NUMERICAL AND THEORETICAL MODELING OF THERMOACOUSTIC INSTABILITIES IN TRANSCRITICAL FLUIDS

A Dissertation

Submitted to the Faculty

of

Purdue University

by

Mario Tindaro Migliorino

In Partial Fulfillment of the

Requirements for the Degree

of

Doctor of Philosophy

December 2018

Purdue University

West Lafayette, Indiana

THE PURDUE UNIVERSITY GRADUATE SCHOOL
STATEMENT OF DISSERTATION APPROVAL

Dr. Carlo Scalo, Chair

School of Mechanical Engineering

Dr. Stephen D. Heister

School of Aeronautics and Astronautics

Dr. J. Stuart Bolton

School of Mechanical Engineering

Dr. Hector Gomez

School of Mechanical Engineering

Approved by:

Dr. Jay P. Gore

Associate Head for Graduate Studies

To “Inspiration”

ACKNOWLEDGMENTS

This doctoral work has been supported by the Frederick N. Andrews Fellowship, Rolls-Royce Doctoral Fellowship, and the Purdue/Rolls-Royce University Technology Center (UTC) grant in Advanced Thermal Management Systems led by Mr. Pat Sweeney (Rolls-Royce, Indianapolis) and Prof. Stephen D. Heister (lead PI, Purdue).

The use of the solver SD3DVISP originally developed by Prof. Antony Jameson's group, and of the solver HYBRID by Prof. Johan Larsson, is gratefully acknowledged. The computing resources were provided by the Rosen Center for Advanced Computing (RCAC) at Purdue University and Information Technology at Purdue (ITaP).

I am deeply grateful to my advisor, Dr. Carlo Scalo, who had a pivotal role in my professional life, making me transition from a student to a research scientist. I thank him very much for all his support and encouragement. I also want to thank Prof.s J. Stuart Bolton, Anil K. Bajaj, and Eckhard Groll for their dedication to teaching, which gave me inspiration and knowledge. All the work from Dayle Alexander, Ariana Martinez, and Karl Jantze on the building and testing of the experimental hardware at the Zucrow Labs is also deeply appreciated.

My time at Purdue has been such a life-changing adventure that it is difficult to thank in words all the people I want. Nevertheless, special mention and thanks go to my friends Iman, James, Fahim, Caitlyn, Ninad, Divya, Enrico, Emanuela, Leonardo, Loris, David, Valeria, Tricia, Victor, Jean-Baptiste, Prateek, Rufat, Vlad, Timo, Monique, Cis, Christian, Reza, Akshay, Sara, Lucas, Alessandra, Uttara, Vito, Gaby, Renzo, Martina, Matilde, Valentina, Matteo, Riccardo, Alberto, Enrico, Adrian, Mohammadhasan, Praneet, Geoffrey, Danish, Kukjin, Zongxin, Tasha, Paul, David for everything we have shared together during my journey here at Purdue.

Lastly, I want to praise the power of love, affection, fulfillment, and joy which Giulia and my whole family have shared with me. This sustains me continuously.

TABLE OF CONTENTS

Page

LIST OF TABLES

LIST OF FIGURES

Figure Page

Figure Page

Figure Page

Figure Page

Figure Page

Figure Page

ABSTRACT

Migliorino, Mario Tindaro PhD, Purdue University, December 2018. Numerical and Theoretical Modeling of Thermoacoustic Instabilities in Transcritical Fluids . Major Professor: Carlo Scalo, School of Mechanical Engineering.

Enhancements of gas turbine engines efficiency are critical for the development of the next generation of clean and efficient aircraft. With the increase in combustion temperatures, cooling of the turbine blades poses one of the most important thermal management issues. The current and most adopted solution is to flow cooling air bled from the compressor through channels inside turbine blades. Fuel preheating, meant to increase combustion efficiency, could be used to cool such air flow in fuel-air heat exchangers. However, when fuel thermodynamic states approach supercritical pressures and temperatures, large amplitude oscillations have been known to occur with catastrophic hardware failures. For this reason, the use of supercritical fuels in fuel-air heat exchangers has been avoided, thereby reducing the fuel's cooling potential and the overall efficiency of the aircraft. Engine manufacturers desire a model capable of predicting the onset of such disruptive thermoacoustic oscillations. To this goal, we study theoretically and numerically transcritical thermoacoustic oscillations, i.e., thermoacoustic instabilities manifesting themselves when a fluid is heated close to its critical point, where abrupt changes of thermodynamic properties appear. Details of this work will be on the development of a transcritical thermoacoustic theory and on numerical results from linear stability analysis and high-fidelity Navier-Stokes simulations. Meeting the needs of industry and with the intent of pushing technological and scientific barriers, we propose to exploit such powerful oscillations for energy conversion through the use of the first-ever-built transcritical thermoacoustic engine.

1. INTRODUCTION

This chapter begins, in §1.1, with an introduction on thermoacoustic instabilities found in heat exchangers, and their relevance to gas turbine applications. Previous experiments performed by Palumbo [1], described in §1.2, are numerically modeled in §1.3 (this work led to a U.S. patent application [2]). Finally, §1.4 describes the objectives and outline of this doctoral work. The assistance of Dr. Steven Hunt in the writing of §1.1 and §1.2 is deeply appreciated. The reader will find more details about previous work in thermoacoustic oscillations is his PhD thesis [3].

1.1 Thermoacoustic Instabilities in Heat Exchangers and Relevance to Gas Turbine Applications

Increased combustion temperatures of modern gas turbine engines pose cooling issues for turbine blades. Many current engines flow cooling air through channels inside turbine blades, bled from the engine's compressor. Cooling air can exit the compressor in excess of 600-1000°F, and although it is much colder than the turbine blades, it could better cool the turbine if its temperature were reduced before entering the turbine. Fuel in aeronautical applications is typically stored in subcritical temperature conditions (e.g., in the wings of an airplane at cruising conditions where outside air temperatures reach -50 °C) under high pressures, due to the pumping power necessary to allow fuel to be delivered to the engines. Therefore, an aircraft's liquid fuel offers a large heat sink potential for turbine cooling air through use of a fuel-air heat exchanger (Fig. 1.1). In addition to improved turbine cooling, the elevated fuel temperatures associated with such a design can improve an engine's combustion efficiency [4]. However, when fuel temperatures approach the supercritical regime, large pressure oscillations have been known to occur within fuel flow paths [1, 5–10].

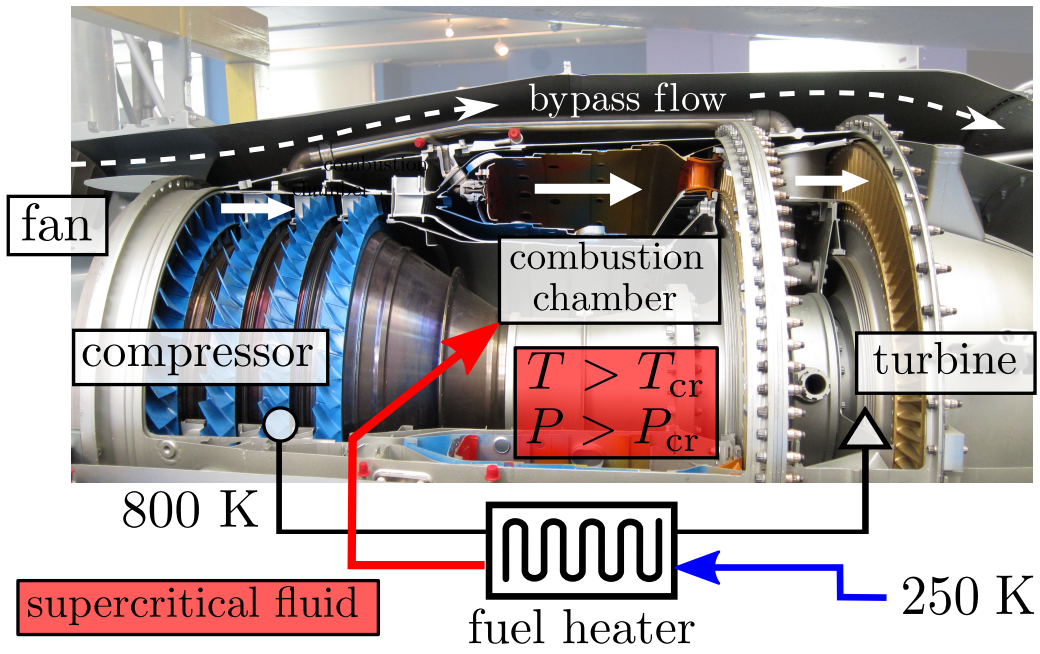

Figure 1.1. Core section of a Rolls-Royce Turboméca Adour turbofan displayed at the Musée de l'Air in Paris, France.

Such oscillations can damage heat exchanger components. For this reason, the use of supercritical fuels in fuel-air heat exchangers has been avoided, thereby reducing the fuel's cooling potential. Engine manufacturers desire a model capable of predicting the onset of pressure oscillations, so that the cooling potential of aircraft fuel may be exploited to its greatest potential.

Supercritical fuel oscillations are known to occur at different oscillation modes. Researchers have observed two distinct types of oscillations near the critical point including bulk-mode oscillations (also known as Helmholtz or pulsating oscillations) and acoustic-scale oscillations. Helmholtz oscillations occurred with high amplitude and low frequency (0.5-3 Hz), whereas acoustic oscillations occurred with low amplitude and high frequency (75-2,000 Hz). A previous work by Hunt and Heister [11] compares test conditions and corresponding results from several publications. Hines and Wolf [5] performed early experiments to show thermoacoustic oscillations in supercrit-

ical fuels. They tested turbulent flows of supercritical RP-1 and diethylcyclohexane (DECH) through thin-walled tubes designed to replicate flowpaths found in rocket cooling jackets. Oscillations were often audible in their tests; oscillations of well-defined frequency with uniform amplitude caused a sound described as a clear and steady scream, whereas oscillations of varying amplitude caused chugging or pulsing noises. Dominant frequencies encountered ranged from 1000-7500 Hz, and pressure amplitudes ranged from 50-380 psi. They unsuccessfully attempted to eliminate these oscillations by placing the tube in cement to damp the vibrations during a run. Linne et al. [9] performed a design of experiments to generate a statistical model predicting the stability of a flow. Their tests involved supercritical JP-7 fuel flowing through a vertical, resistively-heated tube. Five independent variables were selected for this study: test section length, test section inside diameter, mass flow rate, inlet fluid temperature, and heat flux. Buoyancy was originally proposed as a driver of oscillations, but based on the Reynolds and Grashof numbers calculated, buoyancy was deemed negligible for all tests. Their stability analysis was based on the magnitude of RMS pressure. RMS waveforms led to probability distributions of fluid pressure occurring in each test case. The authors arbitrarily selected an RMS pressure of 10 psi as the threshold between a stable and an unstable condition. The model correctly predicted most, but not all, test points as being stable or unstable. Faith et al. [6] experimented with supercritical Jet-A fuel, flowing it through one of several types of resistively-heated tubes. Mean pressure was varied between tests. Heat transfer power was increased over a 5-10 minute period until oscillations began. Oscillations manifested in the form of whistling noises. Pressure fluctuations ranged up to 350 psi. Primary frequencies varied between 1000 and 5000 Hz. Hitch and Karpuk [7] studied vertical flow of MCH and JP-7 through a tube heated by band heaters. They observed two distinct types of oscillations near the critical point: Helmholtz oscillations (also known as bulk-mode oscillations) and acoustic-scale oscillations. Helmholtz oscillations occurred with high amplitude at frequencies from 1-2 Hz, whereas acoustic oscillations occurred with low amplitude at frequencies of 75-450 Hz. Flows were

always stable when the fluid pressure was much higher than the critical pressure. Aiming to eliminate oscillations and increase heat transfer, Hitch and Karpuk tested several turbulating inserts: a twisted-tape insert, a louvered-tape insert, and a static mixer. All three inserts were found to increase the heat transfer coefficient over that of a basic tube. The static mixer caused the largest heat transfer improvement, and reduced Helmholtz oscillations substantially. Flow stability could be maintained with a static mixer until pressure was reduced to less than 1.1 times the critical pressure. Hitch and Karpuk successfully eliminated oscillations even below the critical pressure by using a damping valve to cause a flow restriction before the test section.

1.2 Previous Experimental Work at the Zucrow Labs

Herring's [10] research was aimed at developing a robust and high-performance fuel-air heat exchanger able to accept fuels near or above the supercritical point. Supercritical JP-10 flowed through a single resistively-heated tube in his experimental tests. Independent variables included inlet temperature, mass flow rate, input power, heated length, and total pipe length. This study also tested vertical and horizontal flows to determine the effect of buoyancy, and several types of wire coil inserts in an attempt to improve heat transfer and suppress oscillations. Similar to the results of Hitch and Karpuk, Herring observed bulk-mode oscillations for reduced pressures up to 1.5. Like many other experimenters, Herring only experienced oscillations when the wall temperature was above the pseudocritical temperature and the fuel inlet temperature was below. Unlike the results of Hitch and Karpuk, however, the use of an upstream damping valve did not prevent bulk-mode oscillations. Herring postulated the dissimilarity was due to the different flow systems used: Hitch and Karpuk used a pump-fed system, so the upstream section could be considered incompressible; Herring (and Linne et al.) drove flows with high-pressure gaseous nitrogen, which could apply a restoring force causing Helmholtz oscillations.

Fig. 1.2 shows the flow path in the facility hardware used by Palumbo [1]. Methanol, loaded into the run tank and pressurized, flows to a filter and then an electric preheater. The preheated fuel then enters the test section, which consists of a tube undergoing electric resistance heating. The test section is electrically insulated on each end with isolation flanges. Downstream of the test section, the fluid passes through a cooling bath, filter, flow control valve, sampling station, and finally a waste drum.

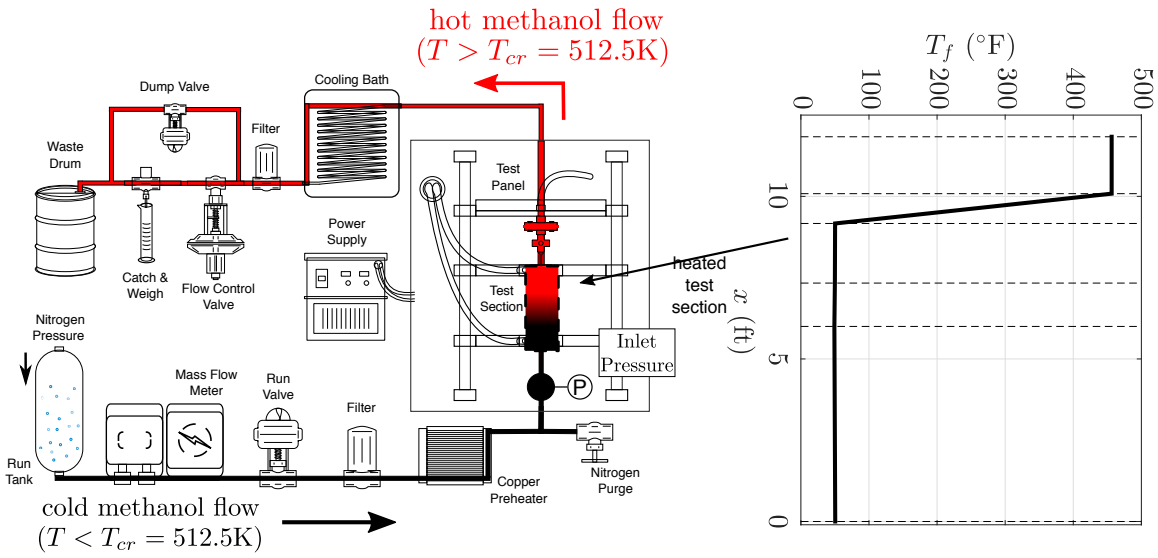

Figure 1.2. Flow path and mean fluid temperature distribution highlighted on Palumbo's rig [1].

Kulite pressure transducers were placed in the inlet and outlet plenum. Data recorded during experiments were sampled at 4 KHz. The chosen reduced pressures of 1.0, 1.2, and 1.4 correspond to pressures of 1175, 1410, and 1645 psi.

Thermoacoustic oscillations were recorded. Those are most prominently displayed in pressure traces near the test section tube and the mass flow rate measurements. Throughout the test campaign, similar to previous studies, two modes of oscillations were detected: the acoustic mode, characterized by frequencies of 100-500 Hz; and the bulk mode, characterized by frequencies from 1-5 Hz. Bulk mode oscillations

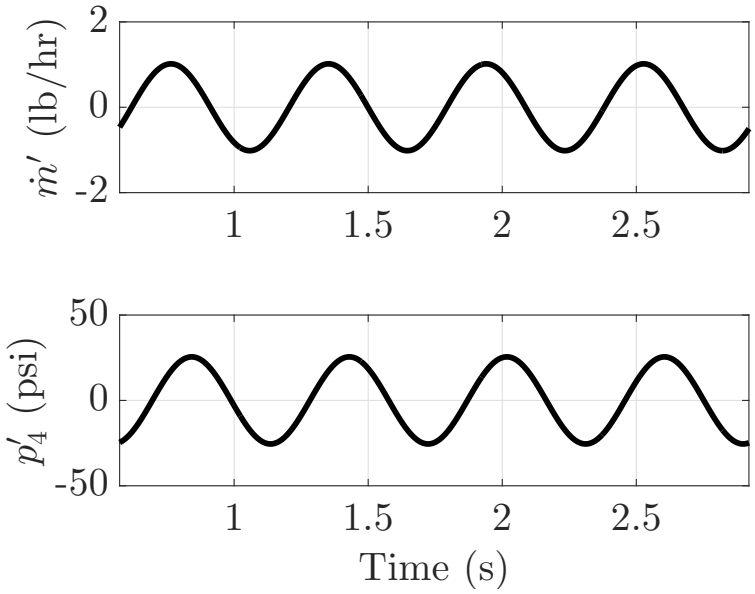

Figure 1.3. Mean-subtracted mass flow rate and tube inlet pressure (bottom) for a sample selected case: $\dot{Q}$ =550W, D_{in} =0.069in, ℓ =6in, $\dot{m}$ =5lb/hr, p_r =1.2.

tend to have amplitudes of over one order of magnitude larger than the acoustic mode. The case illustrated in Fig. 1.3 is representative of the test campaign; both oscillation modes are present, but the bulk mode dominates. Pressure and mass flow rate measurements match in bulk-mode frequency, but are offset by a constant phase lag. This behavior suggests that the instability is a system-wide phenomenon.

1.3 One-Dimensional Thermoacoustic System in Transcritical Conditions

When transcritical fuel is heated through a heat exchanger, destructive high amplitude pressure oscillations can be detected. Configurations can be stable or unstable depending on the particular fluid, the heat released, the geometry of the setup and other parameters. Fluid dynamic instabilities commonly occurring in these highly pressurized systems are called thermoacoustic instabilities and typically also occur in thermoacoustic devices. Thermoacoustic devices are capable of spontaneously gener-

ating acoustic power in the presence of an external temperature differential imposed on the walls of a sealed duct. Wave-induced, quasi-isentropic compressions and dilatations work against the background temperature gradient, spontaneously converting heat into acoustic power and are, thus, self-amplifying. Highly pressurized fluids are usually employed to increase the thermal to acoustic conversion efficiency.

We claim that steady-state acoustic power generation of thermoacoustically unstable ducts corresponds to pressure oscillations observed in unstable heat exchangers. The main driving phenomenon is the large variation of fluid density with temperature at supercritical pressures and for temperatures close to the critical temperature. In order to assess the stability region of fuel heat exchangers, a relationship between dimensionless critical heat release rate and dimensionless mean pressure can be used (derived from a Buckingham Pi theorem). This is an empirically-based method. A second, physics-based method, can be derived considering thermoacoustic devices. A conceptual connection must be performed between dimensionless critical heat and dimensionless critical temperature. The latter is the difference in wall temperature that entails instability for a thermoacoustic device. Furthermore, a conceptual connection must be performed between dimensionless mean pressure and other parameters of the latter device.

A sealed duct in figure 1.4 comprises a tube and a stack, a very efficient heat exchanger.

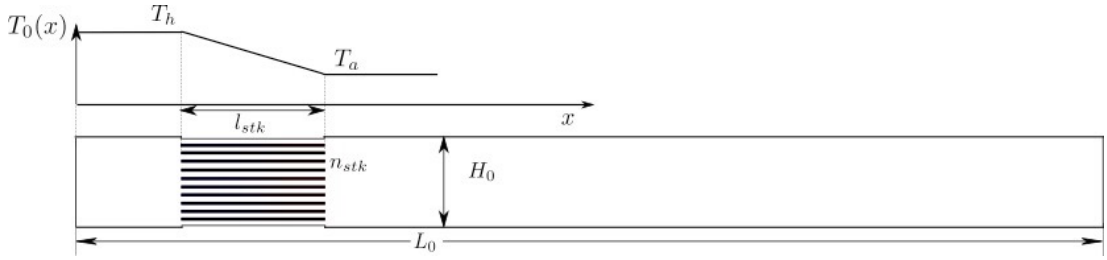

Figure 1.4. A thermoacoustic device. A linear temperature profile is imposed inside the stack, between a high temperature T_h and a base temperature T_a.

The temperature profile

$$\begin{cases} T_0 = T_{hot} & 0 \leq x \leq l_1 \\ T_0 = T_{hot} + \frac{T_{hot}-T_{cold}}{l_1-l_2}(x-l_1) & l_1 < x < l_2 \\ T_0 = T_{cold} & l_2 \leq x \leq L \end{cases}$$

is imposed to the fluid.

Depending on the geometry, the fluid, and $\Delta T = T_h - T_a = T_{hot} - T_{cold}$, the device can be stable or unstable. In the case of instability, pressure oscillations can be detected. If the device is unstable, it means that ΔT exceeds ΔT_{min}, the minimum temperature difference for the onset of instability. Here we fix the length of the setup at L_0=0.5m long and the stack is from 0.05m to 0.175m (12.5cm long). All simulations are considered with uniform pressure $p_0 \geq p_c$.

In the stack, the heat flux between solid and fluid is approximated by a simplified heat release source term that is in phase with temperature fluctuations. Although this is not what happens in reality, this is a good approximation in many cases. We use a linearized version of the Peng-Robinson equation of state together with linearized Navier-Stokes equations to derive a model that can predict thermoacoustic instability for real gases. A first order expansion of the variables can be assumed

$$\rho = \rho_0(x)+\rho'(x,t), \quad T = T_0(x)+T'(x,t), \quad p = p_0+p'(x,t), \quad u = u_0+u'(x,t), \tag{1.1}$$

in which a mean value only dependent on space is added to a fluctuation time and space dependent in order to get the full variable. After some derivations, four equations can be obtained, containing the linearized Navier-Stokes equations and the equation of state.

We model the thermoacoustic system in figure 1.4 with a one-dimensional geometry employing a previously used stack model [12] .The latter consists in source terms that model the heat exchange happening in the stack of a thermoacoustic engine. The momentum source term is

$$F = -(R_C + R_F u)u, \tag{1.2}$$

which linearized is

$$F = -R_C u, \tag{1.3}$$

with

$$R_C = C_{sf}\mu\frac{1-\phi}{4d_w^2\phi}, \tag{1.4}$$

$$R_F = \frac{\rho C_{fd}}{4d_w}, \tag{1.5}$$

$$r_h = \frac{d_w\phi}{4(1-\phi)}, \tag{1.6}$$

where r_h is the hydraulic radius of the pores of the stack, d_w is the mesh wire size, ϕ is the porosity, C_{fd}, C_{sf} are dimensionless fitting constants from metal felts correlations.

The energy source term is in phase with temperature fluctuations

$$\dot{Q} = -uF - \tilde{q}(T - T_0), \tag{1.7}$$

which linearized is

$$\dot{Q} = -\tilde{q}(T - T_0), \tag{1.8}$$

where the heat release parameter is heuristically how much total energy varies with temperature at constant volume (ρc_v) over a time scale

$$\tilde{q} = \frac{\rho c_v}{\tau_h}, \tag{1.9}$$

where the characteristic time scale for heat transfer in the pores is

$$\tau_h = \frac{r_h^2}{k/(\rho c_p)} = \frac{r_h^2\rho\mathrm{Pr}}{\mu}, \tag{1.10}$$

valid for every $t > 0$. The parameter $\tilde{q}$ is therefore

$$\tilde{q} = \frac{\rho c_v}{\frac{r_h^2}{k/(\rho c_p)}} = \frac{k}{r_h^2\gamma}, \tag{1.11}$$

and it has dimensions of power per unit volume per unit Kelvin (W/m^3K). This model is expected to be accurate within an order of magnitude.

The source terms,

$$F = -bu^3, \qquad \dot{Q} = -\alpha(T - T_0), \tag{1.12}$$

become, in linearized form,

$$F = -R_{C_0} u', \qquad \dot{Q} = -\frac{k_0}{r_h^2 \gamma_0} T', \tag{1.13}$$

where the heat source is active only in the stack.

If we assume the harmonic dependence

$$p' = \hat{p}(x)e^{j\omega t}, \quad u' = \hat{u}(x)e^{j\omega t}, \quad T' = \hat{T}(x)e^{j\omega t}, \quad \rho' = \hat{\rho}(x)e^{j\omega t}, \tag{1.14}$$

and consider as given the reference quantities and their spatial gradients, we can eliminate the time dependence and solve an eigenvalue problem in the matrix form

$$A\hat{v} = \lambda B\hat{v}, \tag{1.15}$$

$$\begin{pmatrix} A_{11} & A_{12} & A_{13} \\ A_{21} & A_{22} & A_{23} \\ A_{31} & A_{32} & A_{33} \end{pmatrix} \begin{pmatrix} \hat{p} \\ \hat{u} \\ \hat{T} \end{pmatrix} = j\omega \begin{pmatrix} \frac{\gamma_0}{\rho_0 {a_0}^2} & 0 & -\alpha_{p_0} \\ \frac{u_0 \gamma_0}{{a_0}^2} & \rho_0 & -u_0 \rho_0 \alpha_{p_0} \\ 0 & 0 & 1/T_0 \end{pmatrix} \begin{pmatrix} \hat{p} \\ \hat{u} \\ \hat{T} \end{pmatrix}, \tag{1.16}$$

$$\begin{cases} A_{11} = -\dfrac{u_0}{\rho_0}\left(\dfrac{d\gamma_0/{a_0}^2}{dx} + \dfrac{\gamma_0}{{a_0}^2}\mathcal{D}_p\right) \\ A_{12} = -\mathcal{D}_u - \dfrac{d\ln\rho_0}{dx} \\ A_{13} = \dfrac{u_0}{\rho_0}\left(\rho_0\alpha_{p_0}\mathcal{D}_p + \dfrac{d\rho_0\alpha_{p_0}}{dx}\right) \\ A_{21} = -u_0^2(\dfrac{d\gamma_0/{a_0}^2}{dx} + \dfrac{\gamma_0}{{a_0}^2}\mathcal{D}_p) - \mathcal{D}_p \\ A_{22} = -2\rho_0 u_0 \mathcal{D}_u - 2\rho_0 u_0 \dfrac{d\ln\rho_0}{dx} + \dfrac{4}{3}\left(\dfrac{d\mu_0}{dx}\mathcal{D}_u + \mu_0\mathcal{D}_u^2\right) - R_{C_0} \\ A_{23} = u_0^2(\rho_0\alpha_{p_0}\mathcal{D}_p + \dfrac{d\rho_0\alpha_{p_0}}{dx}) \\ A_{31} = -\dfrac{\gamma_0 u_0}{\rho_0 {a_0}^2}\dfrac{d\ln T_0}{dx} \\ A_{32} = -\dfrac{d\ln T_0}{dx} - \dfrac{\gamma_0 - 1}{\alpha_{p_0} T_0}\mathcal{D}_u \\ A_{33} = -\dfrac{u_0}{T_0}\mathcal{D}_p + u_0\alpha_{p_0}\dfrac{d\ln T_0}{dx} + \dfrac{k_0}{\rho_0 c_{v_0} T_0}\mathcal{D}_p^2 + \dfrac{1}{\rho_0 c_{v_0} T_0}\dfrac{dk_0}{dx}\mathcal{D}_p - \dfrac{q}{\rho_0 c_{v_0} T_0}\hat{T}, \end{cases} \tag{1.17}$$

which is a generalized eigenvalue problem.

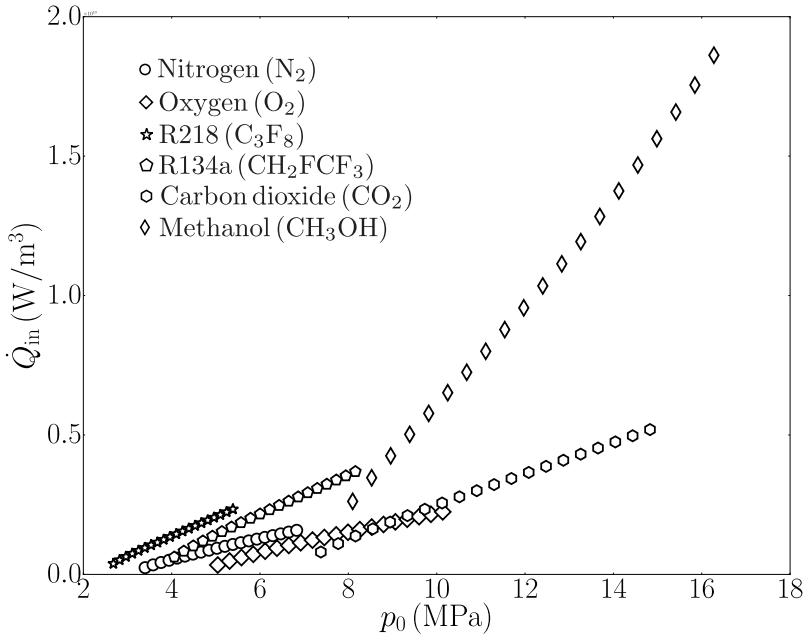

Figure 1.5. Transcritical stability profile. Volumetric power, needed to generate instability in a transcritical thermoacoustic device, is plotted versus mean pressure p_0. Six different fluids exhibit stability regions below approximately straight lines.

The heat exchanger stable region can be alternatively assessed with the analysis of the aforementioned analogous thermoacoustic system, under fluid dynamic instability, exhibiting the transcritical stability profile in figure 1.5. The volumetric power $\dot{Q}_{\rm in}$ (on the y axis in figure 1) is the heat per unit time per unit volume absorbed by the fluid in the analogous system. It can be calculated, from relevant design/operational parameters of the fuel heat exchanger, following a heat transfer formula. The heat transfer formula is as follows:

$$\dot{Q}_{\rm in} = {\rm Nu}\frac{4\bar{k}}{D^2\bar{\gamma}}\Delta T, \tag{1.18}$$

where the temperature difference between inlet and outlet of the heat exchanger is

$$\Delta T = T_{\rm outlet} - T_{\rm inlet}, \tag{1.19}$$

Table 1.1.
Sample values for methanol at pressure $p_0 = 8.527\,\mathrm{MPa}$.

	inlet	outlet	mean
$T\,(\mathrm{K})$	507.514	1141.658	824.586
$\rho\,(\mathrm{kg/m^3})$	318.326	28.301	173.314
$\mu\,(10^{-5}\mathrm{Pa\cdot s})$	4.223	2.784	3.504
$k\,(\mathrm{W/(m\cdot K)})$	0.1403	0.114	0.127
$c_p\,(\mathrm{J/(kg\cdot K)})$	11760.333	3104.363	7432.348
γ	5.333	1.109	3.221

and where the Nusselt number for forced convection (Dittus-Boelter equation) is

$$\mathrm{Nu} = 0.023\,\mathrm{Re}^{0.8}\,\mathrm{Pr}^{0.4}, \tag{1.20}$$

where the Reynolds number is

$$\mathrm{Re} = \frac{4\dot{m}}{\pi D\bar{\mu}}, \tag{1.21}$$

and the Prandtl number is

$$\mathrm{Pr} = \frac{\bar{c}_p\bar{\mu}}{\bar{k}}, \tag{1.22}$$

and μ is the dynamic viscosity, k the thermal conductivity, c_p and c_v the specific isobaric and isochoric heat coefficients, respectively, $\gamma = c_p/c_v$, D is the diameter of the duct, and $\dot{m}$ is the fuel mass flow rate. A bar over a quantity indicates that it has been averaged between its values at the inlet and at the outlet of the tube,

$$\bar{\varphi} = \frac{\varphi_{\mathrm{outlet}} + \varphi_{\mathrm{inlet}}}{2}, \tag{1.23}$$

where φ is a generic variable.

1.4 Research Objectives and Dissertation Outline

The goal of the present doctoral effort is to develop high-quality theoretical and numerical simulation tools to investigate, model, and understand thermoacoustic instabilities in transcritical fluids. An outline of the document is as follows.

Chapter 2 provides details regarding transcritical fluids (§2.1), real-fluid models (§2.2), the governing equations for a fully compressible flow, in their nonlinear (§2.3) and linearized form (§2.4, §2.5), the acoustic (§2.6) and total energy budgets (§2.7), and a non-iterative method to obtain temperature from conserved variables (§2.8).

Chapter 3 starts off with §3.1, where the importance of supercritical flow simulations is underlined. Numerical simulations, employing the numerical setup described in §3.2, are then analyzed in §3.3, where results on traveling entropy wave (1D, §3.3.1), falling supercritical blob (2D, §3.3.2), and turbulent channel flow (3D, §3.3.3) are presented.

Chapter 4 is organized as follows. After a an introduction regarding thermoacoustic instabilities (§4.1), the problem formulation (§4.2) is proposed, starting with the selection of thermodynamic conditions employed in the Navier-Stokes simulations (§4.2.1), followed by the description of the computational setup (§4.2.2), and by a grid sensitivity analysis (§4.2.3). Real-fluid effects are then discussed in §4.3, namely on the frequencies (§4.3.1), growth rates (§4.3.2), and eigenmodes, in §4.3.3. Then, the energy budgets are discussed in §4.4, with a first focus on the acoustic energy budgets (§4.4.1), and then on the total energy budgets (§4.4.2). Finally, high amplitude pressure oscillations are investigated in §4.5, first by describing the limit cycle obtained with nonlinear area losses (§4.5.1), and then with the discussion of the thermodynamic nonlinearities typical of transcritical fluids (§4.5.2).

Chapter 5 is about heat-release-induced waves in supercritical fluids. After an introduction (§5.1), the chapter shows details regarding the problem formulation (§5.2), comprising the selection of fluids (§5.2.1) and the computational setup (§5.2.2). The derivation of a set of reference scaling parameters for all thermo-fluid-dynamic

fluctuations yielding full collapse of isentropic acoustic (§5.3.1) and quasi-isentropic heat-release-induced planar waves (§5.3.2, §5.3.3, §5.3.4) is presented in §5.3. A new modeling strategy (§5.4), valid for a generic compressible fluid, is first derived in §5.4.1, highlighting real-fluid effects on non-isentropic shock wave generation and propagation. Finally, the model allows for a quantitative measure of the thermal to mechanical power conversion efficiency (§5.4.2), and an assessment of its asymptotic behavior for heat release rate tending to infinity (§5.4.3).

Chapter 6 provides a summary of all the results.

2. REAL-FLUID THERMODYNAMICS AND FLOW EQUATIONS

2.1 Supercritical and Transcritical States

A supercritical state is reached when the fluid is at temperatures and pressures exceeding its critical values, $T > T_{cr}$ and $p > p_{cr}$, respectively (figure 2.1a). Supercritical fluids share properties of both gases and liquids, in a seemingly homogeneous yet ambiguous state of matter. In reality, there is a definable, even if smooth, transition between pseudoliquid (or liquid-like) and pseudogaseous (or gaseous-like) conditions, especially in the vicinity of the critical point, identifiable by the pseudoboiling (PB) line, also termed the Fisher–Widom line [13]. The PB line is an extension of the gas-liquid coexistence curve above the critical point [14] and is hereafter defined as the locus of temperature and pressure values ($T_{pb} > T_{cr}, p_{pb} > p_{cr}$) at which the thermal expansion coefficient of the fluid is maximum. A pseudo phase transition, or simply pseudotransition, occurs, for example, when temperature changes from $T < T_{pb}$ to $T > T_{pb}$ (or vice versa), for given pressure conditions $p = p_{pb}$, hence crossing the PB line in the $p - T$ phase diagram. The goal of the present work is to investigate the dynamics of thermoacoustics when the instantaneous temperature and density fields fluctuate about such pseudoboiling conditions, also referred to as transcritical. Unlike a subcritical phase change, there is no latent heat, intended in its standard definition, since the pseudotransition takes place over a finite temperature range centered around pseudoboiling (PB) conditions. While in the liquid- and gas-like supercritical states molecules are homogeneously distributed in space with a well-defined mean free path, during pseudotransition, heterogeneously distributed microscopic clusters of tightly packed molecules are formed [15]. This results in abrupt changes in compressibility and density (figure 2.2), and an intense increase in the heat capacity (figure 2.2), with gas-like behavior retained in the voids between molecular clusters. This het-

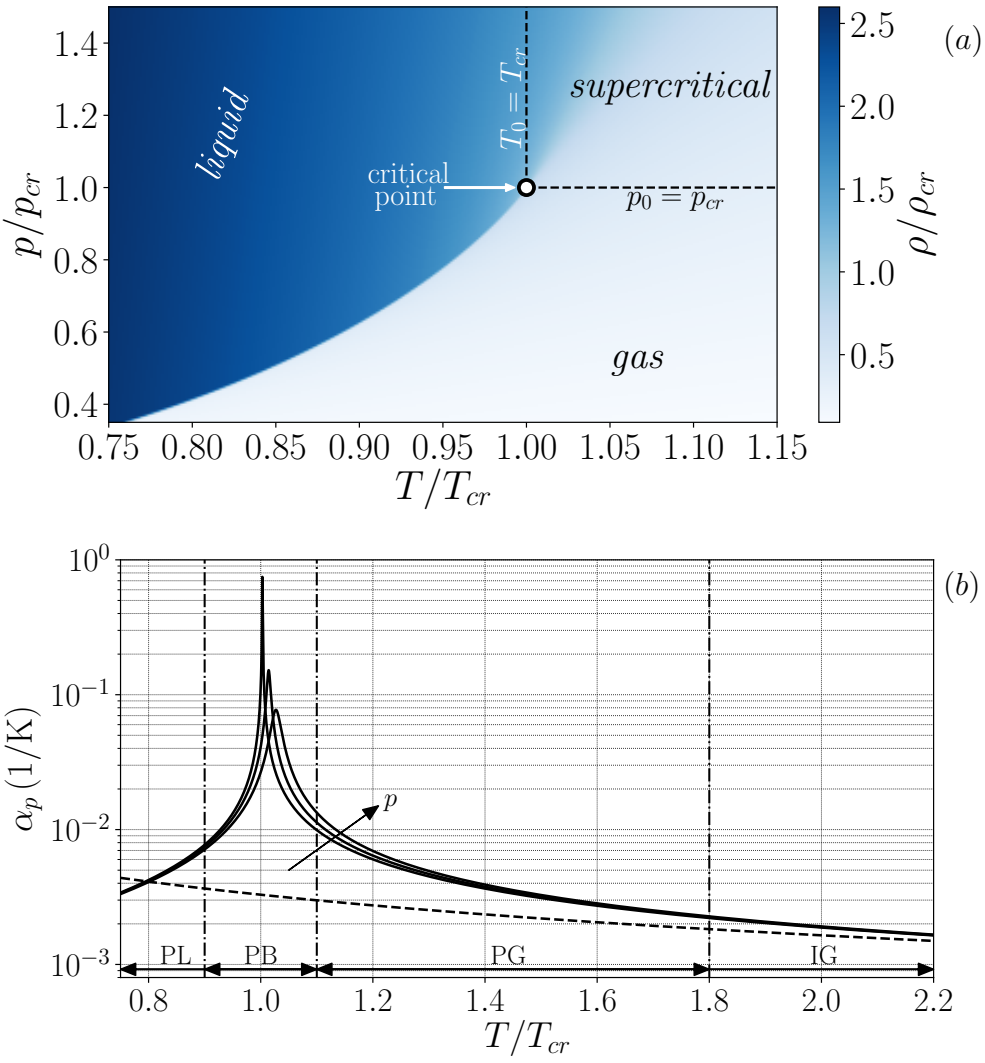

Figure 2.1. (a): phase diagram for carbon dioxide showing flooded contours of reduced density ρ/ρ_{cr}, the critical point ($T = T_{cr}$, $p = p_{cr}$), and the supercritical regime ($T > T_{cr}$, $p > p_{cr}$); (b): isobaric thermal expansion coefficient (Eq. (2.11)) versus temperature for CO_2 at $p/p_{cr} = 1.02, 1.1, 1.2$ modeled with the PR EoS (solid line) and as an ideal gas (dashed line).

erogeneous microscopic distribution results in optical dispersion effects allowing the experimental identification of pseudotransition [16, 17].

For a fixed pressure, starting from cold and heavy pseudo-liquid (PL), for increasing temperatures the density dramatically falls trough a pseudo-boiling (PB) process [13–15], after which the fluid transitions to a pseudo-gaseous (PG) state, reaching eventually a near-ideal-gas state (IG) (figure 2.1b).

2.2 Real-Fluid Models

The equation of state (EoS) proposed by [18], hereinafter called PR EoS, is chosen as real-fluid model because of its thermodynamic consistency, simplicity, and accuracy for the parameter space explored in this study. The PR EoS relates pressure p, temperature T, and density ρ via

$$p = \frac{R_u T}{v_m - b_m} - \frac{\alpha_m}{{v_m}^2 + 2 v_m b_m - {b_m}^2}, \tag{2.1}$$

where $v_m = M_m/\rho$ is the molar volume, M_m is the molar mass of the substance, $R = R_u/M_m$ where $R_u = 8.314472\ \mathrm{J \cdot mol^{-1} K^{-1}}$ is the universal gas constant, $b_m = 0.07780 R_u T_{cr}/p_{cr}$, and the subscript "$cr$" indicates thermodynamic quantities at the critical point. The last coefficient in Eq. (2.1) is

$$\alpha_m = 0.45724 \frac{{R_u}^2 {T_{cr}}^2}{p_{cr}} \left(1 + \left(0.37464 + 1.54226\omega - 0.26992\omega^2\right)\left(1 - \sqrt{T/T_c}\right)\right)^2 \tag{2.2}$$

where ω is the acentric factor of the substance. Real-fluid dynamic viscosity and thermal conductivity are estimated via the method of [19].

Table 2.1.
Fluid properties relative to carbon dioxide.

fluid	T_{cr}(K)	p_{cr}(MPa)	ρ_{cr}(kg/m^3)	v_{mcr}(cm^3/mol)	M_m(g/mol)	ω
CO_2	304.1282	7.3773	467.6	94.1189	44.01	0.225

All of the thermodynamic derivatives required by the current study, here omitted for brevity, can be computed directly, retaining full thermodynamic consistency, from

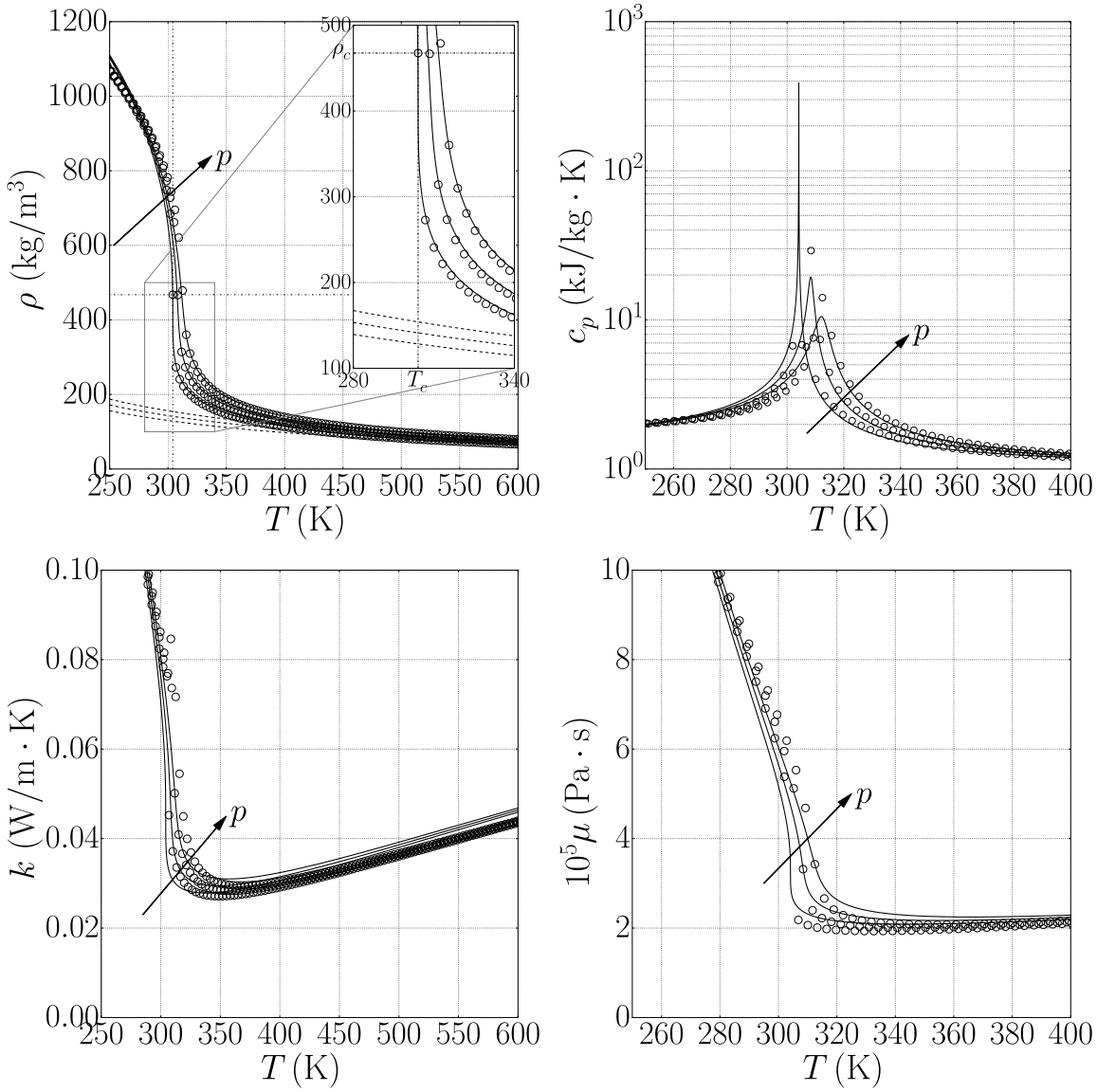

Figure 2.2. Top row: comparison between the Peng-Robinson equation of state (solid lines) and data from the NIST database (circles) for CO_2 at $p = 1.01, 1.10, 1.20\ p_{cr}$. Density $\rho = \rho(T, p)$ on the left, and isobaric specific heat $c_p(T, p)$ on the right, are shown as a function of temperature. On the left, density as given by ideal gas law for the same pressure levels is shown with dashed lines. Bottom row: comparison between Chung's method (solid lines) and data from the NIST database (circles) for CO_2 at $p = 1.01, 1.10, 1.20\ p_{cr}$. Thermal conductivity, $k = k(T, p)$, on the left, and dynamic viscosity $\mu = \mu(T, p)$, on the right, are shown versus temperature.

eq. (2.1). In particular, they can be used to compute any generic thermodynamic quantity with the thermodynamic departure functions [20]. With this approach, a first contribution at constant volume is given by assuming a thermodynamic transformation, following ideal gas law, from $T = 0$ to T, reaching the state (T, v^0) where $v^0 = RT/p^0$ and $p^0 = 1$ bar [21]. Consequently, a volume integration, departing from the thus-derived ideal gas reference state, is performed to the final state (T, v). This strategy can be applied to compute, for example, the specific isochoric, $c_v(T, v)$, and isobaric, $c_p(T, v)$, heat capacities by correcting their ideal gas counterparts, obtained from the polynomial fit given in the appendix of Poling *et. al.* [20].

The PR EoS is in acceptable agreement with data from the NIST database [22] (figure 2.2) for CO_2 at the three selected pressures of $p = 1.01, 1.10, 1.20\ p_{cr}$ and for temperatures higher than T_{cr}. Figure 2.2 shows, on the left, the rapid drop in density approaching the critical point and how, for high temperatures, CO_2 behaves like an ideal gas. On the right, a very high thermal capacity in the near-critical region is shown. Dynamic viscosity and thermal conductivity are estimated via Chung's method [19, 20], also in fair agreement with NIST (figure 2.2) for CO_2.

In the near-critical region, the PR EoS fails to capture the experimental value of the critical density, being such equation tuned to the correct values of critical pressures and temperatures only, more easily measurable than the critical volume [23]. For carbon dioxide, in fact, the critical density predicted by PR EoS is 400 kg/m^3, which differs significantly from the experimental value $\rho_{cr} = 467.6$ kg/m^3 (table 2.1).

Even if density corrections are available for cubic equations of state [21], in this work the original version of the PR EoS is used. In fact the aim of this work is not to reproduce exactly experimental measurements or quantitatively capture the near-critical behavior of CO_2, but rather to perform theoretical numerical simulations, inspired by experimental investigations.

2.3 Fully Compressible Three-Dimensional Flow Equations

In this work, the fluid motion is modeled using the compressible Navier-Stokes equations, expressed by the conservation laws of mass, momentum, and total energy,

$$\frac{\partial \rho}{\partial t} + \frac{\partial \rho u_j}{\partial x_j} = 0, \tag{2.3}$$

$$\frac{\partial \rho u_i}{\partial t} + \frac{\partial \rho u_i u_j}{\partial x_j} = -\frac{\partial p}{\partial x_i} + \frac{\partial \tau_{ij}}{\partial x_j} + \dot{F}_i, \tag{2.4}$$

$$\frac{\partial \rho E}{\partial t} + \frac{\partial \rho E u_j}{\partial x_j} = -\frac{\partial p u_j}{\partial x_j} + \frac{\partial u_i \tau_{ij}}{\partial x_j} - \frac{\partial q_j}{\partial x_j} + \dot{F}_j u_j, \tag{2.5}$$

where t is time, x_j and u_j $(j = 1, 2, 3)$ are the components of position and velocity, ρ and p are the density and pressure, $E = e + u_i u_i/2$ is the specific total energy, sum of specific internal energy and kinetic energy, and $\dot{F}$ is a source term. The Newtonian viscous stress tensor τ_{ij} and the Fourier heat flux read, respectively,

$$\tau_{ij} = \mu \left(\frac{\partial u_i}{\partial x_j} + \frac{\partial u_j}{\partial x_i} - \frac{2}{3}\delta_{ij} \frac{\partial u_k}{\partial x_k} \right), \qquad q_j = -k \frac{\partial T}{\partial x_j}, \tag{2.6}$$

where δ_{ij} is the Kronecker delta, μ is the dynamic viscosity, k is the thermal conductivity, T is the temperature, and Stokes's hypothesis has been adopted.

Eq. (2.5) can be rewritten as the evolution equation for the specific internal energy, e, or specific enthalpy, $h = e + p/\rho$, or specific entropy, s,

$$\begin{aligned} \rho \frac{De}{Dt} &= -p \frac{\partial u_j}{\partial x_j} + \rho T \frac{Ds}{Dt}, \\ \rho \frac{Dh}{Dt} &= \frac{Dp}{Dt} + \rho T \frac{Ds}{Dt}, \\ \rho T \frac{Ds}{Dt} &= \tau_{ij} \frac{\partial u_i}{\partial x_j} - \frac{\partial q_j}{\partial x_j}, \end{aligned} \tag{2.7}$$

where D/Dt is the material derivative. The equation of state $p = p(\rho, T)$ can be differentiated to obtain

$$\gamma dp/\rho a^2 = v d\rho + \alpha_p dT, \tag{2.8}$$

where $v = 1/\rho$ is the specific volume. the isobaric thermal expansion coefficient. The thermodynamic relation $dh = c_p dT + v(1 - \alpha_p T)dp$, Eq. (2.8), and the relation

$c_p - c_v = \alpha_p^2 T v/\kappa_T$ allow to rewrite the enthalpy evolution equation as the pressure or temperature evolution equations,

$$\begin{aligned} \frac{Dp}{Dt} &= -\rho a^2 \frac{\partial u_j}{\partial x_j} + \frac{\rho a^2 \alpha_p T}{c_p} \frac{Ds}{Dt}, \\ \rho c_v \frac{DT}{Dt} &= -\frac{\rho c_v}{\alpha_p}(\gamma - 1)\frac{\partial u_j}{\partial x_j} + \rho T \frac{Ds}{Dt}. \end{aligned} \tag{2.9}$$

Therefore the first of Eq. (2.10) can be rewritten as the evolution equation for pressure,

$$\frac{\partial p}{\partial t} + \frac{\partial p u_j}{\partial x_j} = (p - \rho a^2)\frac{\partial u_j}{\partial x_j} + \frac{a^2 \alpha_p}{c_p}\left(\tau_{ij}\frac{\partial u_i}{\partial x_j} - \frac{\partial q_j}{\partial x_j}\right). \tag{2.10}$$

where the isobaric thermal expansion coefficient is

$$\alpha_p = -\frac{1}{\rho}\left(\frac{\partial \rho}{\partial T}\right)_p, \tag{2.11}$$

a is the sound speed, and c_p is the isobaric specific thermal capacity.

2.4 Derivation of Quasi-Planar Wave Equations

The evolution equations for mass, axial momentum, and pressure, in a two-dimensional domain, with x ($j = 1$) corresponding to the axial direction and r ($j = 2$) to the radial direction, read

$$\begin{aligned} \frac{\partial \rho}{\partial t} + u_j \frac{\partial \rho}{\partial x_j} &= -\rho\left(\frac{\partial u}{\partial x} + \frac{1}{r^m}\frac{\partial r^m v}{\partial r}\right), \\ \rho\left(\frac{\partial u}{\partial t} + u_j \frac{\partial u}{\partial x_j}\right) &= -\frac{\partial p}{\partial x} + \frac{\mu}{r^m}\frac{\partial}{\partial r}\left(r^m \frac{\partial u}{\partial r}\right), \\ \frac{\partial p}{\partial t} + u\frac{\partial p}{\partial x} &= a^2\left(\frac{\partial \rho}{\partial t} + u_j \frac{\partial \rho}{\partial x_j}\right) + \frac{\alpha_p a^2}{c_p}\left(\tau_{ij}\frac{\partial u_i}{\partial x_j} + \frac{k}{r^m}\frac{\partial}{\partial r}\left(r^m \frac{\partial T}{\partial r}\right)\right), \end{aligned} \tag{2.12}$$

where we considered cartesian ($m = 0$) or cylindrical ($m = 1$) coordinates, neglected axial viscous and conduction stresses, assumed that $\mu = \mu(x)$ and $k = k(x)$, and disregarded the momentum equation in the r direction ($\partial p/\partial r = 0$, $v = v(r)$, and negligible viscous stresses along r).

A first order Taylor expansion is assumed, both for thermodynamic and kinematic variables,

$$\begin{gathered}\rho = \rho_0(x) + \rho'(x,y,t), \qquad T = T_0(x) + T'(x,y,t), \qquad p = p_0 + p'(x,t), \\ u = u'(x,y,t), \qquad v = v'(y),\end{gathered} \tag{2.13}$$

where a generic variable is composed of a base quantity, at most varying axially, and a fluctuation that is time and space dependent, and no mean flow is considered. Neglecting nonlinear terms, and with the assumptions in Eq. (2.13), Eq. (2.12) becomes

$$\begin{aligned}\frac{\partial \rho'}{\partial t} + u'\frac{d\rho_0}{dx} &= -\rho_0\left(\frac{\partial u'}{\partial x} + \frac{1}{r^m}\frac{\partial r^m v'}{\partial r}\right), \\ \rho_0\frac{\partial u'}{\partial t} &= -\frac{\partial p'}{\partial x} + \frac{\mu_0}{r^m}\frac{\partial}{\partial r}\left(r^m\frac{\partial u'}{\partial r}\right), \\ \frac{\partial p'}{\partial t} &= a_0^2\left(\frac{\partial \rho'}{\partial t} + u'\frac{d\rho_0}{dx}\right) + \frac{\gamma_0 - 1}{\alpha_{p_0}T_0}\frac{k_0}{r^m}\frac{\partial}{\partial r}\left(r^m\frac{\partial T'}{\partial r}\right),\end{aligned} \tag{2.14}$$

where we used the thermodynamic relation $a^2 T\alpha_p^2/c_p = \gamma - 1$.

Introducing the variables

$$U' = \int_{-\delta_{0m}h/2}^{h/2} u'(x,r,t)(2\pi r)^m dr, \qquad A = \int_{-\delta_{0m}h/2}^{h/2}(2\pi r)^m dr, \tag{2.15}$$

which are, respectively, the volumetric flow rate fluctuations and the cross sectional area for cylindrical coordinates ($m = 1$), or pore height times 1 m for rectilinear coordinates ($m = 0$), and integrating Eq. (2.14) over the cross section, we obtain

$$\rho_0\frac{\partial U'}{\partial t} = -A\frac{\partial p'}{\partial x} + \tau_w', \qquad A\frac{\partial p'}{\partial t} = -\rho_0 a_0^2\frac{\partial U'}{\partial x} + \frac{\gamma_0 - 1}{\alpha_{p_0}T_0}q', \tag{2.16}$$

after accounting for impenetrable boundary conditions in r, and assuming symmetry of the fluctuations around the centerline of the duct in the expressions of the wall shear stress and the wall heat flux, respectively,

$$\tau_w' = 2\mu_0\left(\frac{\pi h}{2}\right)^m \left.\frac{\partial u'}{\partial r}\right|_{r=h/2}, \qquad q' = 2k_0\left(\frac{\pi h}{2}\right)^m \left.\frac{\partial T'}{\partial r}\right|_{r=h/2}. \tag{2.17}$$

Assuming an harmonic dependence of the perturbations (normal mode assumption),

$$\begin{gathered}\rho' = \hat{\rho}(x,r)e^{\sigma t}, \quad T' = \hat{T}(x,r)e^{\sigma t}, \quad p' = \hat{p}(x)e^{\sigma t}, \\ u' = \hat{u}(x,r)e^{\sigma t}, \quad v' = \hat{v}(r)e^{\sigma t},\end{gathered} \tag{2.18}$$

where it is intended that the physical solution of all the perturbations is the real part of the respective expressions, Eq. (2.14) becomes

$$\begin{aligned} \sigma\hat{\rho} &= -\rho_0\frac{\partial\hat{u}}{\partial x} - \hat{u}\frac{d\rho_0}{dx} - \frac{\rho_0}{r^m}\frac{\partial r^m\hat{v}}{\partial r}, \\ \sigma\hat{u} &= -\frac{1}{\rho_0}\frac{d\hat{p}}{dx} + \frac{\nu_0}{r^m}\frac{\partial}{\partial r}\left(r^m\frac{\partial\hat{u}}{\partial r}\right), \\ \sigma\left(\hat{\rho} - \frac{1}{a_0^2}\hat{p}\right) &= -\hat{u}\frac{d\rho_0}{dx} + \frac{\nu_0}{\mathrm{Pr}_0}\frac{1}{r^m}\frac{\partial}{\partial r}\left(r^m\frac{\partial\hat{\rho}}{\partial r}\right), \end{aligned} \tag{2.19}$$

which are the harmonic mass, momentum, and pressure equations, and the frequency-domain expression of Eq. (2.16) reads

$$\rho_0\sigma\hat{U} = -A\frac{d\hat{p}}{dx} + \hat{\tau}_w, \quad A\sigma\hat{p} = -\rho_0 a_0^2\frac{\partial\hat{U}}{\partial x} + \frac{\gamma_0 - 1}{\alpha_{p_0}T_0}\hat{q}. \tag{2.20}$$

Despite not having made any assumption on the fluid, Eq. (2.19) coincides with the equations proposed by [24], who used the ideal gas EoS.

2.5 Extension of Rott's Theory to Real Fluids

We employ a well known procedure [24–26], rederiving Rott's theory for a generic fluid [27], starting from the coordinate transformation

$$\xi = i\eta, \qquad \eta = \sqrt{\frac{\sigma}{\nu_0}}r = \sqrt{2i + 2\frac{\alpha}{\omega}}\frac{r}{\delta_\nu}, \tag{2.21}$$

which is a generalization of the case $\alpha \ll \omega$ ($\sigma \approx i\omega$) [24–27], for which $\eta = \sqrt{2i}r/\delta_\nu = (i+1)r/\delta_\nu$, allows to rewrite the harmonic momentum equation as

$$\xi^2\frac{\partial^2\widehat{u}_*}{\partial\xi^2} + m\xi\frac{\partial\widehat{u}_*}{\partial\xi} + \xi^2\,\widehat{u}_* = 0, \tag{2.22}$$

where $\widehat{u}_* = -\sigma\rho_0\hat{u}/\left(d\hat{p}/dx\right) - 1$. Eq. (2.22), in the case of $m = 1$, is a Bessel's differential equation of order 0. Eq. (2.22) has the general solution

$$(m=1): \quad \widehat{u}_*(\xi) = -\frac{J_0(\xi)}{J_0(\xi_b)}, \qquad (m=0): \quad \widehat{u}_*(\eta) = -\frac{\cosh(\eta)}{\cosh(\eta_b)} \tag{2.23}$$

where J_0 is the Bessel function of the first kind of order 0, the subscript b indicates evaluation at $r = h/2$, i.e. $\eta_b = \sqrt{\sigma/\nu_0}h/2$, and the no-slip boundary condition

has been taken into account ($\widehat{u}_*(\xi_b) = \widehat{u}_*(\eta_b) = -1$). Therefore the solution of the momentum equation and the wall shear stress in frequency domain are

$$\hat{u} = -\frac{1}{\sigma\rho_0}\frac{d\hat{p}}{dx}\left(\widehat{u}_* + 1\right), \qquad \hat{\tau}_w = A\frac{d\hat{p}}{dx}f_\nu, \tag{2.24}$$

and the first of Eq. (2.20) is

$$\sigma\hat{U} = -\frac{A}{\rho_0}\frac{d\hat{p}}{dx}\left(1 - f_\nu\right), \tag{2.25}$$

where

$$(m=1): \quad f_\nu = \frac{2}{\xi_b}\frac{J_1(\xi_b)}{J_0(\xi_b)}, \qquad (m=0): \quad f_\nu = \frac{\tanh(\eta_b)}{\eta_b}. \tag{2.26}$$

The linearized harmonic EoS,

$$\gamma_0\frac{\hat{p}}{\rho_0{a_0}^2} = \frac{\hat{\rho}}{\rho_0} + \alpha_{p_0}\hat{T}, \tag{2.27}$$

evaluated at the walls, where isothermal boundary conditions ($\hat{T}_w = 0$) are applied, becomes

$$\hat{\rho}_w = \frac{\gamma_0}{{a_0}^2}\hat{p}, \tag{2.28}$$

where we used the independency of $\hat{p}$ from r. Using Eq. (2.21), the harmonic pressure equation becomes

$$\frac{\partial^2}{\partial\xi^2}(\hat{\rho} - \hat{\rho}_w) + \frac{m}{\xi}\frac{\partial}{\partial\xi}(\hat{\rho} - \hat{\rho}_w) + \mathrm{Pr}_0(\hat{\rho} - \hat{\rho}_w) = -\mathrm{Pr}_0\frac{\gamma_0 - 1}{{a_0}^2}\hat{p} - \frac{\mathrm{Pr}_0}{\sigma}\hat{u}\frac{d\rho_0}{dx}, \tag{2.29}$$

that is the inhomogeneous analog of Eq. (2.22). To revert back to an homogeneous equation, we assume a solution of the form

$$(\hat{\rho} - \hat{\rho}_w) = \frac{\rho_0\Theta}{\sigma}\frac{\mathrm{Pr}_0}{1 - \mathrm{Pr}_0}\hat{u}\left(\xi\right) + (\rho - \hat{\rho}_w)_2, \tag{2.30}$$

where we assumed $\mathrm{Pr}_0 \neq 1$ everywhere axially, obtaining from Eq. (2.29) the equation

$$\begin{aligned} \tilde{\xi}^2\frac{\partial^2\widehat{\rho}_*}{\partial\tilde{\xi}^2} + m\tilde{\xi}\frac{\partial\widehat{\rho}_*}{\partial\tilde{\xi}} + \tilde{\xi}^2\widehat{\rho}_* = 0, \qquad \tilde{\xi} = \xi\sqrt{\mathrm{Pr}_0}, \\ \widehat{\rho}_* = -(\hat{\rho} - \hat{\rho}_w)_2\left(\frac{\gamma_0 - 1}{{a_0}^2}\hat{p} + \frac{\Theta}{(1 - \mathrm{Pr}_0)\sigma^2}\frac{d\hat{p}}{dx}\right)^{-1} - 1, \end{aligned} \tag{2.31}$$

which can be solved with a solution of the form of Eq. (2.23) replacing ξ with $\tilde{\xi}$, taking advantage of the wall boundary conditions:

$$(m=1): \quad \widehat{\rho}_*(\xi) = -\frac{J_0(\xi\sqrt{\mathrm{Pr}_0})}{J_0(\xi_b\sqrt{\mathrm{Pr}_0})}, \qquad (m=0): \quad \widehat{\rho}_*(\eta) = -\frac{\cosh(\eta\sqrt{\mathrm{Pr}_0})}{\cosh(\eta_b\sqrt{\mathrm{Pr}_0})}. \tag{2.32}$$

We can therefore write the harmonic density equation:

$$\hat{\rho} - \hat{\rho}_w = -(\mathcal{R} + \hat{p}(\gamma_0 - 1)/{a_0}^2)(\widehat{\rho}_* + 1) + \mathcal{R}\mathrm{Pr}_0(\widehat{u}_* + 1), \tag{2.33}$$

where

$$\mathcal{R} = \frac{\Theta/\sigma^2}{1-\mathrm{Pr}_0}\frac{d\hat{p}}{dx}. \tag{2.34}$$

Here, as noticed before, the derivation of Rott, performed under the assumption of ideal gases, still holds for a generic fluid, in the case of $\mathrm{Pr}_0 \neq 1$.

We can now evaluate the wall heat flux in the frequency domain,

$$\hat{q} = \sigma A \frac{c_{p_0}}{\alpha_{p_0}} \left(-\frac{\Theta}{(1-\mathrm{Pr}_0)\sigma^2}\frac{d\hat{p}}{dx}(f_k - f_\nu) - \frac{\gamma_0 - 1}{a_0^2}\hat{p} f_k \right), \tag{2.35}$$

where notice that the term $1/\alpha_{p_0}$ reverts back to T_0 in the case of ideal gas EoS [26], and where

$$(m=1): \quad f_k = \frac{2}{\xi_b\sqrt{\mathrm{Pr}_0}}\frac{J_1(\xi_b\sqrt{\mathrm{Pr}_0})}{J_0(\xi_b\sqrt{\mathrm{Pr}_0})}, \qquad (m=0): \quad f_k = \frac{\tanh(\eta_b\sqrt{\mathrm{Pr}_0})}{\eta_b\sqrt{\mathrm{Pr}_0}}. \tag{2.36}$$

Eq.s (2.26) and (2.36) define the thermoviscous functions.

Finally, the pressure equation in harmonic form can be written as

$$\sigma\hat{p} = \frac{\rho_0 a_0^2/A}{1 + (\gamma_0 - 1)f_k}\left(\frac{\Theta(f_k - f_\nu)}{(1-f_\nu)(1-\mathrm{Pr}_0)} - \frac{d}{dx}\right)\hat{U}. \tag{2.37}$$

In summary, from the governing equations it is possible [24, 27, 28] to obtain, for a generic duct, the frequency-domain equations for the complex volumetric flow rate $\hat{U}$ and pressure $\hat{p}$,

$$\sigma\hat{U} = -\frac{A}{\rho_0 F_\nu}\frac{d\hat{p}}{dx}, \tag{2.38a}$$

$$\sigma\hat{p} = \frac{\rho_0 a_0^2}{A F_k}\left(\Theta\Phi_{\mathcal{P}} - \frac{\mathrm{d}}{\mathrm{d}x}\right)\hat{U}, \tag{2.38b}$$

where $\sigma = \alpha + i\omega$ is the complex eigenvalue with growth rate α and angular frequency ω, and

$$\Phi_{\mathcal{P}} = \frac{1}{1-\mathrm{Pr}_0}\frac{f_k - f_\nu}{1-f_\nu}, \qquad F_\nu = \frac{1}{1-f_\nu}, \qquad F_k = 1 + (\gamma_0 - 1)f_k, \tag{2.39}$$

where the thermoviscous functions f_ν and f_k depend on σ, the duct geometry, Prandtl number, and kinematic viscosity (see Eq.s (2.26) and (2.36)). Base state quantities are a function of the axial coordinate x only and are denoted with a subscript 0; a_0 is the isentropic speed of sound, $\nu_0 = \mu_0/\rho_0$ is the kinematic viscosity, $\gamma_0 = c_{p_0}/c_{v_0}$ is the ratio of specific heats, and $\mathrm{Pr}_0 = c_{p_0}\mu_0/k_0$ is the Prandtl number. Furthermore, A is in general the cross-sectional area of the duct, but is intended per unit depth for the geometry employed in this study.

Eq.s (2.38a) and (2.38b) are discretized on a staggered uniform grid with second order numerical operators [25, 26] and solved with a shift-Arnoldi algorithm. For all the results in this document, we will always refer to the first mode of oscillation of the system.

2.6 Acoustic Energy Budgets

Multiplying Eq. (2.38a) by $\hat{U}^*$ and (2.38b) by $\hat{p}^*$, where a superscript $*$ indicates complex conjugate, yields, after rearranging,

$$\sigma\overline{\kappa}F_\nu A = -\frac{1}{2}\frac{d\hat{p}}{dx}\hat{U}^*, \tag{2.40a}$$

$$\sigma\overline{\varepsilon}F_k A = \frac{\Theta\Phi_{\mathcal{P}}}{2}\hat{U}\hat{p}^* - \frac{1}{2}\hat{p}^*\frac{d\hat{U}}{dx}, \tag{2.40b}$$

which are the equations for the acoustic kinetic energy density and acoustic potential energy density, respectively defined by

$$\overline{\kappa} = \frac{\rho_0}{2}\frac{|\hat{U}|^2}{A^2}, \qquad \overline{\varepsilon} = \frac{1}{2}\frac{|\hat{p}|^2}{\rho_0 a_0^2}, \tag{2.41}$$

both with units of energy per unit volume. Taking the real part of the addition of Eq. (2.40a) with Eq. (2.40b), and using the properties $\Re\{\phi\psi\} = \Re\{\phi\}\Re\{\psi\} - \Im\{\phi\}\Im\{\psi\}$, and $\Re\{\phi - \phi^*\} = 0$, where ϕ, ψ are two generic complex numbers, yields

$$\alpha\overline{\mathcal{E}} + \frac{d\overline{\dot{W}}}{dx} = \overline{\mathcal{P}} - \overline{\mathcal{D}}, \tag{2.42}$$

where the acoustic energy density is defined as

$$\overline{\mathcal{E}} = A(\Re\{F_\nu\}\,\overline{\kappa} + \Re\{F_k\}\,\overline{\varepsilon}), \tag{2.43}$$

which has dimensions of an energy per unit length, the acoustic power is

$$\overline{\dot{W}} = \frac{1}{2}\Re\{\hat{p}\,\hat{U}^*\}, \tag{2.44}$$

which has dimensions of an energy per unit time, the production of acoustic energy density is

$$\overline{\mathcal{P}} = \frac{\Theta}{2}\left[\Re\{\Phi_\mathcal{P}\}\,\Re\left\{\hat{p}^*\hat{U}\right\} - \Im\{\Phi_\mathcal{P}\}\,\Im\left(\hat{p}^*\hat{U}\right\}\right], \tag{2.45}$$

and its dissipation is

$$\overline{\mathcal{D}} = -\omega A(\Im\{F_\nu\}\,\overline{\kappa} + \Im\{F_k\}\,\overline{\varepsilon}), \tag{2.46}$$

both with dimensions of power per unit length.

$$\Phi_\mathcal{P}^T = \Re\left(\Phi_\mathcal{P}\right), \quad \Phi_\mathcal{P}^S = \Im\left(\Phi_\mathcal{P}\right), \tag{2.47}$$

where $\Phi_\mathcal{P}^T$ and $-\Phi_P^S$ weigh the traveling-wave, $\mathrm{Re}(\hat{p}^*\hat{U})$, and the standing-wave, $\mathrm{Im}(\hat{p}^*\,\hat{U})$, contributions to the thermoacoustic energy production, and

$$\Phi_\mathcal{D}^q = -\Im\left(f_k\right), \quad \Phi_\mathcal{D}^\tau = \Im\left(-f_\nu/(1-f_\nu)\right), \tag{2.48}$$

represent losses due to wall heat and wall shear, respectively. In our derivation, we absorbed the dependency to $(1-\mathrm{Pr}_0)$ in Eq. (2.39), included thermoviscous effects in the acoustic energy density definition in Eq. (2.43), and generalized the expressions for geometrical configurations where more than one thermoacoustic unit is present, for an arbitrary duct geometry, and accounting for area change as well, and for a generic

fluid. It can be shown that the weights of $\Re\left\{\hat{p}^*\hat{U}\right\}$ and $\Im\left\{\hat{p}^*\hat{U}\right\}$ in Eq. (2.45) always contribute positively overall to the thermoacoustic production regardless of the sign of $(1-\mathrm{Pr}_0)$.

Integrating Eq. (2.42) axially along the domain yields

$$\alpha = \mathcal{R}/\Sigma, \tag{2.49}$$

where the Rayleigh index [26] is

$$\mathcal{R} = \int_0^L \left(\overline{\mathcal{P}} - \overline{\mathcal{D}}\right) dx, \tag{2.50}$$

and the total acoustic energy is

$$\Sigma = \int_0^L \overline{\mathcal{E}} dx, \tag{2.51}$$

and where hard-wall boundary conditions have been taken into account (the acoustic power is zero at $x = 0$ and $x = L$).

All the thermoviscous functions and the quantities in Eq.s (2.47) and (2.48) vary with the ratio of regenerator half-width $h/2$ to the Stokes boundary layer thickness δ_ν (figures 2.3 and 2.4), where the viscous and thermal boundary layers δ_ν, δ_k are defined by

$$\delta_\nu^2 = \frac{2\nu_0}{\omega}, \quad \delta_k^2 = \frac{2k_0}{\omega\rho_0 c_{p_0}}, \quad \delta_\nu = \sqrt{\mathrm{Pr}_0}\delta_k. \tag{2.52}$$

In the case of $\mathrm{Pr}_0 = 1$, $f_k = f_\nu$, and for a rectilinear geometry

$$\lim_{\mathrm{Pr}_0 \to 1} \Phi_{\mathcal{P}} = \frac{1}{2}\left(-1 + \frac{\eta_b^2 f_\nu^2}{1 - f_\nu}\right), \tag{2.53}$$

If instead $\mathrm{Pr}_0 = 0$, $f_k = 1$, and

$$\lim_{\mathrm{Pr}_0 \to 0} \Phi_{\mathcal{P}} = 1, \tag{2.54}$$

indicating that $\Phi_{\mathcal{P}}^T = 1$ and $-\Phi_{\mathcal{P}}^S = 0$, so that the production due to standing waves is null.

Having a Prandtl number close to 0 entails high thermoacoustic production over a wide range of $h/(2\delta_\nu)$, but for $\mathrm{Pr}_0 > 1$, $\Phi_{\mathcal{P}}^T$ tends to $\mathrm{Pr}_0 - 1$ for $h/(2\delta_\nu) = 0$, decreasing much faster than the $\mathrm{Pr}_0 = 0$ curve for increasing $h/(2\delta_\nu)$.

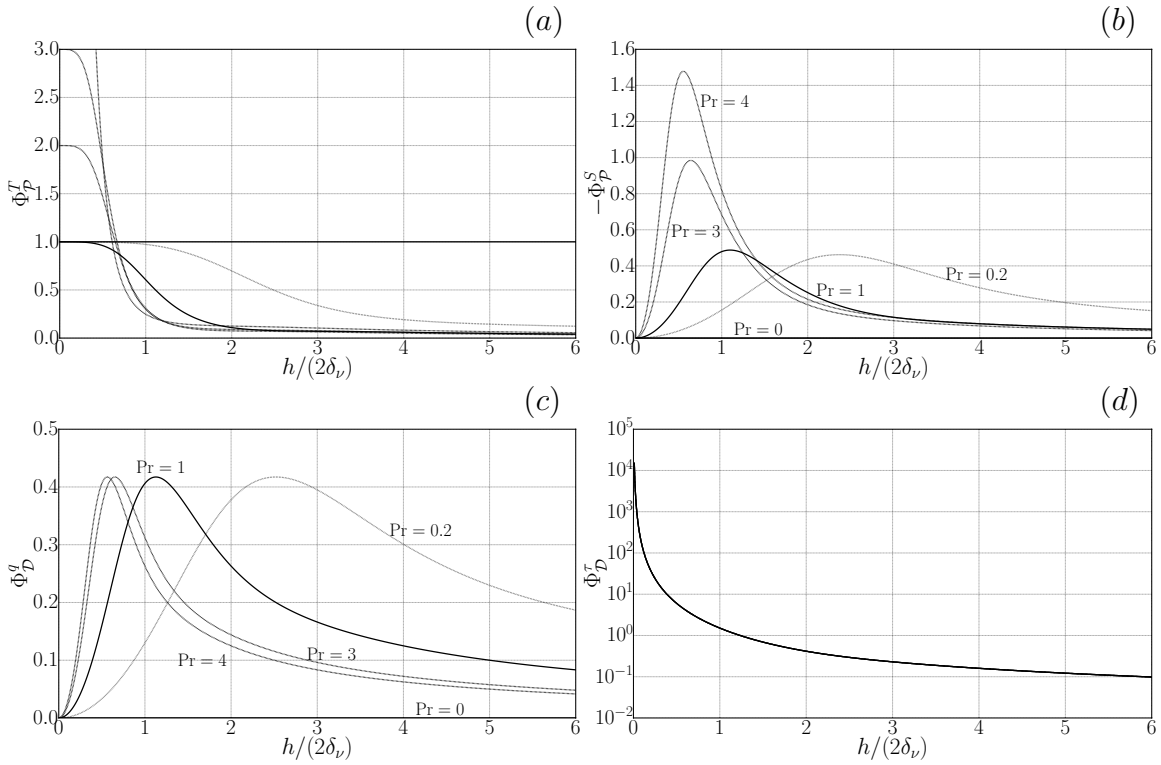

Figure 2.3. Prefactors $\Phi^T_{\mathcal{P}}$ (a) and $\Phi^S_{\mathcal{P}}$ (b) in Eq. (2.47) for rectilinear geometry versus dimensionless pore size at different Prandtl numbers. Prefactors $\Phi^q_{\mathcal{D}}$ (c) and $\Phi^\tau_{\mathcal{D}}$ (d)in Eq. (2.48) for rectilinear geometry versus dimensionless pore size at different Prandtl numbers.

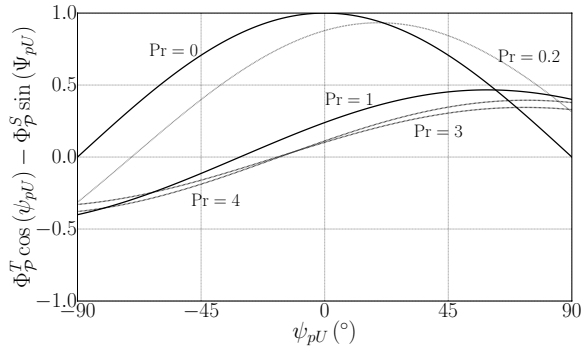

Figure 2.4. Normalized thermoacoustic production, $2A\overline{\mathcal{P}}/\Theta$ for rectilinear geometry, versus phase angle $\psi_{pU} = \angle\hat{U} - \angle\hat{p}$ for $h/(2\delta_\nu) = 1.5$.

2.7 Thermoacoustic Total Energy Budgets

The evolution equation for total energy in two dimensions reads

$$\frac{\partial \rho E}{\partial t}+\frac{\partial \rho H u}{\partial x}+\frac{\partial \rho H v}{\partial y}=\frac{\partial u_i \tau_{i1}}{\partial x}+\frac{\partial u_i \tau_{i2}}{\partial y}-\frac{\partial q_1}{\partial x}-\frac{\partial q_2}{\partial y}, \tag{2.55}$$

where $E=e+(u^2+v^2)/2$ is the specific total energy, sum of specific internal energy and specific kinetic energy, $H=E+p/\rho$ is the specific total enthalpy. Integrating Eq. (2.55) across the stack pore area, for a 2D rectilinear geometry, yields

$$\frac{\partial}{\partial t}\int_{-h/2}^{h/2}\rho E dy+\frac{\partial}{\partial x}\int_{-h/2}^{h/2}\rho H u dy=\int_{-h/2}^{h/2}\frac{\partial u_i \tau_{i1}}{\partial x}dy-\frac{\partial}{\partial x}\int_{-h/2}^{h/2}q_1 dy-[q_2]_{-h/2}^{h/2}, \tag{2.56}$$

where we accounted for $u=v=0$ at $y=\pm h/2$. Introducing the cycle averaging operator,

$$\overline{(\cdot)}=\frac{\omega}{2\pi}\int_0^{2\pi/\omega}(\cdot)\mathrm{d}t, \tag{2.57}$$

where time 0 indicates the beginning of an acoustic cycle, Eq. (2.56) becomes

$$\int_{-h/2}^{h/2}\frac{[\rho E]_0^{2\pi/\omega}}{2\pi/\omega}dy+\frac{\partial}{\partial x}\int_{-h/2}^{h/2}\left(\overline{\rho H u}+\overline{q_1}\right)dy=\int_{-h/2}^{h/2}\overline{\frac{\partial u_i\tau_{i1}}{\partial x}}dy-[\overline{q_2}]_{-h/2}^{h/2}. \tag{2.58}$$

Scaling arguments provided by [29] allow to neglect the energy change due to viscous dissipation, first term on the right hand side of Eq. (2.58), which, neglecting terms of third order, becomes

$$-[\overline{q_2}]_{-h/2}^{h/2}=\int_{-h/2}^{h/2}\frac{[\rho E]_0^{2\pi/\omega}}{2\pi/\omega}dy+\frac{\partial\overline{\dot{\mathcal{H}}}}{\partial x}, \tag{2.59}$$

where

$$\overline{\dot{\mathcal{H}}}=\int_{-h/2}^{h/2}\left(\overline{\rho h u}dy-\overline{k\frac{\partial T}{\partial x}}\right)dy \tag{2.60}$$

is the fluid's time-averaged total energy flux. Integrating Eq. (2.59) axially along the stack, with 1 indicating the axial coordinate of its beginning and 2 its end, yields

$$\overline{\dot{Q}}=\int_1^2\int_{-h/2}^{h/2}\frac{[\rho E]_0^{2\pi/\omega}}{2\pi/\omega}dydx+\overline{\dot{\mathcal{H}}}_2-\overline{\dot{\mathcal{H}}}_1, \tag{2.61}$$

where the time-averaged heat exchange through the walls is

$$\overline{\dot{Q}}=-\int_1^2[\overline{q_2}]_{-h/2}^{h/2}dx=2\int_1^2\overline{\left(k\frac{\partial T}{\partial y}\right)}_{h/2}dx, \tag{2.62}$$

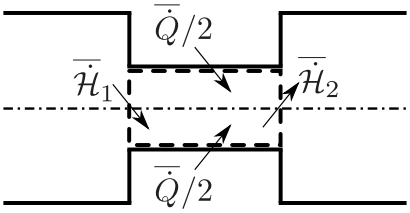

Figure 2.5. Control volume used for the total energy balance inside the stack pore.

where we assumed a symmetric temperature profile around $y = 0$. Eq. (2.61) shows that the boundary heat flux is absorbed by the fluid in the form of time-averaged total energy flux difference between stack end and beginning.

The frequency domain expression for the time-averaged energy flux (Eq. (2.60)) has been derived by [29, 30]:

$$\overline{\dot{\mathcal{H}}} = \frac{1}{2}\Re\left\{\hat{p}\hat{U}^*\left(1 - \frac{\alpha_{p_0}T_0(f_k - f_\nu^*)}{(1+\mathrm{Pr}_0)(1-f_\nu^*)}\right)\right\} + \frac{\rho_0 a_0^2 \Theta|\hat{U}|^2}{2AG_0\omega|1-f_\nu|^2}\Im\left\{\frac{f_\nu^*\mathrm{Pr}_0 + f_k}{1-{\mathrm{Pr}_0}^2}\right\} + H_k, \tag{2.63}$$

where

$$H_k = -Ak_0\frac{\mathrm{d}T_0}{\mathrm{d}x} \tag{2.64}$$

is the conduction heat, and where

$$G = \frac{\alpha_p a^2}{c_p} = \frac{\gamma - 1}{\alpha_p T}, \tag{2.65}$$

is the Grüneisen parameter, which reverts to $\gamma - 1$ for ideal gases, and which is used by [27] as the ratio between the work parameter $\gamma - 1$ and the heat parameter $\alpha_p T$. For our configuration, due to the inviscid hot cavity and resonator, $\overline{\dot{\mathcal{H}}}$ is equal to the acoustic power outside the stack.

2.8 A non-iterative Method to Get Temperature from Conserved Variables

Fully conservative Navier-Stokes simulations of real-fluid flows are used widely in the literature [21, 31–33]. The use of fully conservative simulations with highly nonlinear equations of state is not recommended for problems involving contact discontinuities, because of the well known issue of loss of mechanical equilibrium [34–37], as we will see in chapter 3, but is mandatory for flows involving shock waves [37]. In fact, it has been proposed [37] that a hybrid approach solving for primitive variables in most of the flow field and for conserved variables in regions where shocks are present would be effective for real-fluid simulations. Nevertheless, for some problems (e.g. flows of supercritical fluids not too close to the critical point), the loss of mechanical equilibrium gives rise to spurious pressure oscillations that are either not significant enough or do not compromise the validity and stability of the calculations [21, 33], especially if artificial viscosity is included, and are anyways eliminated with grid refinement [38]. Therefore, fully conservative Navier-Stokes are and will be used in the future even if coupled with nonlinear equations of state.

Solving the evolution equations for conserved variables implies the need for temperature and pressure appearing in the fluxes to be computed from them at every sub-time step. The routine that solves for temperature T from density ρ and internal energy per unit mass e ($T = T(\rho, e)$) can be very computationally expensive (if not the most expensive) because the highly nonlinear nature of $e = e(T)$ for a fixed ρ requires the use of iterative methods (e.g. Newton-Raphson, NR) [34]. In fact, it has been reported [39] that the Peng-Robinson equation of state is 100 times slower that the ideal gas equation of state. Concerns of performance are hence raised and attention on how $T = T(\rho, e)$ is handled can potentially ensure great reductions of computational time.

Here we propose an alternative method to obtain T from ρ and e. The main idea is to redefine the ideal gas specific caloric coefficients so that the relation $T = T(\rho, e)$ can

be solved analytically. With the proposed method we obtain temperature from ρ, e without Newton-Raphson-like iterations (and related user-input parameters) ensuring considerable computational speed-up and machine precision accuracy of T. We apply this idea to single-component fluids modeled with the following EoSs: IG (ideal gas), vdW (van der Waals), SRK (Soave-Redlich-Kwong), PR (Peng-Robinson).

A generic two-parameters cubic EoS can be recast as [40, 41]:

$$p = \frac{\rho R T}{1 - \rho b} - \frac{\rho^2 \alpha_{cr} \alpha}{(1 - \rho c_1 b)(1 - \rho c_2 b)} \tag{2.66}$$

where $R = R_u / M_m$, M_m is the molar mass, $R_u = 8.314472\,\mathrm{J \cdot mol^{-1} K^{-1}}$ is the universal gas constant, c_1, c_2 are real constants, α is chosen as the one proposed by Soave [42]:

$$\alpha = \left[1 + \beta \left(1 - \sqrt{T/T_{cr}}\right)\right]^2 = F^2 T - 2GF\sqrt{T} + G^2, \tag{2.67}$$

where $\alpha(T_{cr}) = 1$, $F = \beta/\sqrt{T_{cr}}$, $G = \beta + 1$. This paper deals with the EoSs described by the parameters in table 2.2.

Table 2.2.
EoS-specific parameters for Eq. (2.66).

EoS	$\alpha_{cr} M_m^2 p_{cr} / (R_u^2 T_{cr}^2)$	$b p_{cr} / (R_u T_{cr})$	c_1	c_2
IG	0	0	0	0
vdW	27/64	1/8	0	0
SRK	$1/(9(2^{1/3} - 1))$	$(2^{1/3} - 1)/3$	0	-1
PR	≈ 0.457236	≈ 0.0777961	$-1 - \sqrt{2}$	$-1 + \sqrt{2}$

EoS	β
IG	0
vdW	0
SRK	$0.480 + 1.574\omega - 0.176\omega^2$
PR	$0.37464 + 1.54226\omega - 0.26992\omega^2$

The specific internal energy e can be computed [20] with the following expression:

$$e = e^0 - \int_0^\rho \left(T \frac{\partial p}{\partial T}\Big|_\rho - p \right)_T \frac{d\rho}{\rho^2} = e^0 + \alpha_{cr} Y \left(T \frac{\mathrm{d}\alpha}{\mathrm{d}T} - \alpha \right) = e^0 + \alpha_{cr} Y \left(GF\sqrt{T} - G^2 \right), \tag{2.68}$$

where we used Eq. (2.67) and

$$Y = \int_0^\rho \frac{d\rho}{(1-\rho c_1 b)(1-\rho c_2 b)} = \begin{cases} \rho & \text{vdW} \\ \dfrac{1}{b(c_2-c_1)} \ln\left(\dfrac{1-\rho b c_1}{1-\rho b c_2} \right) & \text{SRK, PR} \end{cases} \tag{2.69}$$

and the superscript 0 denotes ideal gas quantities. Eq. (2.68) can be a highly non-linear function of temperature. The reason for this is not the term multiplying $\alpha_{cr} Y$, but the reference ideal gas internal energy e^0. In fact, Poling et al. [20] and NASA polynomials [cit] provide a polynomial expression for e^0 of degree five in T. Since $\sqrt{T}$ is present in Eq. (2.68), the polynomial is in general of order ten and requires iterative techniques (e.g. Newton-Raphson method) to be solved for $\sqrt{T}$. Notice that this is true also for thermally perfect IG and for vdW EoSs but not for the calorically perfect IG EoS.

For a fixed ρ, $\sqrt{T}$ can be computed analytically from Eq. (2.68) if the latter is at maximum a polynomial of order four in $\sqrt{T}$. It is this observation that leads to the following definitions:

$$c_p^0/R = c_0/\sqrt{T} + c_1 + c_2\sqrt{T} + c_3 T, \qquad h^0 = h_0 + h_1\sqrt{T} + h_2 T + h_3 T^{3/2} + h_4 T^2 \tag{2.70}$$

where the IG enthalpy is $h^0 = e^0 + R(T - T_{ref}) = h_{ref} + \int_{T_{ref}}^T c_p^0 dT$, $h_1 = 2Rc_0$, $h_2 = Rc_1$, $h_3 = 2Rc_2/3$, $h_4 = Rc_3/2$, and $h_0 = h_{ref} - h_1\sqrt{T_{ref}} - h_2 T_{ref} - h_3 T_{ref}^{3/2} - h_4 T_{ref}^2$. The first of Eq. (2.70) has been fitted (minimizing the root mean square error) trough experimental c_p^0 values [20] in order to obtain the values of c_i for $i = 0, 1, 2, 3$ reported in table 2.3 for some fluids. Figure 2.6 shows that Eq. (2.70) has satisfactory performance in replicating established experimental values.

The change of the functional dependence of c_p^0 on T hence does not impact validity of the pointwise values and, more importantly, allows to write Eq. (2.68) as

$$e = h_0 + RT_{ref} + h_1\sqrt{T} + (h_2 - R)T + h_3 T^{3/2} + h_4 T^2 + \alpha_{cr} Y \left(GF\sqrt{T} - G^2 \right), \tag{2.71}$$

Table 2.3.
Ideal gas isobaric thermic coefficient c_p^0 for the first of Eq. (2.70). Validity range is $50-1000$ K for all fluids, a part from R-218 and FC-72, for which it is $200-1000$ K.

species	$c_0\,(\mathrm{K}^{1/2})$	c_1	$c_2\,(\mathrm{K}^{-1/2})$	$c_3\,(\mathrm{K}^{-1})$
N_2	-3.42882	4.47527	$-8.32912\cdot10^{-2}$	$2.21125\cdot10^{-3}$
O_2	6.35435	2.49365	$2.94819\cdot10^{-2}$	$6.14998\cdot10^{-4}$
CO_2	$3.07600\cdot10^{1}$	-3.95446	$4.94522\cdot10^{-1}$	$-6.22984\cdot10^{-3}$
Xe	0	2.5	0	0
H_2O	5.67997	3.54438	$-2.24653\cdot10^{-2}$	$1.89775\cdot10^{-3}$
Methanol	$4.96352\cdot10^{1}$	-5.14533	$4.31377\cdot10^{-1}$	$9.01708\cdot10^{-4}$
R-134a	$9.74481\cdot10^{1}$	$-2.15547\cdot10^{1}$	1.98495	$-2.61853\cdot10^{-2}$
R-218	$1.52131\cdot10^{1}$	$-1.70374\cdot10^{1}$	2.65459	$-3.96511\cdot10^{-2}$
FC-72	$-2.83300\cdot10^{1}$	$-2.16350\cdot10^{1}$	4.38248	$-6.48505\cdot10^{-2}$

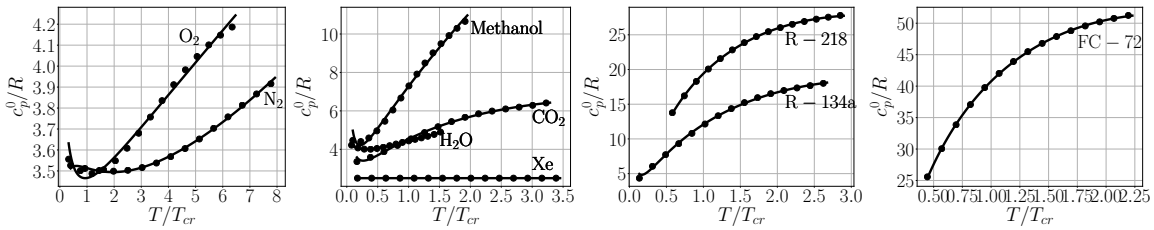

Figure 2.6. Ideal gas isobaric thermic coefficient c_p^0 from the first of Eq. (2.70) using values from table 2.3 (solid lines) and reference data (using polynomial c_p^0 from Poling [20]) (circles).

which is a polynomial equation of the type $e(\rho,\sqrt{T})=0$ of order four in $\sqrt{T}$:

$$A(\sqrt{T})^4+B(\sqrt{T})^3+C(\sqrt{T})^2+D\sqrt{T}+E=0, \tag{2.72}$$

where the coefficients of the quartic equation are

$$\begin{aligned} A = h_4, \qquad B = h_3, \qquad C = h_2 - R, \\ D = h_1 + \alpha_{cr} Y G F, \qquad E = h_0 + R T_{ref} - e - \alpha_{cr} Y G^2. \end{aligned} \tag{2.73}$$

Notice that all of the above derivations are clearly dependent on the assumption made in Eq. (2.67): other expressions of c_p^0 in Eq. (2.70) will be more useful for other functional dependences of α on T. In particular, it is the term $T\mathrm{d}\alpha/\mathrm{d}T - \alpha$ in Eq. (2.68) that gives information on a convenient form of c_p^0. Most of the coefficients of Eq. (2.72) can be precomputed ensuring good computational performance. In the case that Eq. (2.72) is not a quartic because of null h_i coefficients, the solution procedure is greatly simplified. As example, for most noble gases $c_p^0 = c_1 = const.$ (see table 2.3) and Eq. (2.72) reverts to a quadratic equation also without the method proposed in this paper.

Eq. (2.72) can be solved with analytical steps for $\sqrt{T}$ (isolating only positive and real solutions), providing the temperature T corresponding to ρ, e with machine precision error. Notice that in the case of $A \neq 0$, two real $\sqrt{T}$ values will be obtained during the solution process, and the $\sqrt{T}$ inside the validity range indicated in table 2.3 has to be taken as the only correct solution.

In case Eq. (2.70) can not reproduce trends exhibited by experimental data with high fidelity, the procedure outlined above can be used as an accurate first guess for iterative methods.

3. NUMERICAL CHALLENGES WITH HIGH-ORDER SPECTRAL DIFFERENCE SOLVERS FOR SUPERCRITICAL FLOWS

We have investigated single-component supercritical flows using the spectral difference (SD) method. We compare the use of a fully conservative approach with the solution of the pressure evolution equation: the former, violating mechanical equilibrium at contact discontinuities, can result in unstable computations, while the latter allows for fast, accurate, and robust computations in absence of shocks. We provide h- and p-convergence study for 1D entropy wave advection, showing grid refinement difficulties for the fully conservative method if conditions are too close to the critical point. We then perform 2D computations of a buoyant supercritical configuration showing the visibly altered numerical solution (up until blow-up) if a conservative approach is employed, while the non-conservative method allows to obtain a stable computation. Finally, we apply the SD discretization with both conservative and non-conservative methods to the solution of supercritical isothermall-wall channel flow, pointing out differences in turbulent statistics and flow visualizations. The material in this chapter has been presented at the AIAA Aviation Conference in 2018 [38].

3.1 Importance of Numerical Simulations of Supercritical Flows

Supercritical fluid flow computations have become essential for the design of the next generation Diesel and rocket engines, due to the increase in efficiency with their operating pressure. State of the art simulations include supercritical mixing layers [21], trans- and supercritical fluid injection [39, 43–45], transcritical non-premixed counterflows [46], large eddy simulations (LES) of channel flow or jets [33, 47, 48], and full LES of fuel-oxidizer injection in a rocket engine [49].

Fully conservative simulations of supercritical flows suffer from spurious numerical oscillations due to the well known issue of loss of mechanical equilibrium at contact and material discontinuities [36, 50]. Nevertheless, it is still possible to couple numerical tools solving explicitly for total energy with highly nonlinear equations of state [21, 32, 33, 49, 51–54] if sufficient grid resolution is employed and if the thermodynamic conditions are not too close to the critical point. In such cases, the loss of mechanical equilibrium gives rise to spurious pressure oscillations anyways, but those are either not significant enough or do not compromise the validity and stability of the calculations, especially if artificial viscosity is included, and are (slowly) eliminated with grid refinement.

To solve the problem of spurious pressure oscillations, non-conservative numerical schemes have been employed [34, 35]. In particular, the solution of mass and momentum equations in conservative form and of the pressure evolution equation has been shown [35, 55] to be fast, accurate, and robust in the numerical solution of supercritical flows.

Most of the literature in supercritical flows employs the finite volume method or the finite differences method [56–60], but scarcity of study on the Spectral Difference (SD) numerical method is found. A discontinuous Galerkin (DG) formulation has recently been used for supersonic methane jet computations [39], but no detailed information on the behavior of the numerics has been explicitly provided. Since DG and SD methods are gaining increasing attention in the community because of their ability to provide a high-order of accuracy on unstructured meshes, there is the need for an accurate comparison of fully conservative scheme with a non-conservative scheme. Furthermore, since the implementation of the pressure equation in finite volume codes is not straightforward [34], it is needed to investigate its implementation with a SD discretization.

A detailed investigation of the SD discretization performance when applied to supercritical flows is proposed in this chapter. We compare the use of a fully conservative approach against the solution of mass and momentum equations in conservative form

and of the pressure evolution equation. We provide h- and p-convergence plots for the advection of an entropy wave showing the differences in using the two methods, and then apply the numerical strategy to the solution of supercritical buoyant configuration and channel flow. We take into account single-component fluids modeled with the Peng-Robinson equation of state [18]. Table 3.1 reports critical values for the two fluids of interest in this work.

Table 3.1.
Critical pressure and temperature for Carbon dioxide and Helium.

fluid	T_{cr}(K)	p_{cr}(MPa)
CO_2	304.13	7.3773
He	5.19	0.227

3.2 Numerical Setup

The Navier-Stokes equations are solved using the spectral difference (SD) discretization. We briefly recall here the formulation on conservative variables, which is typically adopted [61–63], and which will serve as a reference for the implementation of the pressure evolution approach proposed in the present work. To achieve an efficient implementation, each element in the physical domain is transformed to a standard cubic element described by local coordinates $\boldsymbol{\xi} \equiv (\xi_1, \xi_2, \xi_3)^{\mathrm{T}}$, with $\boldsymbol{\xi} \in [-1 : 1]^3$. The governing equations in the physical domain are then transferred into the computational domain, where they take the form

$$\frac{\partial \boldsymbol{\mathcal{W}}}{\partial t} + \boldsymbol{\nabla}_{\boldsymbol{\xi}} \cdot \boldsymbol{\mathcal{F}} = \mathbf{0}, \tag{3.1}$$

with

$$\boldsymbol{\mathcal{W}} = \det(\mathbf{J})\mathbf{w}, \quad \boldsymbol{\mathcal{F}} = \mathrm{adj}(\mathbf{J}) \cdot [\mathbf{F}_{\mathrm{c}}(\mathbf{w}) - \mathbf{F}_{\mathrm{v}}(\mathbf{w}, \nabla\mathbf{w})], \tag{3.2}$$

where $\boldsymbol{\nabla_\xi} \equiv (\partial/\partial\xi_1, \partial/\partial\xi_2, \partial/\partial\xi_3)^{\mathrm{T}}$, whereas $\det(\mathbf{J})$ and $\mathrm{adj}(\mathbf{J}) = \det(\mathbf{J})\mathbf{J}^{-1}$ represent the determinant and the adjoint of the Jacobian matrix $\mathsf{J}_{ij} = \partial x_i/\partial\xi_j$, respectively. $\mathbf{w} = (\rho, \rho\mathbf{u}, \rho E)^{\mathrm{T}}$ is the vector of conservative variables. Within each standard element, two sets of points are defined, namely the solution points and the flux points.

In order to construct a degree p (resp. $p+1$) polynomial for the solution (resp. flux) along each coordinate direction, the solution (resp. flux) at $p+1$ (resp. $p+2$) points is required. Unless otherwise stated, the $p+1$ solution points in 1D are chosen to be the Gauss-Legendre quadrature points, whereas the $p+2$ flux points are the Gauss-Legendre quadrature points of order $p-1$ plus the two end points -1 and 1. Accordingly, the $p+1$ solution points are obtained as the roots of the equation

$$P_{p+1}(\xi) = \frac{2p+1}{p+1}\xi P_p(\xi) - \frac{p}{p+1}P_{p-1}(\xi) = 0, \tag{3.3}$$

where $P_{p+1}(\xi)$ is the Legendre polynomial of order $p+1$, $P_{-1}(\xi) = 0$ and $P_0(\xi) = 1$ and ξ is either ξ_1, ξ_2 or ξ_3. This particular combination of solution and flux points can be proved to be linearly stable for all orders of accuracy [64].

Using the $p+1$ solution points and the $p+2$ flux points, polynomials of degree p and $p+1$, respectively, can be built using Lagrange bases defined as

$$h_i(\xi) = \prod_{s=1, s\neq i}^{p+1} \left(\frac{\xi - \xi_s}{\xi_i - \xi_s}\right), \quad \text{and} \quad l_{i+1/2}(\xi) = \prod_{s=0, s\neq i}^{p+1} \left(\frac{\xi - \xi_{s+1/2}}{\xi_{i+1/2} - \xi_{s+1/2}}\right). \tag{3.4}$$

The first step of the SD discretization is to interpolate the vector of conservative variables from solution points to flux points using a Lagrange interpolant of degree p (Eq. (3.4)). The values of convective fluxes are then computed on the flux points from the interpolated conservative variables. Regarding the end-points contributions, a Riemann solver is employed to compute a common flux at element interfaces to ensure conservation and stability. In the current implementation, the Rusanov solver is used. Once the values of convective fluxes are known on all flux points, another Lagrange interpolant of degree $p+1$ is constructed using the flux values. The spatial derivatives of fluxes are then interpolated from flux points to solution points using the analytical expression of the Lagrange polynomial derivatives. The viscous flux

polynomial is computed accordingly to Kopriva and Sun [65, 66]. First, polynomials based on the velocity components are constructed on flux points using average values at the end points. The velocity gradients are then computed on solution points from the interpolation and derivation of the flux points velocity polynomials. Finally, the gradients are interpolated on flux points using averaged values at end points, allowing the computation of the viscous fluxes.

After the flux derivatives are known on the solution points, a third- or forth-order explicit time integration is performed via the Runge-Kutta methodology.

Regarding the thermodynamic closure, the EoSs in table 2.2 are used in order to provide a point-wise evaluation of the pressure, temperature and density. When real fluids are concerned, the thermodynamic closure given by a highly nonlinear EoS is known to yield numerical oscillations when the pressure is computed from the conservative variables. In the present work, we consider an alternate formulation for which the pressure evolution equation is solved instead of the total energy. Despite being non-conservative regarding the total energy, this approach allows for eliminating the pressure oscillations yielding stable computations for stiff, real-fluid problems. The pressure equation is solved as in Eq. (2.10). The velocity gradients and heat flux q_j are solved using the SD derivatives operator, and allow for specifying the boundary conditions trough numerical fluxes. This particular form of the pressure equation includes the convective flux pu_j solved using the Rusanov flux at the element interfaces, thus adding an amount of stabilizing numerical dissipation when the pressure is solved.

3.3 Results

3.3.1 Advection of an Entropy Wave

In this section we consider the numerical simulation of the advection of an entropy wave in supercritical Carbon dioxide by solving the 1D Euler equations. This tests if the numerical scheme respects the property of mechanical equilibrium at con-

tact discontinuities, which refers to keeping a uniform pressure and velocity across non-uniform profiles of density, temperature, and therefore entropy and all other thermodynamic quantities.

The flow field is initialized with an assigned uniform velocity field $u_0 = 1000$ m/s, a uniform pressure $p_0 = 8115030$ Pa, corresponding to $1.1p_{cr}$ for CO_2, and a temperature assigned by

$$T = T_0 - 15\exp(1 - (10x/L)^2), \tag{3.5}$$

where $L = 1\,\mathrm{m}$ is the length of the domain. The value of T_0 in Eq. (3.5) can either be $T_0 = 1.2T_{cr}$ or $T_0 = 1.5T_{cr}$, simulating thermodynamic conditions closer or farther away from the critical point, respectively.

We employ a uniform grid with N_{cv} elements and N solution points per element (corresponding to polynomial order $p = N - 1$). In this section we use RK4 time-stepping. The computation is stopped at $t = L/u_0$ and the final solution is compared to the initial condition, allowing to compute the rms error for a given quantity φ as

$$\text{rms error} = \sqrt{\frac{\int_0^L (\varphi - \varphi_{ex})^2 dx}{\int_0^L \varphi_{ex}^2 dx}}, \tag{3.6}$$

where φ_{ex} is the exact solution.

The behavior of the two different approaches, conservative versus non-conservative, regarding the pressure oscillations is assessed by plotting the pressure fluctuations at the end of the computations (figure 3.1). The discretization in this case features 10 mesh elements and a sixth-order of accuracy, for a total of 60 degrees of freedom in the spatial domain. It is seen that while the conservative approach leads to strong, point-to-point pressure oscillations, solving the pressure equation instead leads to a complete elimination of these spurious oscillations.

It is now interesting to investigate if these spurious pressure oscillations vanish with grid refinement. One way to do this is by increasing the order of accuracy of the polynomial reconstruction (p-refinement).

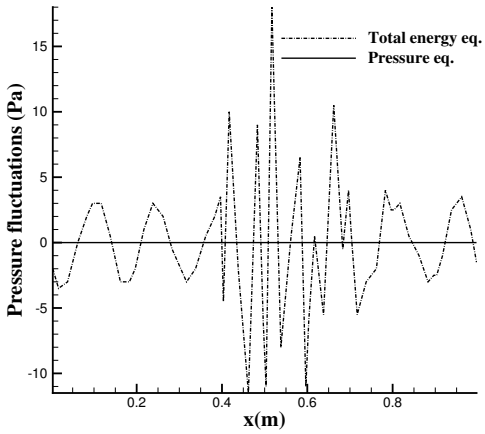

Figure 3.1. Pressure fluctuations for the advection of an entropy wave, 10 mesh elements, $p = 5$.

P-refinement (figure 3.2) entails exponential order of convergence, as expected, for the rms error in density for all cases with $T_0 = 1.5T_{cr}$. With the use of the pressure evolution equation, both the PR EoS and the non-calorically perfect EoS exhibit pressure rms errors at machine precision levels. On the other hand, when a fully conservative approach is used, spurious pressure oscillations are present, but those, for $T_0 = 1.5T_{cr}$, decrease in amplitude exponentially, following the theoretical order of convergence of the numerical scheme. Therefore, it is possible to conduct fully resolved numerical simulations employing the total energy equation coupled with a nonlinear EoS, for $T_0 = 1.5T_{cr}$. On the other hand, if $T_0 = 1.2T_{cr}$, for which the thermodynamic conditions are closer to the critical point, the PR EoS, when combined with a fully conservative approach, leads to the increase of the density rms error for higher N, leading to unstable computations. This happens because the related spurious pressure oscillations actually increase in amplitude with grid refinement. Instead, for the non-calorically perfect IG EoS, the thermodynamic nonlinearities and gradients are less severe than the PR EoS for $T_0 = 1.2T_{cr}$, allowing to obtain grid-converged solution. The pressure evolution equation, coupled with the PR EoS, yields machine precision error on pressure, and allows to obtain easily and robustly a

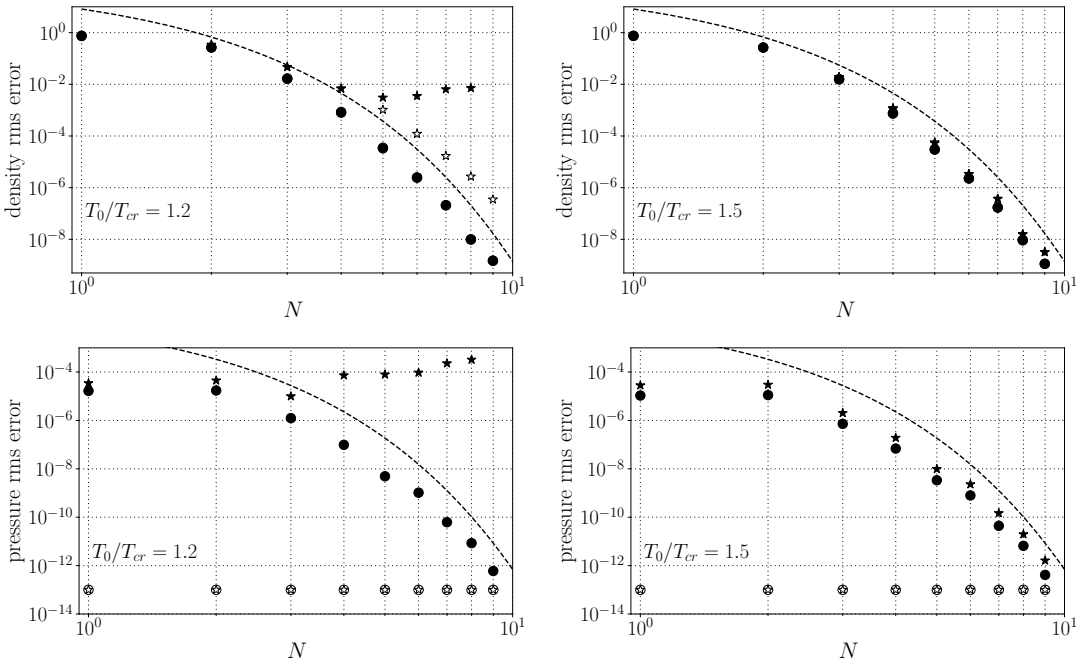

Figure 3.2. Rms density errors (top) and rms pressure errors (bottom) showing p-refinement for the advection of an entropy wave. Black star: PR EoS with ρE equation; white star: PR EoS with coupled with pressure equation; black circle: thermally (but non-calorically) perfect IG EoS with ρE equation; white circle: thermally (but non-calorically) perfect IG EoS with pressure equation. Plots on the left are for $T_0/T_{cr} = 1.2$, while on the right $T_0/T_{cr} = 1.5$ (see Eq. (3.5)). Computations are run with a uniform grid with 20 elements. Dashed line: $100e^{-2.5N}$. Cases with errors at machine precision levels are depicted at the bottom of the figures.

fully resolved computation, even for $T_0 = 1.2T_{cr}$. However, the overall error level of the PR EoS increases from $T_0 = 1.5T_{cr}$ to $T_0 = 1.2T_{cr}$, and it is always higher than the one entailed by the non-calorically perfect IG EoS. This happens because the more the conditions approach the critical point, the more the entropy wave becomes a series of two step functions for the density profiles, for the extreme case of which errors are expected to be higher, and artificial viscosity is eventually required.

In order to verify if the conclusions made above regarding the PR EoS coupled with a fully conservative approach are only valid for a p-refinement study, we now refine

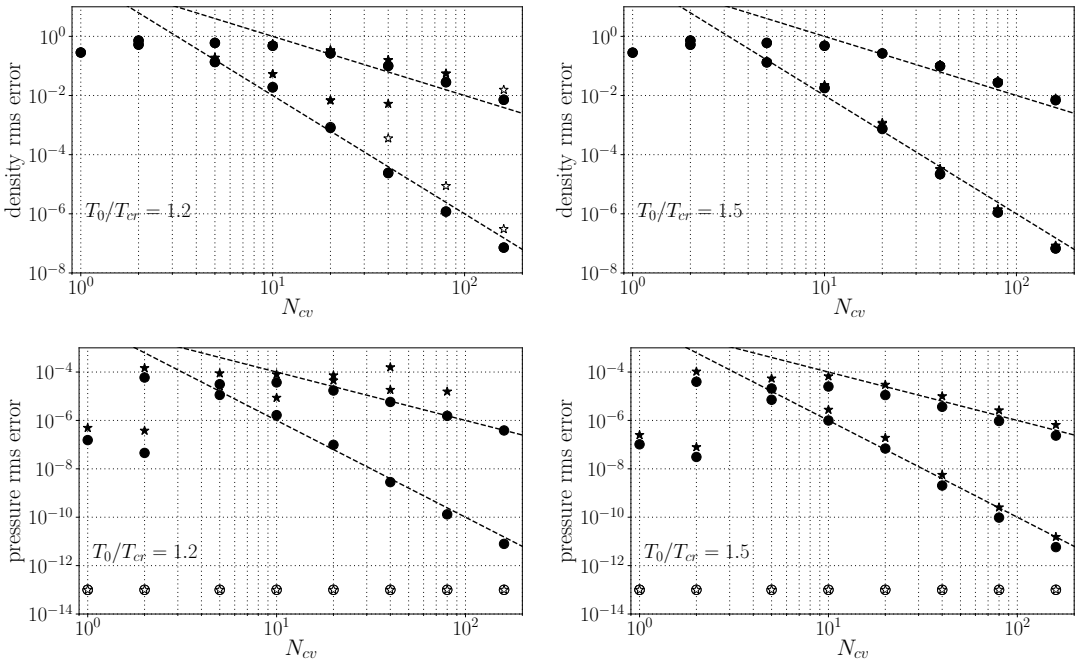

Figure 3.3. Rms density errors (top) and rms pressure errors (bottom) showing h-refinement for the advection of an entropy wave. Black star: PR EoS with ρE equation; white star: PR EoS with coupled with pressure equation; black circle: thermally (but non-calorically) perfect IG EoS with ρE equation; white circle: thermally (but non-calorically) perfect IG EoS with pressure equation. Plots on the left are for $T_0/T_{cr} = 1.2$, while on the right $T_0/T_{cr} = 1.5$ (see Eq. (3.5)). Computations are run with with $N = 2$ and $N = 4$. Dashed lines: $0.01N_{cv}^{-N}$ (top), $100N_{cv}^{-N}$ (bottom). Cases with errors at machine precision levels are depicted at the bottom of the figure.

the grid by fixing the polynomial order of accuracy ($N = 2, 4$), and increasing the number of control volumes (or elements) N_{cv} (h-refinement). H-refinement (figure 3.3) shows that, for $T_0 = 1.5T_{cr}$, the order of convergence of all cases is the one expected. However, as the p-refinement suggested already, for $T_0 = 1.2T_{cr}$ the PR EoS coupled with the total energy equation still results unstable.

Both grid refinement strategies show that using a fully conservative approach entails pressure errors due to violation of mechanical equilibrium. For a thermally perfect gas, and for the PR EoS applied far away from the critical point, these dis-

appear with the order of convergence of the numerical method. Nevertheless, when approaching the critical point, spurious pressure oscillations do not vanish with mesh refinement. Computations carried out with the calorically perfect ideal gas EoS (not shown) show the predicted order of accuracy, for both p- and h- convergence, for the density rms error and do not present numerical pressure oscillations for neither of the fully conservative or non-conservative approaches.

3.3.2 Falling Supercritical Blob

In this section we further analyze the differences between conservative and non-conservative formulations applied to the 2D Euler equations. We consider supercritical Carbon dioxide in a $[-L, L] \times [-L, L]$ box, where $L = 5$ m, initialized at uniform pressure equal to $p_0 = 8115030$ Pa $= 1.1 p_{cr}$ with the temperature distribution

$$T = T_0 - \frac{1}{8} \frac{a_0^2}{c_{p_0}} e^{1-100(x^2+y^2)/L^2}, \tag{3.7}$$

where $T_0 = 600$ K, x, y are the spatial coordinates from the center of the computational box, and a_0, c_{p_0} are the speed of sound and specific isobaric thermal capacity of CO_2 corresponding to T_0, p_0. This distribution results in blob of cold and heavy fluid in the center of the domain, which is pulled down by a gravity force $\dot{F}_y = -\rho g$, where $g = 9.81\,\mathrm{m/s^2}$ is the gravitational acceleration, in the momentum equation in the y direction (Eq. (4.5) for $i = 2$) and $v\dot{F}_y$ in the total energy equation for consistency. Notice that in the pressure evolution equation there is no need to add an additional term in order to be consistent.

Two computations are performed, considering the total energy transport (case A) and pressure transport (case B) equations, respectively (figure 3.4). The discretization features 20 mesh elements in each direction and a 6th order of accuracy for case A, yielding 120 degrees of freedom in each direction, and a 5th order of accuracy for case B, yielding 100 degrees of freedom in each direction. Case A starts to shows numerical oscillations in the flow when the variables gradients start becoming steep, ultimately leading to a blow-up of the computation. Case B remains stable and

oscillation-free for long time integration. Figure 3.4 shows the density field for the two cases at an early time, when the blob is starting to accelerate, at the moment of blob-up for case A, and at a later time. Case B shows a smooth density profile, as opposed to the spurious oscillations affecting case A. This computation shows that it is not possible to use a fully conservative approach coupled with a very nonlinear EoS without artificial viscosity or explicit filtering, if the Euler equations are solved and the flow gradients are significant.

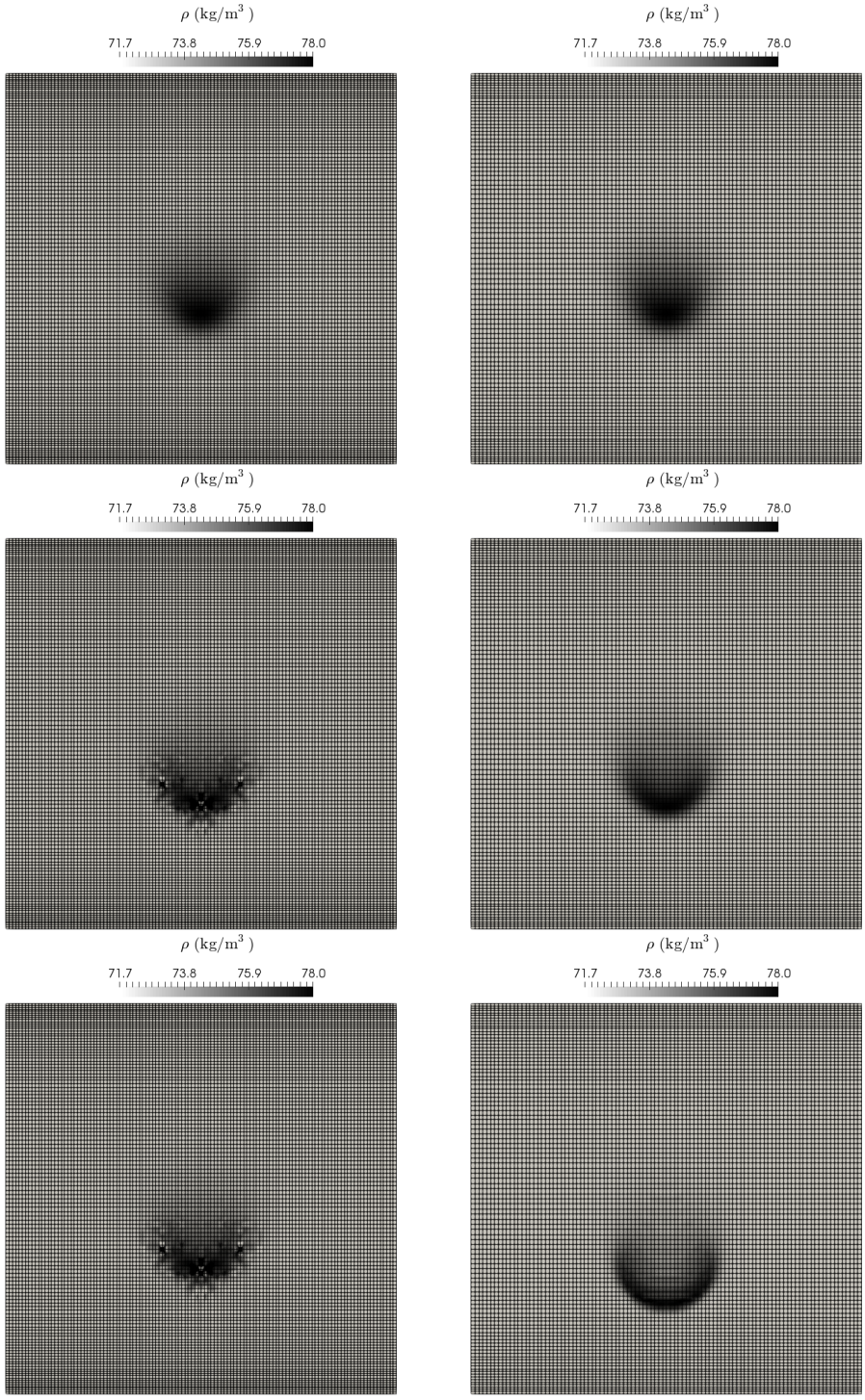

Figure 3.4. Time evolution of density during the fall of a heavy supercritical blob in a lighter environment. Comparison of solution obtained with total energy transport (left, case A) and pressure transport (right, case B).

3.3.3 Turbulent Channel Flow

In this section we perform 3D Navier-Stokes computations of a supercritical Helium periodic channel flow configuration. The computational domain is a box defined as $[0, 2\pi h] \times [-h, +h] \times [0, \pi h]$, where h is half the height of the channel set to 0.1mm. Periodic conditions are considered in the streamwise and spanwise directions, while no-slip boundary conditions are considered in the wall-normal direction at $y = \pm h$. The wall boundaries are isothermal at temperature T_w. The flow is driven by a source term $\dot{F}$ in the streamwise momentum equation that keeps the volume-averaged mass flow rate constant in the channel. A source term $u\dot{F}$ is also considered in the total energy equation for consistency.

We employ a structured mesh of size $N_x = 36$, $N_y = 24$, $N_z = 36$, with uniform spacing in x and z, and a hyperbolic tangent profile for the grid spacing in y to cluster more elements near the channel walls.

The flow is initialized with a uniform pressure $p_0 = 249700$ Pa, corresponding to $1.1p_{cr}$ for Helium, a temperature equal to T_w, and with the following velocity field:

$$u = 1.5u_0(1 - (y/h)^2), \tag{3.8}$$

$$v = 0.01u_0 \exp(-(x/L_x - 0.5)^2) \exp(-(y/2h)^2) \cos(4\pi z/L_z), \tag{3.9}$$

$$w = 0, \tag{3.10}$$

where $u_0 = 22\,\mathrm{m/s}$. The velocity profiles in Eq. (3.8) yield transition to turbulence in the channel and afterwards to a statistically steady turbulent state. The bulk Reynolds number of the flow configuration is $\mathrm{Re}_0 = \rho_0 u_0 h/\mu_0 = 5095$, and the bulk Mach number is $M_0 = u_0/a_0 = 0.131$.

Computations with $N = 3$ and $N = 4$, corresponding to second and third order reconstructing polynomials, respectively, are carried out using the pressure transport (PT) equation. Only $N = 3$ is analyzed for the fully conservative (FC) approach, because it is found to yield computational instability when ran for $N = 4$. Figure 3.5 shows the density contours for the PT and FC cases using $N = 3$. Strong unphysical oscillations in density are clearly observed for the FC case, while these are absent

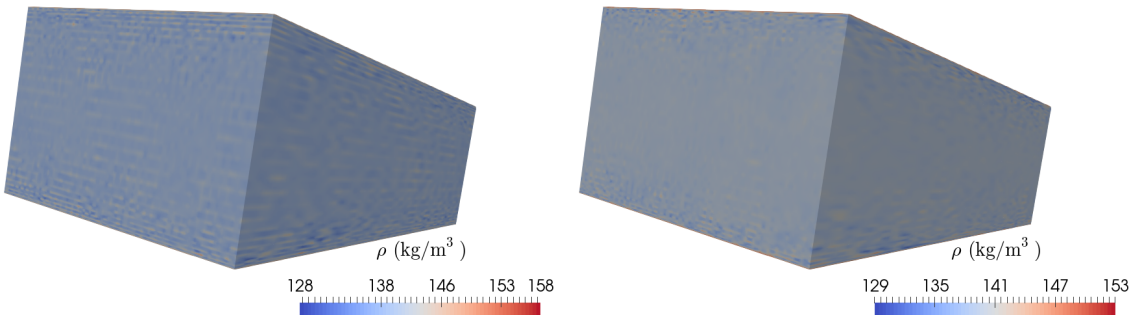

Figure 3.5. Comparison of density field obtained with the solution of the total energy equation (left) and of the pressure equation (right) for the same numerical resolution (3 points inside each element).

from the PT case. This clearly confirms the superiority of using the PT framework for high-order SD schemes compared to the FC approach when considering low-Mach number flows.

The main quantity monitored during computations is the wall friction coefficient in the x direction,

$$c_x = \frac{(\int_S \boldsymbol{\tau} \cdot \boldsymbol{n} \mathrm{dS}) \cdot \boldsymbol{i}}{\frac{1}{2}\rho_0 u_0^2 A} \tag{3.11}$$

where $\boldsymbol{\tau}$ is the viscous stress tensor, ρ_0 is the density corresponding to p_0, T_w (computed with the PR EoS), S is the solid boundary surface, $A = 10^{-8}\mathrm{m}^2$. The wall force peak indicates transition to turbulence, after which a statistical steady state is reached (figure 3.6a). If the value of $c_x = 0.325$ is multiplied by $0.5A/S = 0.02533$, where $S = 2\pi^2 h^2$, the skin friction coefficient $2\tau_w/(\rho_0 u_0^2) = 0.0076$ is obtained.

Turbulent statistics begin to be computed when the statistical steady state is reached. The mean velocity profile predicted with under resolved fully conservative computations slightly deviates from the profile obtained with the use of the pressure evolution equation, at the same numerical resolution (figure 3.6b).

From those profiles, it is observed that the wall friction is enhanced in the PT case corresponding to higher friction Reynolds number behavior compared to the FC case. This behavior is also observed for the Reynolds stresses. Indeed, the FC

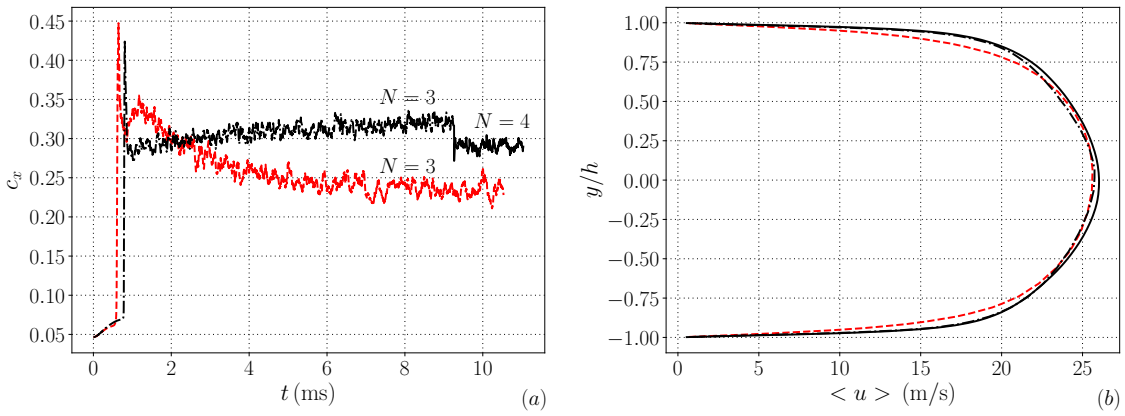

Figure 3.6. (a): wall friction coefficient (Eq. (3.11)) time evolution, (b); mean velocity profile. Dashed line: solution with total energy evolution equation for $N = 3$; dashed-dotted line: solution with pressure evolution equation for $N = 3$; solid line: solution with pressure evolution equation for $N = 4$, restarted from $N = 3$.

computation displays lower stresses intensity compared to the PT approach, implying a more intense small-scale activity for the PT case. On the coarse discretization ($N = 3$), oscillations are observed on the fluctuating profiles for both the PT and FC approaches. These oscillations seem to be more pronounced for the FC case, especially seen on the wall-normal fluctuations (Figure 3.7b). Increasing the polynomial order of the reconstructing polynomials for the SD discretization provides an efficient way to obtain grid-refined data. However, it was not possible to obtain a refined computation from third to fourth order using the total energy equation, probably because of the pressure oscillations present in the flow, which greatly compromise the stability of higher order polynomials. With the use of the pressure evolution equation, instead, the finer computation is stable and smoother profiles for the average velocity and Reynolds stresses are obtained (solid lines in figure 3.7). Also, the fact that the profiles are pretty similar, suggests that the $N = 4$ PT computation is close to grid convergence. The oscillations and blow-up observed for the $N = 3$ PT and FC and $N = 4$ FC cases, respectively, suggests that subgrid dissipation or regularization

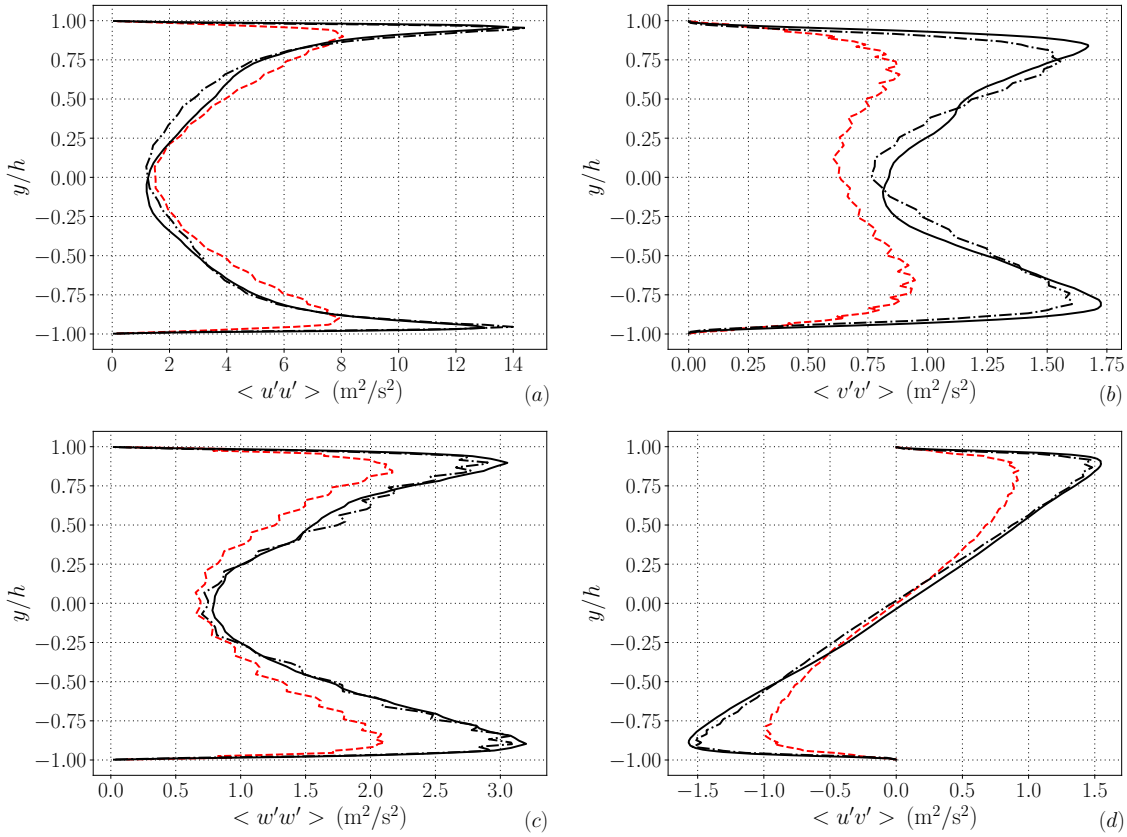

Figure 3.7. Reynolds stress components (a-d). Lines have same meaning as in figure 3.6.

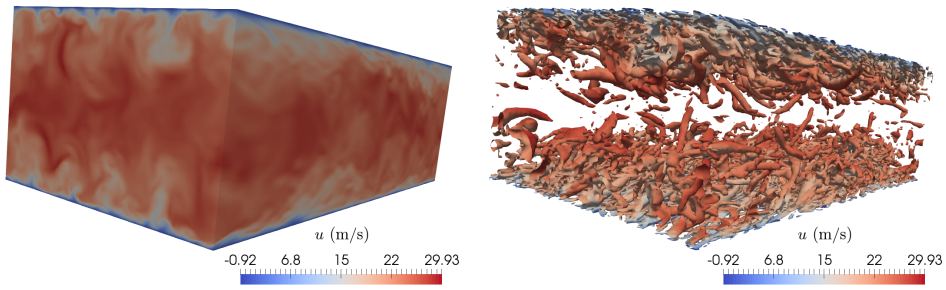

Figure 3.8. Visualization of u velocity field (left) and isosurfaces of Q-criterion (right) at $Q = 6 \cdot 10^{10}\, 1/s^2$, colored by u, obtained with the solution of the pressure equation with 4 points inside each element.

procedures might be needed in order to obtain stable and physically consistent results on coarse grids when considering gases with complex real gas effects.

To show the ability of the method to display correct flow patterns, the velocity field contours and iso-surfaces of Q-criterion are plotted in Figure 3.8 for the PT case with $N = 4$. We can observe an accurate representation of near-wall streaks as well as the ejection of worm-like structures at the core of the channel. This shows the capacity of the present PT methodology to represent accurately turbulent structures in a supercritical regime at relatively coarse resolution.

4. REAL-FLUID EFFECTS ON STANDING-WAVE THERMOACOUSTIC INSTABILITY

We have performed fully resolved high-order unstructured compressible Navier-Stokes simulations of a thermoacoustically unstable resonator employing CO_2 in transcritical conditions. The parameter space spans the range of base pressures $p_0 = 1.01 - 1.5$ p_{cr} and temperature differences $\Delta T = T_{hot} - T_{cold}$ up to 200 K, with thermodynamic and transport properties obtained from the Peng-Robinson equation of state and Chung's model. The resonator's geometry has been optimized resulting in a critical temperature difference of 23 K for $p_0 = 1.01$ p_{cr}. Strong real-fluid effects in the thermoacoustic response are observed: (i) the growth rate α needs to be included in the thermoviscous functions dependence in order to replicate Navier-Stokes results pushed to grid convergence, due to a high growth-rate-to-frequency ratio; (ii) α and frequency f vary in a nonlinear fashion with respect to p_0 and ΔT; (iii) the pressure eigenmode amplitude tends to flatten out, and the pressure-velocity phasing smoothly transitions at the average location of the pressure node; (iv) the sharp change in acoustic impedance at transcritical conditions changes locally the derivative of the eigenmodes, akin to an area change. Moreover, the acoustic and total energy budgets illustrate, for a given ΔT, the increase of the produced acoustic power, but also of the heat required, if the thermodynamic conditions approach the critical point. The limit cycle governed by nonlinear minor area losses is finally discussed, with an analysis of the thermodynamic nonlinearities peculiar of transcritical thermoacoustic oscillations at high pressure amplitudes.

4.1 Thermoacoustic Instabilities

Fluid dynamic instabilities featuring acoustic wave amplification due to the two-way coupling between pressure and heat release fluctuations [67] are known as thermoacoustic instabilities. These are intentionally triggered in thermoacoustic engines (TAEs) [29], where an external temperature differential imposed on a compact region of the device (thermoacoustic stack or regenerator) results in the spontaneous generation of acoustic power. TAEs have received much attention from the worldwide community [68–73] due to the very high energy conversion efficiency potential associated with the quasi-isentropic nature of wave energy propagation and the absence of moving parts. TAE applications span from NASA designs for deep-space energy generation [74] to small-scale CPU-generated heat control patented by Google [75].

The mechanisms driving thermoacoustic instabilities in TAEs rely on a Brayton-like thermodynamic cycle occurring inside the thermoacoustic stack [29], comprising two near-adiabatic transformations, driven by the acoustics, and two near-isobaric irreversible heat transfer transformations, which combined cause a fluid particle to experience thermal expansion/contraction at a high/low pressure, powering the instability and spontaneously converting heat into acoustic power. The operating fluid and the base state conditions, hereinafter indicated by a subscript 0, play a fundamental role during the heat-exchange phases of the cycle. Indeed, the theoretical thermoacoustic production is proportional to the thermoacoustic gain [29],

$$\Theta = -\frac{1}{\rho_0}\frac{\mathrm{d}\rho_0}{\mathrm{d}x}, \tag{4.1}$$

where x indicates the coordinate of wave propagation, and ρ_0 is the base density. If the base pressure p_0 is uniform, Eq. (4.1) reverts to

$$\Theta = \alpha_{p_0}\frac{\mathrm{d}T_0}{\mathrm{d}x}, \tag{4.2}$$

where T_0 is the base temperature and

$$\alpha_p = -\frac{1}{\rho}\frac{\partial\rho}{\partial T}\Big|_p \tag{4.3}$$

is the isobaric thermal expansion coefficient, which is simply equal to $1/T$ for perfect ideal gases, usually employed in thermoacoustic systems.

Fluids in thermodynamic conditions close to their critical point have large thermal expansion coefficients (see figure 4.1), and their use would, theoretically, greatly increase the thermoacoustic gain in Eq. (4.2). In particular, for fluids in transcritical, or pseudo-boiling (PB) conditions [13–15], wave-induced compressions and dilatations could be so large that periodic transitions from liquid-like fluid (pseudo liquid, PL) to gas-like fluid (or pseudo gas, PG) would occur (see figure 4.1a). Around the PB region, the highly nonlinear coupling between pressure, temperature, and density has been proposed [10] as the reason for some undesired effects, such as thermoacoustic instabilities in high-pressure combustion chambers [76,77] or bulk-mode oscillations in pressurized fuel heat exchangers [1,5,7,11,78], often leading to catastrophic hardware failure.

The use of a fluid close to its critical point in a thermoacoustic engine was already suggested by [29]. In fact, the power energy density is proportional to $\alpha_{p_0} T_0$, making a high thermal expansion coefficient one of the basic requirements in the selection of the working fluid. However, the high pressures involved in the handling of transcritical fluids, together with the drop of their thermal diffusivity (requiring very small pore size), has limited their use in a thermoacoustic engine so far [79]. Moreover, high-fidelity numerical simulations of transcritical thermoacoustic instabilities have not been carried out yet. One of the major reasons is the use of fully conservative schemes [36,37,50], for which spurious numerical oscillations have been shown to produce unstable computations when transcritical flows are considered [35, 38, 60]. The most relevant previous work is the development of the linear thermoacoustic theory, applicable to a generic fluid, by [29], which builds upon classic linear theory [24,80,81]. This theory was applied to the design of a thermoacoustic engine successfully operated with liquid sodium [69], which was not in a transcritical state. However, [69] demonstrated that fluids other than ideal gases, and in particular liquids, which had

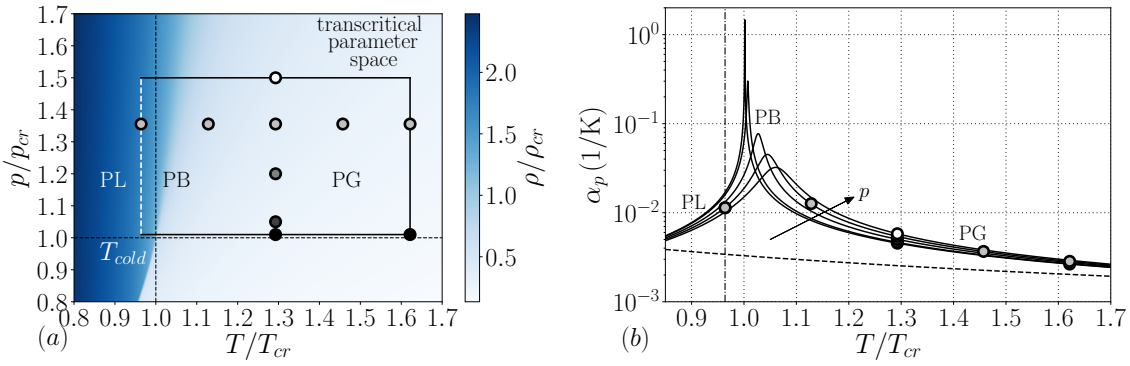

Figure 4.1. (a): state diagram for CO_2 showing flooded contours of reduced density ρ/ρ_{cr}, with vertical and horizontal black dashed lines indicating critical temperature and pressure, respectively; the rectangle drawn with solid black lines determines the parameter space of T_{hot} taken into account with the linear stability analysis, with $T_{cold} = 293.15$ K (see figure 4.2 and Eq.s (4.9) and (4.10)), fixed for all cases, indicated by a vertical white dashed line. The conditions for T_{hot} for the Navier-Stokes computations are indicated with circles, for a total of 10 configurations (see table 4.1). (b): isobaric thermal expansion coefficient (Eq. (4.3)) versus reduced temperature for CO_2, at the pressures indicated in table 4.1, modeled with the PR EoS (solid line) and as a perfect ideal gas (dashed line, $1/T$); a vertical black dashed-dotted line indicates $T_{cold} = 293.15$ K. PG, PB, and PL stand for fluid in pseudo-gaseous, pseudo-boiling, and pseudo-liquid conditions, respectively.

Table 4.1.
Selected base pressures for the Navier-Stokes simulations.

p_0 (MPa)	7.451	7.746	8.853	10.000	11.066
p_0/p_{cr}	1.01	1.05	1.2	1.356	1.5
symbol	●	●	○	○	

been employed before in Malone-type Stirling-like engines [82], can be employed in thermoacoustic systems.

The objective of this work is to establish a numerical benchmark for high-fidelity simulations of transcritical thermoacoustic flows, extending previous efforts aimed at the understanding and description of canonical thermoacoustic instabilities [12, 25, 26]. This goal is accomplished, building upon [28], with an idealized version of the setup used by [79]: a standing-wave-like thermoacoustically unstable two-dimensional resonator with transcritical CO_2 as the working fluid.

4.2 Problem Formulation

Table 4.2.
Critical temperature, pressure, and density of carbon dioxide.

fluid	T_{cr}	p_{cr}	ρ_{cr}
CO_2	304.1282 K	7.3773 MPa	467.6 kg/m^3

4.2.1 Selection of Thermodynamic States

In this work we have selected carbon dioxide (see table 4.2 for its critical parameters) as the working fluid. Its transcritical, or pseudo-boiling (PB), state is reached when the fluid is at pressures exceeding its critical value, $p > p_{cr}$, and the temperature varies between $T < T_{cr}$ (pseudo-liquid conditions, PL) and $T > T_{cr}$ (pseudo-gaseous conditions, PG), as figure 4.1 shows. The density rapidly drops when transitioning from PL to PG conditions (figure 4.1a), hence the spike in the isobaric thermal expansion coefficient (figure 4.1b). However, for increasing pressures, this transition becomes more gradual, and, for large values of the temperature, α_p tends towards $1/T$, the value corresponding to a perfect ideal gas.

The equation of state (EoS) of [18] and the model of [19] for viscosity and thermal conductivity are chosen as real-fluid model due to their simplicity and easiness of

implementation. Notice that the EoS and transport parameter model degrade in accuracy for thermodynamic conditions close to the critical point, while still retaining all the important features of real fluids.

Five base pressures (p_0) and five hot temperature T_{hot} (see figure 4.2 and Eq.s (4.9) and (4.10)) values are considered for the computational setup of the Navier-Stokes simulations, but only 10 combinations are solved for numerically (symbols in figure 4.1). For all cases, the value of the cold temperature is $T_{cold} = 293.15$ K.

4.2.2 Computational Setup

Governing Nonlinear Equations and Numerical Setup

In this work we consider the fully compressible Navier-Stokes equations, expressed by the conservation laws of mass and momentum,

$$\frac{\partial \rho}{\partial t} + \frac{\partial \rho u_j}{\partial x_j} = 0, \tag{4.4}$$

$$\frac{\partial \rho u_i}{\partial t} + \frac{\partial \rho u_i u_j}{\partial x_j} = -\frac{\partial p}{\partial x_i} + \frac{\partial \tau_{ij}}{\partial x_j}, \tag{4.5}$$

and the evolution equation for pressure [53],

$$\frac{\partial p}{\partial t} + \frac{\partial p u_j}{\partial x_j} = (p - \rho a^2)\frac{\partial u_j}{\partial x_j} + \frac{a^2 \alpha_p}{c_p}\left(\tau_{ij}\frac{\partial u_i}{\partial x_j} - \frac{\partial q_j}{\partial x_j}\right), \tag{4.6}$$

where t is time, x_j and u_j ($j = 1, 2, 3$) are the components of position and velocity, ρ and p are the density and pressure, a is the sound speed, α_p is the isobaric thermal expansion coefficient (Eq. (4.3)), and c_p is the isobaric specific thermal capacity. The Newtonian viscous stress tensor τ_{ij}, according to Stokes's hypothesis, and the Fourier heat flux read, respectively,

$$\tau_{ij} = \mu\left(\frac{\partial u_i}{\partial x_j} + \frac{\partial u_j}{\partial x_i} - \frac{2}{3}\delta_{ij}\frac{\partial u_k}{\partial x_k}\right), \qquad q_j = -k\frac{\partial T}{\partial x_j}, \tag{4.7}$$

where δ_{ij} is the Kronecker delta, μ is the dynamic viscosity, k is the thermal conductivity, T is the absolute temperature.

Eq.s (4.4), (4.5), and (4.6) are solved with the unstructured spectral difference (SD) solver SD3DVISP, the same used by [26] in their thermoacoustics simulations. The solver has been upgraded with real-fluid models and solves for the pressure evolution equation (Eq. (4.6)) instead of the total energy equation, as tested and validated in [38]. This numerical approach has been shown to be much more computationally stable than the fully conservative one, with the SD method, for the correct numerical solution of transcritical flows. However, the numerical method, being non conservative, entails a change in time of the integral value of the total energy, which is non physical. Nevertheless, this error is limited in magnitude by the smallness of the Mach numbers considered in our numerical simulations [35] and it is not significant for the conditions we have numerically simulated.

The Navier-Stokes numerical simulations are initialized with the following conditions:

$$p = p_0, \quad T_0(x), \quad u = \frac{p_0 p_{amp}}{\rho_0 a_0} \sin(\pi x/L), \quad v = 0, \tag{4.8}$$

where $T_0(x)$ is given by Eq.s (4.9) and (4.10), $\rho_0 = \rho_0(x)$ and $a_0 = a_0(x)$ are the density and sound speed corresponding to p_0 and $T_0(x)$, respectively, and p_{amp} is fixed at $p_{amp} = 10^{-7}$ for all cases, a part from the ones analyzed in §4.5.2, for which $p_{amp} = 5 \cdot 10^{-3}$. Eq. (4.8) imposes an initial disturbance in the computational setup that is thermoacoustically amplified if the system is fluid-dynamically unstable.

Geometry Optimization

The geometrical setup considered in this study (figure 4.2) is a two-dimensional duct composed by a hot cavity, indicated by the subscript *cav*, a thermoacoustic stack, indicated by the subscript *stk*, and a long resonator. The whole system is enclosed axially by two adiabatic walls at $x = 0$ and $x = L$, respectively. Fluid in

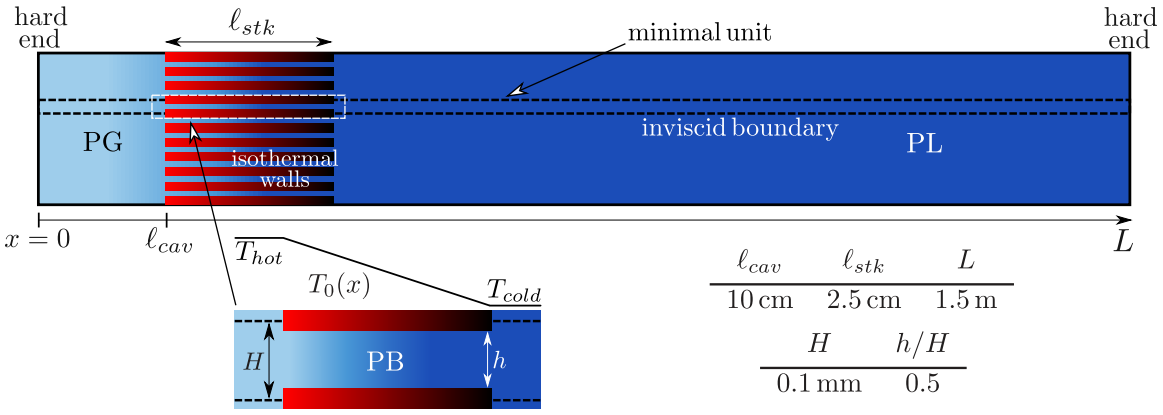

Figure 4.2. Computational setup (not to scale) with geometrical parameters for minimal unit numerical simulations. Isothermal boundary conditions in the stack are imposed following Eq. (4.10). The side walls are considered adiabatic. PG stands for pseudo-gaseous fluid, PB for pseudo-boiling fluid, and PL for pseudo-liquid fluid.

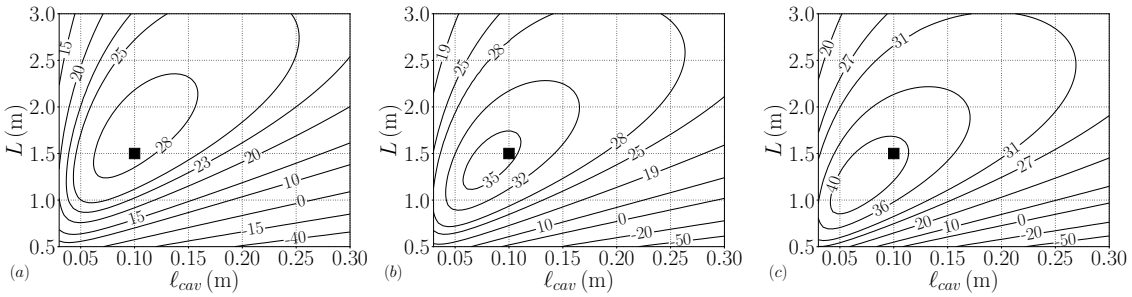

Figure 4.3. Isolevels of thermoacoustic growth rate, α [rad/s], versus total length, L, and length of the hot cavity, ℓ_{cav} (see figure 4.2), for $p_0 = 10$ MPa, $\Delta T = 100$ K (a), $\Delta T = 125$ K (b), and $\Delta T = 150$ K (c), with a black square indicating the selected design point. These results are obtained with the solution of the linear system of equations composed by Eq.s (2.38a) and (2.38b).

PL conditions (T_{cold}) and PG conditions (T_{hot}), according to the base temperature distribution

$$T_0(x) = \begin{cases} T_{hot} & 0 \le x \le \ell_{cav}, \\ T_{cold} & \ell_{cav} + \ell_{stk} \le x \le L, \end{cases} \tag{4.9}$$

bound the stack ($\ell_{cav} < x < \ell_{cav} + \ell_{stk}$), kept around pseudo-boiling (PB) conditions by isothermal wall boundary conditions, which impose the following temperature profile:

$$T_0(x) = T_{hot} - \Delta T(x - \ell_{cav})/\ell_{stk}, \tag{4.10}$$

where $\Delta T = T_{hot} - T_{cold}$. When the linearized equations are solved for, the flow field is considered at uniform base pressure p_0.

A canonical minimal unit [26] is carved out of this geometry, defining the computational setup used in the numerical simulations (both for the linearized equations and the fully nonlinear ones). The definition of a minimal unit greatly reduces the computational cost for the Navier-Stokes simulations (which is especially high for simulations featuring transcritical fluids) and does not hide any of the physics in the linear regime of the thermoacoustic instability. The nonlinear effects captured by this setup include thermodynamic ones and losses due to recirculation at the area changes, which will be analyzed in §4.5. Acoustic streaming, transitional turbulence, and nonlinear wave steepening are not considered in this study.

This minimal-unit computational setup is optimized, based on the aforementioned linear theory, for three consecutive values of ΔT (figure 4.3), resulting in the geometrical parameters listed in the table of figure 4.2. The optimization is performed here visually on the plots of the growth rates and provides a geometry for which thermoacoustic instability appears for only about $\Delta T = 25$ K. Other values of p_0 or ΔT considered in the optimization would lead to different geometries, which are not considered in this study.

4.2.3 Grid Sensitivity Analysis

The Navier-Stokes simulations are carried out on an unstructured mesh including only half of the thermoacoustic pore (figure 4.4), due to the symmetry of the flow field with respect to the centerline of the domain, which allows for faster computations. Two different grids are considered (see table 4.3): A (coarse) and B (fine). The order

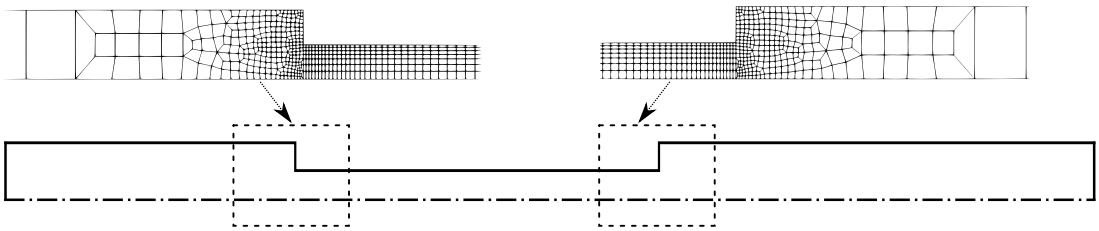

Figure 4.4. Zoom of unstructured mesh for Grid B (see table 4.3), close to area changes, used for the Navier-Stokes simulations. The mesh has number of elements $N_{\text{el}} = 2635$.

Table 4.3.
Number of degrees of freedom, $N_{\text{dof}} = N^2 N_{\text{el}}$, for the two grids considered in this study, and for two numbers of solution points N inside each element.

	Grid A ($N_{\text{el}} = 1135$)	Grid B ($N_{\text{el}} = 2635$)
	N_{dof}	N_{dof}
$N = 2$	4540	10540
$N = 3$	10215	23715

of accuracy of the polynomial reconstruction is fixed with N, indicating the number of points inside each element. For each grid, $N = 2$ and $N = 3$ are chosen.

We here perform a grid sensitivity study on the linear growth rate entailed by the transcritical thermoacoustic instability. In [26], growth rates for their Navier-Stokes minimal-unit computations were matching with considerable accuracy the results from the linear theory, while in the simulations by [25], executed with a low-order finite-volume solver and which were accounting for the complete thermoacoustic geometry, a mismatch between those was found. In both of these previous works a perfect ideal gas was employed.

In this work we observe that, even when the fluid inside the stack is transcritical, the growth rates predicted by linear theory match with excellent agreement the

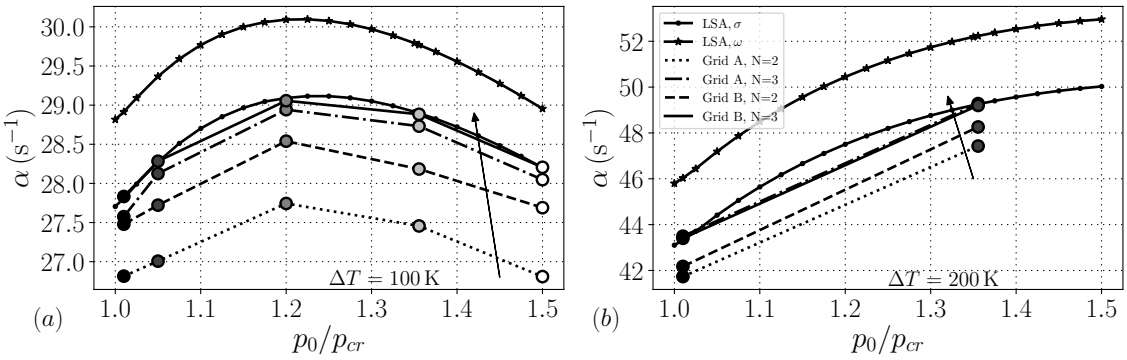

Figure 4.5. Growth rate versus reduced base pressure for $\Delta T = 100$ K (a) and $\Delta T = 200$ K (b), for the different grid resolutions in table 4.3. Symbols connected by lines are obtained from the Navier-Stokes simulations, with arrows indicating increasing resolution (see legend in (b)). The upper curves are results from linear stability analysis (LSA): thermoviscous functions only dependent on ω (Eq. (4.12)), thermoviscous functions dependent on $\alpha + i\omega$ (Eq. (4.11)).

growths extracted from the minimal-unit Navier-Stokes simulations at the finest resolution (grid B and $N = 3$ in table 4.3), while coarser resolutions show a successive improvement and converging behavior (figure 4.5). However, an important remark is that the thermoviscous functions in Eq.s (2.26) and (2.36) have to depend on the eigenvalue σ, and not only on its imaginary part ω, otherwise the linear theory overpredicts the growth rate. In fact, in the coordinate transformation of Eq. (2.21), the variable

$$\eta = \sqrt{\frac{\sigma}{\nu_0}} r = \sqrt{2i + 2\frac{\alpha}{\omega}} \frac{r}{\delta_\nu}, \tag{4.11}$$

where δ_ν is defined in Eq. (4.31) and r is the transverse spatial coordinate, includes also the growth rate α, and is a generalization of the case $\alpha \ll \omega$ ($\sigma \approx i\omega$, used in [24–27]), for which

$$\eta = \sqrt{\frac{i\omega}{\nu_0}} r = \sqrt{2i} \frac{r}{\delta_\nu} = (i+1) \frac{r}{\delta_\nu}. \tag{4.12}$$

For both grids, the resolution $N = 3$ exhibits approximately the same values of growth rates (especially for $\Delta T = 200$ K, for which the two results are almost

identical). Furthermore, an almost equal number of degrees of freedom N_{dof} entails different results depending on the order of the polynomial reconstruction inside each element: grid A (coarser) with $N = 3$ provides a better estimate of the growth rates than grid B (finer) with $N = 2$. This justifies the use of high-order numerics in the simulation of thermoacoustic instabilities.

Hereinafter only results from grid B with $N = 2$ or $N = 3$ (finest resolution) will be considered. Frequencies were found to be not very sensitive to grid resolution.

4.3 Real-fluid Effects on Frequencies, Growths, and Eigenmodes

We start our discussion of the numerical results with the real-fluid effects on the frequency and growth of oscillations of the fluid in the minimal-unit setup, together with a closer look at the eigenmodes of the system.

4.3.1 Real-fluid Effects on Frequency

The frequency of oscillation of the system, f, can widely change depending on the conditions under investigation. Keeping the same ΔT across the stack, for increasing base pressures, the frequency increases approximately with a linear trend (figure 4.6b), entailing changes of 15 % from $p/p_{cr} = 1.01$ to 1.5.

On the other hand, a nonlinear, non-monotonic, and larger effect on frequency is entailed by the ΔT across the stack (see figure 4.6a) with a given base pressure p_0. The largest values of f are obtained for values of ΔT below 5 K, for which most of the system is filled with pseudo-liquid (which has a high speed of sound). Then, for increasing ΔT, the frequency changes at maximum of about 40 %, with a decreasing trend, the sharper the closer the base pressure is to the critical pressure, due to the rapid changes in thermodynamic properties which characterize the transcritical region. For higher values of ΔT, the frequency begins to increase almost linearly, due to the increasing presence of fluid in near-ideal gas state (for which the speed of sound

increases with temperature). Thermoacoustic oscillations featuring ideal gases show much milder changes and dependance on the thermodynamic conditions [25, 26].

The data extracted from the Navier-Stokes simulations confirm with excellent agreement the results obtained from the linear theory. The grid required to capture the correct frequency of operation of the system is less stringent than the one needed for numerical convergence of the growth rates (figure 4.5), which are the topic of the next section.

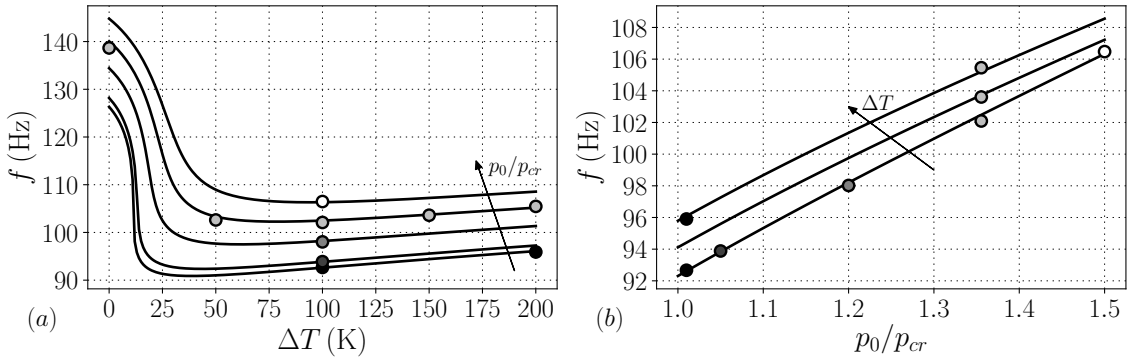

Figure 4.6. Frequency versus ΔT for the five base pressures in table 4.1 (a), and frequency versus reduced base pressure p_0/p_{cr} for $\Delta T = 100, 150, 200$ K (b). Solid lines indicate results from linear theory, symbols are data extracted from the Navier-Stokes simulations (with grid B and resolution $N = 2$, see table 4.3).

4.3.2 Real-fluid Effects on Growth Rates

The thermoacoustic growth rate strongly depends on the ΔT across the stack (see figure 4.7a), because ΔT is the parameter that controls the thermoacoustic gain Θ, which in turn controls the acoustic energy production (which we will discuss more in detail in section §4.4.1). For all base pressures considered, the minimum ΔT for the onset of instability (positive growth rate) is only approximately 25 K, much less than what usually needed in standard thermoacoustic systems employing perfect ideal

gases [25, 26, 83]. In reality, as the zoom in figure 4.7a shows, configurations where the base pressure is closer to the critical pressure need the lowest ΔT (= 23 K) to be thermoacoustically unstable.

A small dip is present right before ΔT = 15 K only for base pressures closer to the critical pressure ($p_0 = 1.01p_{cr}$ and $p_0 = 1.05p_{cr}$). For those pressures, the trend of the growth rate becomes non-monotonic as soon as transcritical conditions appear inside the stack, whereas the milder pseudo-boiling states of the higher base pressures do not entail this effect. From the onset of instability onwards, increasing ΔT always increases the growth rates, with a trend similar among all base pressures. However, for $p_0 = 1.01p_{cr}$ and $p_0 = 1.05p_{cr}$, the growth rate rapidly increases above all other cases, but then begins to decrease in magnitude, with respect to them, for ΔT higher than about 100 K, eventually being the lowest at the maximum $\Delta T = 200$ K considered. Instead, for the other three base pressures, the highest considered in this study, the trend of the growth rate with ΔT is monotone, closer to ideal-gas behavior, and much smoother than the one shown by the lowest p_0.

The dependence of the growth rate on the base pressure (figure 4.7b) is not as strong as the one observed above against ΔT, and is more pronounced for higher values of ΔT (see also figure 4.5). However, the growth rate shows a decreasing trend as the base pressure approaches the critical pressure, which is a somewhat unexpected result. This is because higher base density gradients are expected to boost thermoacoustic energy production [28] and therefore the growth rate, hence setting the expectation for a monotonic decrease of the growth rate with p_0/p_{cr}. The results from the linear theory and Navier-Stokes simulations instead show that other factors come into play, which will be shown and explained in more detail in §4.4.1. Furthermore, for $\Delta T = 100$ K, the growth rate changes in a non-monotonic manner with different base pressures, showing a maximum around $p_0 = 1.25p_{cr}$ (see also figure 4.5a). The same behavior is expected to be shown by the other values of ΔT considered, which would have maxima of growth rates for higher values of p_0/p_{cr}. All

of these effects are usually not present with thermoacoustic systems employing ideal gases [25, 26, 83].

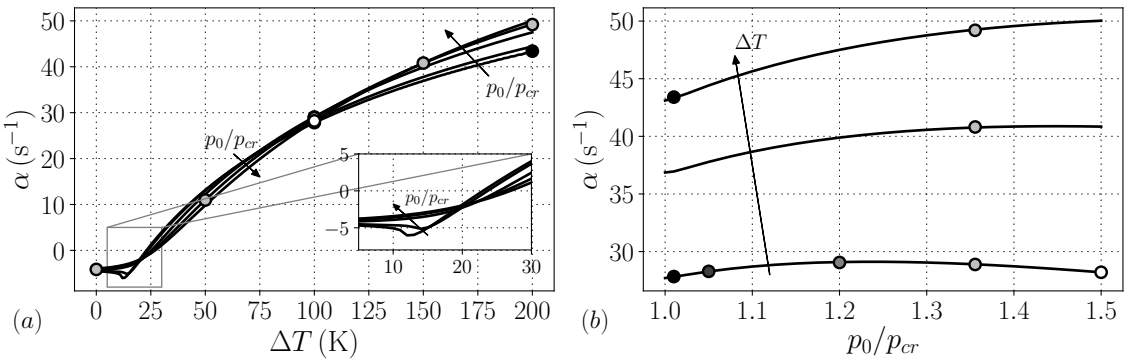

Figure 4.7. (a): Growth rate versus ΔT for the five base pressures in table 4.1; (b): growth rate versus reduced base pressure p_0/p_{cr} for $\Delta T = 100, 150, 200$ K. Solid lines indicate results from linear theory, symbols are data extracted from the Navier-Stokes simulations.

Overall, all frequencies and growth rates extracted from the Navier-Stokes simulations agree well with their respective predictions from the linear theory. This confirms the validity of the linear stability ansatz despite the large gradients in the base state. When higher values of pressure oscillations are considered, as we will see in §4.5.2, thermodynamic nonlinearities, which can potentially decrease the values of the linear growth rates, arise around the pseudo-boiling region. As an additional step in verifying the linear theory with the data from the Navier-Stokes simulations, and to discuss more real-fluid effects, we now take a look at the system's eigenmodes.

4.3.3 Real-fluid Effects on Eigenmodes

The system exhibits oscillations in all fluid and thermodynamic variables. Pressure and mass flow rate amplitudes, and their relative phasing, in particular, are the quantities of primary interest and are analyzed in figure 4.8. The results from the linear stability theory match well the data extracted from the unstructured Navier-

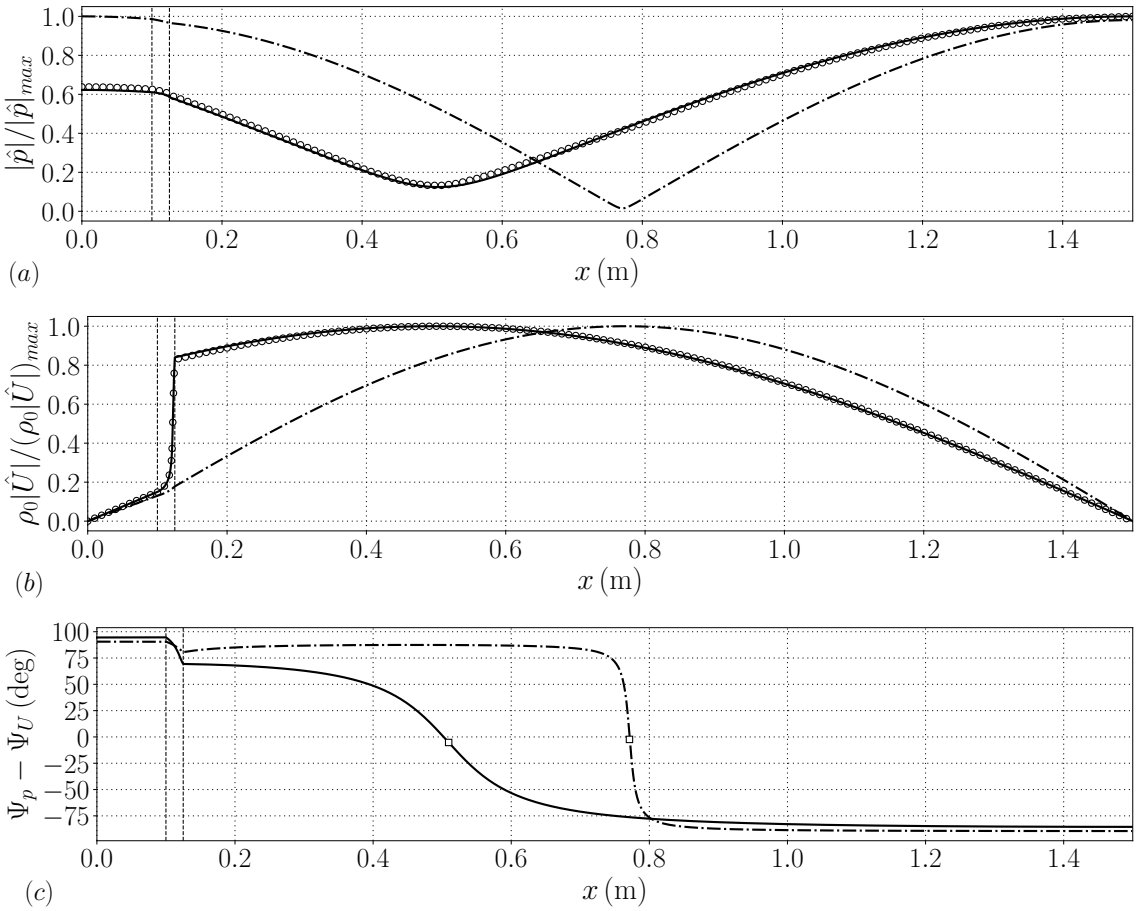

Figure 4.8. Axial distribution of pressure (a), mass flow rate (b) dimensionless amplitudes, and phasing between $\hat{p}$ and $\hat{U}$ (c), for $\Delta T = 200\,\mathrm{K}$ and $p_0 = 10\,\mathrm{MPa}$: linear theory (solid lines), data extracted from the Navier-Stokes simulations (circles). Dashed-dotted lines indicate eigenmodes obtained from the linear theory with the assumption of thermally perfect ideal gas, still with Chung's model for transport properties. Vertical dashed lines indicate locations of abrupt area change. The squares in (c) indicate values of phase difference at the location of minimum pressure amplitude.

Stokes simulations. Not a significant change in the overall mode spatial distribution, nor in the matching with Navier-Stokes simulations, is found for $\Delta T = 200$ K for different base pressures.

The linearized mass flow rate eigenmode (figure 4.8b) presents two nodes at the beginning and end of the duct, where the pressure has its antinodes (figure 4.8a), due to the imposed hard-wall boundary conditions, and a maximum inside the resonator, where the pressure is minimum. The oscillating mass on the left hand side of the stack and in the hot cavity, where pseudo-gaseous (PG) fluid exists, exhibits a trend similar to the ideal gas configuration. On the other hand, the sharp base density gradients in the stack entails an equally sharp boost in oscillating mass on the right hand side of the stack, where pseudo-boiling (PB) fluid exists. In the resonator, instead, where pseudo-liquid fluid (PL) is present, the mass flow rate oscillation is overall the highest. Moreover, while the ideal gas case shows a mass flow rate eigenmode very similar to the first harmonic of a standing-wave resonance in the duct, for the real gas case the eigenmode is significantly more modified, due to the transcritical conditions present in the stack.

Another quantity of interest is the phasing between $\hat{p}$ and $\hat{U}$, i.e. $\Psi_p - \Psi_U$ (figure 4.8c). This quantity, for the ideal gas configuration, is consistent with similar trends reported in [84], where a sharp change from $\pi/2$ to approximately $-\pi/2$ was observed. Instead, for the transcritical case, this phasing difference shows a much milder transition inside the resonator. Moreover, the value of $\Psi_p - \Psi_U$ at the point of minimum $|\hat{p}|$ (indicated by squares in figure 4.8c) is not exactly zero, and it is in magnitude higher for the transcritical fluid with respect to the the ideal gas case. The point where $|\hat{p}|$ is minimum is the average node location, indicated with a subscript n in the following discussion. It can be shown that (appendix 4.3.3)

$$\Psi_{p_n} - \Psi_{U_n} = -\arctan\left(\frac{\alpha}{\omega}\right). \tag{4.13}$$

indicating that the pressure-velocity phase difference is significantly different than zero at the average node location for transcritical flows, being α/ω high. This means that, at $x = x_n$, pressure and flow rate are generally more out of phase for transcritical fluids than for ideal gases.

We call $x = x_n$ an average node location because, there, the (minimum) pressure amplitude is not null, hence x_n is not a stationary pressure node. Instead, for the

analogous ideal gas configuration, $|\hat{p}|_{min}$ seems to be 0. However, a more in depth analysis of this (figure 4.9b) reveals that, for the ideal gas case, $|\hat{p}|_{min}/\hat{p}|_{max}$ is not exactly zero, but is at maximum 2% for all the values of ΔT considered, which can not be appreciated from figure 4.8a only. On the other hand, for the real fluid, the pressure amplitude minimum can be a considerable portion (at maximum 12%) of its maximum value, therefore its pressure eigenmode tends to be more flat overall than for ideal gases. As a result of the closure of the acoustic energy budgets, it can be shown that (appendix 4.3.3, see figure figure 4.9c), regardless of the EoS,

$$\frac{|\hat{p}|_{min}}{|\hat{p}|_{max}} \propto \frac{|\alpha|}{\omega}. \tag{4.14}$$

The average node location inside the duct (figure 4.9a) is approximately at the center of the domain for $\Delta T = 0$ K, as per standing wave resonance. For increasing ΔT, x_n shifts rightwards for the ideal gas case, remaining around $0.51L$ at maximum. On the other hand, for a real fluid, x_n shifts at first leftwards, reaching a minimum of about 31% of the total length, but eventually also rightwards, for increasing ΔT, being overall always in the left hand side of the duct. This trend resembles the one of frequency versus ΔT (figure 4.6a) because, during the thermoacoustically sustained oscillation, the wavelength decreases while traversing the fluid's base state in the hot cavity, due to its lower speed of sound if compared to the one of the heavier PL in the resonator. Therefore, the pressure node shifts towards the left of the duct, until the speed of sound of the PG in the hot cavity increases when ΔT grows.

A final regard on real-fluid effects can be appreciated with the peculiar features exhibited by the pressure eigenmode towards the end of the stack, which are magnified in figure 4.10 for $\Delta T = 200\,\text{K}$ and $p_0 = 1.01 p_{cr}$. In fact, the abrupt change in duct area from stack to resonator entails a change in derivative of the pressure eigenmode. This is because the acoustic impedance Z_0, obtained as the ratio of the specific acoustic impedance and the duct area,

$$Z_0 = \frac{\rho_0 a_0}{A}, \tag{4.15}$$

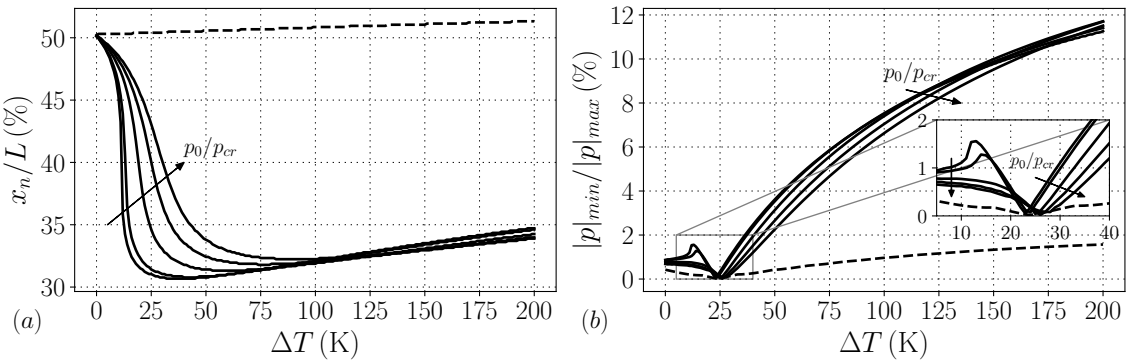

Figure 4.9. Data from linear stability theory on pressure mode amplitude: location (a) and relative magnitude (b) of its minimum. Solid lines are for real-fluid EoS (for all base pressures in table 4.1), and the dashed line indicates thermally perfect ideal gas EoS, still with Chung's model for transport properties (for $p_0 = 10$ MPa only).

jumps from one duct to the other. From stack to resonator, no discontinuity in base state quantities exists, hence the jump in Z_0 is only due to area change present at $(x - \ell_{cav})/\ell_{stk} = 1$.

Inside the stack, instead, the duct area is uniform, but great variations of base density and speed of sound exist, especially in the vicinity of the pseudo-boiling region, resulting in rapidly changing specific acoustic impedance around $(x - \ell_{cav})/\ell_{stk} = 0.942$. Therefore, the acoustic impedance Z_0 presents a pseudo-jump which, entailing a great variation of its derivative, changes gradually the spatial derivative of the pressure eigenmode (and of the mass flow rate, not shown). This rapid change in Z_0 at transcritical conditions effectively acts on the eigenmodes like a continuous change in geometry. When milder conditions in the stack are present (higher base pressures), the spike of thermodynamic quantitites is not as pronounced as seen above, and the eigenmodes look smoother, like their ideal gas counterparts.

The large difference in acoustic impedance between resonator and hot cavity is also responsible for the presence of the maximum of pressure on the right end side of the domain, when the real gas configuration is concerned (see figure 4.8a). For ideal

gases, the acoustic impedance in the hot cavity might be higher than in the resonator, instead, causing the maximum pressure amplitude to be at $x = 0$.

Having finished with the real-fluid effects on frequencies, growths, and eigenmodes, we now shift our discussion on the energetic aspect of the transcritical thermoacoustic instability, by considering the acoustic and total energy budgets.

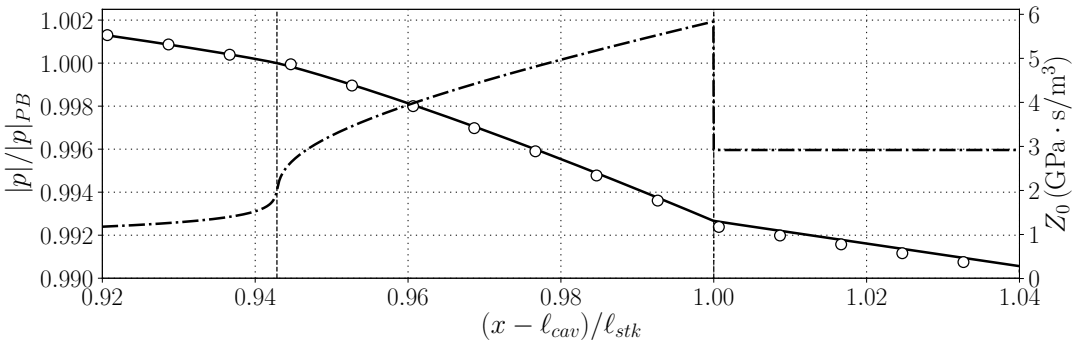

Figure 4.10. Axial distribution of dimensionless pressure amplitudes (left y axis), and base acoustic impedance (right y axis), for $\Delta T = 200\,\mathrm{K}$ and $p_0 = 1.01 p_{cr}$: linear theory (solid line), data extracted from the Navier-Stokes simulations (circles), and base acoustic impedance (dashed dotted line). The vertical dashed line on the left indicates pseudo-boiling (PB) conditions, while the one on the right denotes the separation between stack and resonator.

Discussion on Minimum Pressure Amplitude

Expressing $\hat{p}$ and $\hat{U}$ in the conventional complex phasor notation, $\hat{p} = |\hat{p}|e^{i\Psi_p}$ and $\hat{U} = |\hat{U}|e^{i\Psi_U}$ in Eq. (2.38a) yields

$$\hat{U} = -\frac{A}{\sigma\rho_0 F_\nu} e^{i\Psi_p}\left(\frac{d|\hat{p}|}{dx} + i|\hat{p}|\frac{d\Psi_p}{dx}\right), \tag{4.16}$$

hence

$$|\hat{U}| = \frac{A}{|\sigma|\rho_0|F_\nu|}\sqrt{\left(\frac{d|\hat{p}|}{dx}\right)^2 + \left(|\hat{p}|\left|\frac{d\Psi_p}{dx}\right|\right)^2}, \tag{4.17}$$

$$e^{i(\Psi_U - \Psi_p)} = -\frac{|\sigma||F_\nu|}{\sigma F_\nu}\left(\frac{d|\hat{p}|}{dx} + i|\hat{p}|\frac{d\Psi_p}{dx}\right)\Big/\sqrt{\left(\frac{d|\hat{p}|}{dx}\right)^2 + \left(|\hat{p}|\left|\frac{d\Psi_p}{dx}\right|\right)^2}, \tag{4.18}$$

and, from Eq. (2.38b),

$$\sigma|\hat{p}|e^{i(\Psi_p-\Psi_u)}\frac{AF_k}{\rho_0 a_0^2}=|\hat{U}|\left(\Theta\Phi_{\mathcal{P}}-i\frac{d\Psi_U}{dx}\right)-\frac{d|\hat{U}|}{dx}. \tag{4.19}$$

In the resonator (on the right of the stack) the base state is uniform, hence $\Theta=0$, and inviscid walls are assumed ($F_\nu=F_k=1$). There, where the average pressure node (n) is, if α is not too close to 0, $|\hat{p}|_n$ is the minimum value of $\hat{p}$ and $|\hat{U}|_n$ can be assumed as the maximum of $\hat{U}$. Therefore, $d|\hat{p}|/dx|_n=d|\hat{U}|/dx|_n=0$ in Eq.s (4.17), (4.18), and (4.19) yields

$$|\hat{U}|_n=\frac{A}{|\sigma|\rho_0}|\hat{p}|_n\left|\frac{d\Psi_p}{dx}\right|_n, \tag{4.20}$$

$$e^{i(\Psi_{pn}-\Psi_{U_n})}=i\frac{\sigma}{|\sigma|}\mathrm{sgn}(\frac{d\Psi_p}{dx}|_n)\quad\rightarrow\quad\Psi_{p_n}-\Psi_{U_n}=-\arctan\left(\frac{\alpha}{\omega}\right), \tag{4.21}$$

$$\frac{|\sigma|^2}{a_0^2}=\left|\frac{d\Psi_p}{dx}\right|_n\left|\frac{d\Psi_U}{dx}\right|_n. \tag{4.22}$$

Eq. (4.20) shows that, in order to have maximum $|\hat{U}|_n$, $|d\Psi_p/dx|_n$ is maximum. Eq.s (4.20), (4.21), and (4.22) have been verified with the data obtained from the linear theory (not shown).

In section §4.3.3 it was observed that $|\hat{p}|_{min}/|\hat{p}|_{max}$ (figure 4.9b) is proportional to $|\alpha|/\omega$ (figure 4.11b). This can be explained by noticing that, in the resonator, Eq. (2.42) becomes

$$\frac{d\overline{\dot{W}}}{dx}=-\alpha\overline{\mathcal{E}}, \tag{4.23}$$

and by assuming an acoustic energy distribution (Eq. (2.43)) equal to its value at $x=L$ ($|\hat{U}|_{x=L}=0$). After integrating Eq. (4.23) from the right end side of the stack to the right end side of the resonator, the power at the average node location is

$$\overline{\dot{W}}_n=|\hat{p}|_n|\hat{U}|_n(-\frac{\omega}{|\sigma|})\mathrm{sgn}(\frac{d\Psi_p}{dx}|_n)=\frac{\alpha A}{2\rho_0 a_0^2}|\hat{p}|^2_{max}(L-x_n), \tag{4.24}$$

where x_n is its location. This is consistent with the intuitive reasoning that, if there is growth, nowhere in the resonator the acoustic power flow can be blocked by a stationary node, which would instead happen for a perfectly standing wave (zero acoustic power) with $\alpha=0$. Inserting Eq. (4.20) in Eq. (4.24) yields

$$\left(\frac{|\hat{p}|_n}{|\hat{p}|_{max}}\right)^2=-\frac{|\sigma|^2\alpha}{2a_0^2\omega}(L-x_n)/\left|\frac{d\Psi_p}{dx}\right|_n, \tag{4.25}$$

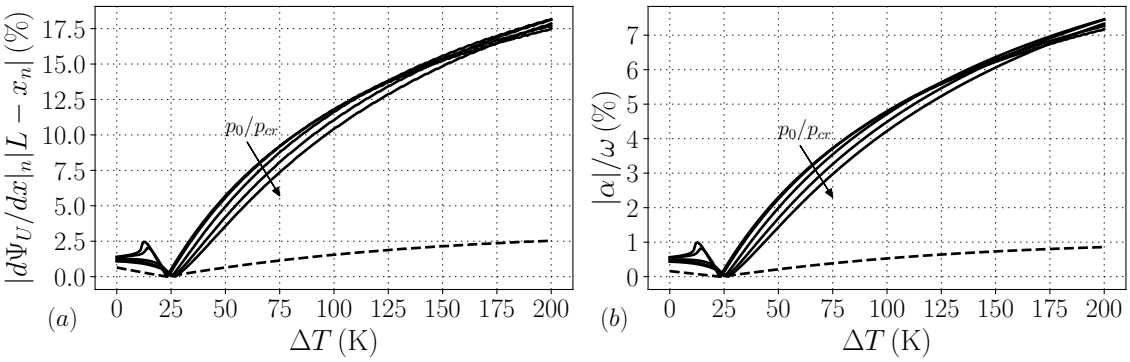

Figure 4.11. Data from linear stability theory: (a) product of the absolute value of the phase derivative at average node location of flow rate and absolute value of distance of average node location from the right end side of the duct (in the right hand side of Eq. (4.26)); (b) ratio of the absolute value of growth rate to pulsation $2\pi f$. Solid lines are for real-fluid EoS (for all base pressures in table 4.1, and the dashed line indicate ideal gas EoS (for $p_0 = 10$ MPa only).

which proves that, since the left hand side is always positive, $\alpha/\frac{d\Psi_p}{dx}|_n \leq 0$. Using Eq. (4.22) in Eq. (4.25), after taking the absolute value of its right hand side, yields

$$\left(\frac{|\hat{p}|_n}{|\hat{p}|_{max}}\right)^2 = \frac{1}{2}\frac{|\alpha|}{\omega}\left|\frac{d\Psi_U}{dx}\right|_n |L - x_n|. \tag{4.26}$$

With the data obtainable from the linear theory, it is found that $|d\Psi_U/dx|_n|L - x_n|$ (figure 4.11a) is proportional to $|\alpha|/\omega$ (figure 4.11b), hence also

$$\frac{|\hat{p}|_{min}}{|\hat{p}|_{max}} \propto \frac{|\alpha|}{\omega}, \tag{4.27}$$

explaining the trend observed in figure 4.9b.

Effect of stack's base temperature profile

The different mean temperature profiles in figure 4.12a are considered in order to investigate the effect of T_0 in the stack on the thermoacoustic growth rates. Those are computed according to

$$T_0 = T_{hot} - \Delta T \left(\frac{(x - \ell_{cav})}{\ell_{stack}} \right)^n , \tag{4.28}$$

where $n = 1$ indicates a linear profile. Values of n higher than 1 shift the highest temperature gradients towards the right end side of the stack, and the opposite happens for $n < 1$.

As it can be expected, for the same mean pressure, a different temperature distribution will entail a different mean density profile (not shown), therefore changing the location of PB fluid in the stack. For $n \ll 1$, the stack is almost full of pseudo-liquid, whereas for $n \gg 1$ the stack if filled with pseudo-gas for the most part. In the range of n considered in this study, the growth rate varies from a maximum of 36.36 1/s for the lowest n considered ($n = 1/7$), to a minimum of 27.02 1/s, achieved around $n = 1/2$, which is approximately a 35 % change. For values of n lower than 1/7, the growth rate continues to sharply increase due to the continuous raise in temperature gradients close to the left hand of the stack. The same continuous growth rate increase happens for n higher than 5, but less accentuated than the case of $n \ll 1$.

The different temperature profiles in figure 4.12a do not significantly change the operating frequency of the system, which varies of at maximum 1 % for the range of n considered. This is expected since in the discussion above T_{hot} and T_{cold} are fixed and so are the speed of sound inside resonator and hot cavity, which greatly influence the value of operating frequency (see discussion in §4.3.1).

4.4 Energy Budgets

The fundamental mechanisms of conversion from thermal to acoustic energy happen inside the stack, where a fluid parcel experiences a thermodynamic cycle, driven

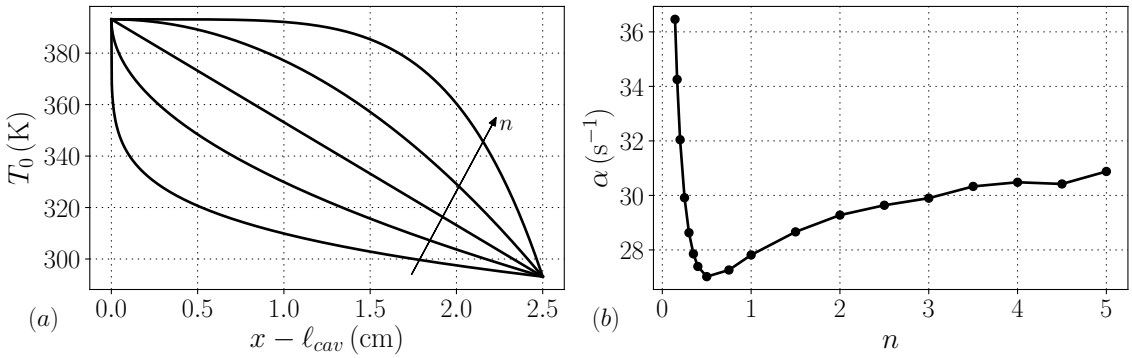

Figure 4.12. Profiles of mean temperature T_0 in the stack, considering $p/p_{cr} = 1.01$ and $\Delta T = 100$ K, for $n = 1/5, 1/2, 1, 2, 5$ (a, see Eq. (4.28)) and growth rates computed from linear theory versus n (b). The solid line in (b) is just a guide to the eye.

by the harmonic pressure oscillations, in which expansions and contractions are accompanied by heating and cooling. The resulting Lagrangian pressure-volume cycle, traversed clockwise, indicates mechanical power production (figure 4.13). How much power is produced is strongly dependent on the fluid's base state properties, which are a consequence of the imposed mean temperature distribution (Eq. (4.9)). For base pressures closer to the critical pressure, the transcritical conditions entail a sharper base density distribution, therefore entailing larger volume fluctuations for the same value of maximum pressure oscillations. Therefore, conditions closer to the critical point entail higher power production, due to the larger area encompassed by the Lagrangian cycle.

4.4.1 Acoustic Energy Budgets

Once the eigenvalue problem in Eq. (2.38) is solved, it is possible to directly evaluate all the variables in Eq.s (2.44), (2.45), and (2.46), allowing to compute the growth rate from Eq. (2.49). This procedure has been carried out for all the configurations considered in this work and the growth rate hence obtained has resulted

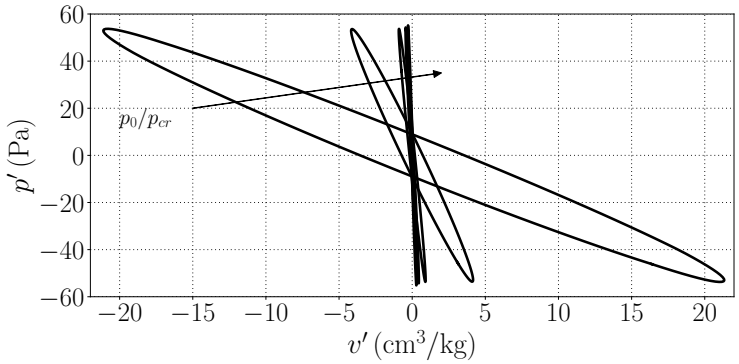

Figure 4.13. Fluctuating pressure plotted against specific volume fluctuation of a Lagrangian fluid parcel, for all base pressures of table 4.1, extracted with the aid of the linear theory. Initial position of the Lagrangian parcel is at the centerline of the stack and at pseudo-boiling conditions ($x = 12.21, 12.17, 12.019, 11.88, 11.77$ cm for increasing values of p_0). All oscillations are assumed to be at fixed maximum pressure amplitude, and with zero growth rate. All cycles are traversed clockwise.

to be in excellent agreement with the one from the direct numerical solution of Eq. (2.38). Indeed, the pointwise acoustic energy budgets (Eq. (2.42)) are closed (figure 4.14e), corroborating the validity of the data extracted from the linear theory.

The acoustic energy production (figure 4.14c) spikes at pseudoboling conditions, due to the peak in Θ (figure 4.14b). Depending on the base pressure, these peaks appear at different axial locations inside the stack. In fact, the location of pseudo-boiling conditions strongly depends on the base pressure: keeping the same ΔT and T_{cold}, for a pressure closer to the critical point, transcritical conditions are achieved for a lower temperature (see figure 4.1b), resulting in PB fluid closer to the cold right end side of the stack. Furthermore, the highest absolute values of Θ are attained for the values of p_0 closest to p_{cr}. This boost of production is, however, also accompanied by a similar increase in acoustic dissipation (figure 4.14c), due to the high values of Prandtl number typical of transcritical conditions (figure 4.14a). In fact, the Prandtl number shows trends which directly resemble the ones of the thermal expansion coefficient, which is the main driver of the variable Θ. Therefore, inside the stack, for $p_0 =$

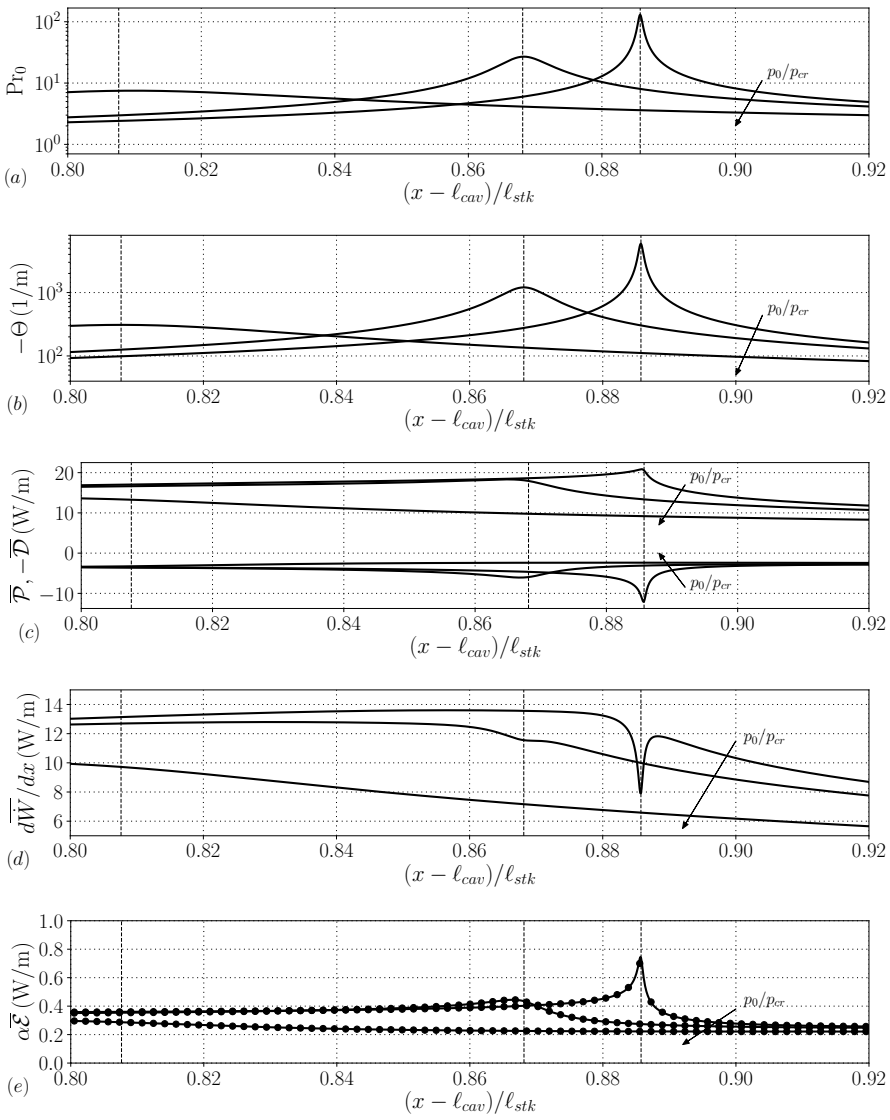

Figure 4.14. Base state quantities and acoustic energy budgets terms from linear theory, for $\Delta T = 100$ K and $p_0/p_{cr} = 1.01, 1.05, 1.2$ (see table 4.1), inside the stack and close to the respective PB regions. (a): base Prandtl number; (b): minus thermoacoustic gain (Eq. (4.1)); (c): acoustic energy production (Eq. (2.45), positive values), and minus acoustic energy dissipation (Eq. (2.46), negative values); (d): axial gradient of acoustic power (Eq. (2.44)); (e): $\overline{\mathcal{P}} - \overline{\mathcal{D}} - d\overline{\dot{W}}/dx$ (circles), and $\alpha\overline{\mathcal{E}}$ (solid lines, Eq. (2.43)), see Eq. (2.42). All quantities correspond to maximum pressure oscillation amplitude of 100 kPa, fixed for all base pressures. Vertical dashed lines indicate, for each base pressure, locations of minimum Θ, which are $x = 12.21, 12.17, 12.019$ cm for increasing values of p_0.

$1.01p_{cr}$, the sum of production and dissipation of acoustic energy can actually reach a minimum (figure 4.14c). This instead does not appear for higher values of p_0, which also features a lower spike of Θ, causing the non-monotone behavior observed for the growth rate as a function of p_0/p_{cr} in figure 4.5a. The trends of acoustic energy production and dissipation directly affect the ones of gradient of acoustic power and acoustic energy density, which show, when strong transcritical conditions exist, a dip (figure 4.14d) and a spike (4.14e), respectively. The rapid change in derivative of the acoustic power at PB conditions is akin to the one observed before for the pressure eigenmode (§4.3.3).

For all values of p_0, the acoustic power flows towards the left in the hot cavity, and towards the right in the resonator, reaching boundary values of zero due the imposed hard wall boundary conditions (figure 4.15a), while inside the stack (figure 4.15b) a positive gradient (also see figure 4.14d) confirms acoustic power production. The trends of the acoustic power inside the duct confirm the intuitive conclusion, drawn from figure 4.13, that near-critical base pressures entail higher power production. This will also be seen when limit cycle oscillations are present (figure 4.16). However, the heat required for sustaining the pressure oscillations at values of p_0 closer to p_{cr} is also expected to be higher, given the spike of thermal capacities typical of transcritical conditions. With to objective to assert the validity of this intuition, in the next section we analyze the total energy budgets.

4.4.2 Total Energy Budgets

The profile of $\overline{\dot{\mathcal{H}}}$ inside the stack (figure 4.15b) shows the cumulative time-averaged heat required from the solid walls of the stack to sustain the steady-state fluid oscillations inside it. The axial derivative of $\overline{\dot{\mathcal{H}}}$ represents the pointwise heat injected into the fluid. The highest heat is required to sustain carbon dioxide oscillating around its pseudo-boiling (PB) state, followed by fluid in pseudo-liquid and pseudo-gaseous conditions, on the right and left, respectively, of fluid in PB conditions. This hier-

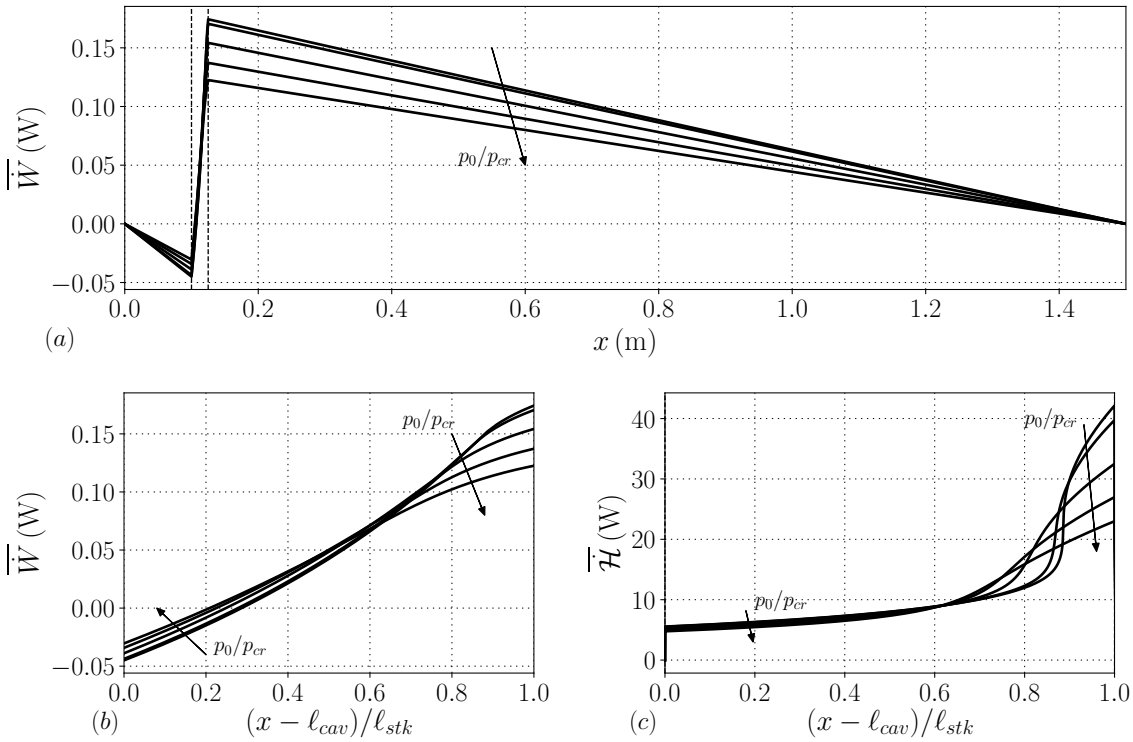

Figure 4.15. (a): acoustic power (Eq. (2.44)) in the whole domain; (b): acoustic power in the stack; (c): total energy flux (Eq. (2.63)) in the stack. Data are taken from the linear stability theory, for $\Delta T = 100$ K and all base pressures of table 4.1. The values on the y axis correspond to a maximum amplitude of pressure oscillations of 100 kPa, fixed for all base pressures.

archy is consistent with the typical orders of magnitude of the specific heat capacity of each thermodynamic condition. Furthermore, for near-critical base pressures, the heat required by the stack increases monotonically. Therefore, for a given ΔT, conditions closer to the critical point do produce more acoustic power, but also required more energy to be sustained.

The efficiency of the thermal-to-acoustic energy transformation can be computed by dividing the produced acoustic power to the total energy required by the stack,

$$\eta = \frac{\overline{\dot{W}}_2 - \overline{\dot{W}}_1}{\overline{\dot{Q}}}. \tag{4.29}$$

This estimate can be more accurately performed if a limit cycle is present (to cancel the unsteady term in Eq. (2.61)). In order to do so, nonlinear effects need to be considered. This is the topic of the next section.

4.5 Limit Cycle and Nonlinear Thermodynamic Effects

A limit cycle can be achieved if pressure amplitudes are sufficiently high to trigger nonlinear losses, which contribute to the acoustic energy budgets (Eq. (2.42)) with a nonlinear dissipation term, resulting in a zero net energy growth. A source of nonlinear dissipation is the vortex shedding at locations of sudden area change, such as the transition from the hot cavity to the stack and from the latter to the resonator (see figure 4.2). These losses, in our computational setup, can be the governing mechanism for the achievement of a limit cycle, without letting shock waves form. In fact, when elevated pressure amplitudes are obtained in a minimal unit setup, shock waves can arise [26], providing high enough nonlinear losses for a limit cycle with their distorted waveforms.

However, pressurized liquids are expected to sustain elevated pressure wave amplitudes without the generation of higher harmonics or shock waves. The pressure amplitude level above which acoustic nonlinearities occur, $|p|_{shocks}$, is approximately equal to the reference pressure $\rho_0 a_0^2$ [53]. Table 4.4 illustrates that considerably high amplitude pressure amplitudes, of the order of hundreds of MPa, are required for shocks to form inside the computational setup. This very high pressure amplitude corresponds to about 15 times the base pressure, a very high value if compared to the 1-2% needed for ideal gases. Indeed, [83] reported higher harmonics in his experiments with a large-scale ideal gas thermoacoustic engine, with pressure amplitudes of 10% of the base pressure, and [26] showed shock waves at 7% of the base pressure in their numerical traveling wave setup. On the other hand, [69], in their liquid sodium thermoacoustic device, at a maximum $|p|_{max}/p_0 = 55\%$, did not report any trace of higher harmonics, and even proposed a future design for which $|p|_{max}/p_0 = 100\%$.

Table 4.4.
Base pressure, base density times square of base speed of sound, equal to the approximate pressure amplitude limit for nonlinear wave propagation, $|p|_{shocks}$, and ratio of $|p|_{shocks}$ over base pressure. In the last row, values of K (Eq. (4.30)) used for the linearized pressure jump entailed by minor area losses. Data are for all the base pressures of table 4.1 and for $T = 293.15$ K.

p_0 (MPa)	7.451	7.746	8.853	10.000	11.066
$\|p\|_{shocks} \simeq \rho_0 a_0^2$ (MPa)	110.36	114.81	130.52	145.69	159.09
$\|p\|_{shocks}/p_0$	14.81	14.82	14.74	14.57	14.38
K	1.3	1.5	2.1	3.4	9.0

4.5.1 Limit Cycle due to Minor Area Losses

Minor losses entail a pressure drop at area jumps, with A_0 the smaller and A_1 the larger area, which can be parametrized as [25]:

$$\Delta\hat{p}_{ml} = -K\left[\left(1-\frac{A_0}{A_1}\right)^2 + \frac{1}{2}\left(1-\frac{A_0}{A_1}\right)^{3/4}\right]\frac{\rho_0|\hat{U}|_{lc}}{A_0^2}\hat{U}, \tag{4.30}$$

which considers losses in steady flow due to expansions (Borda-Carnot formula) together with losses from contractions [85], and employs the largest average velocity $|\hat{U}|/A_0$ in the channel. The value of $|\hat{U}|$ at limit cycle, $|\hat{U}|_{lc}$, is obtained for each area jump iteratively until a zero growth rate is obtained from the numerical solution of Eq.s (2.38a) and (2.38b). In [25], it was shown that the functional dependence of Eq. (4.30) allows for matching of the acoustic power predicted by the linear theory with the Navier-Stokes simulations data. However, recommendation was given on the proper tuning of K to specific numerical or experimental investigations in order to accurately predict the limit cycle physics. In the present study, different values of K, reported in the last row of table 4.4, have been selected to match Navier-Stokes limit cycle pressure amplitude data at low values of ΔT with the linear theory. In addition, for $\Delta T = 26$ K and $p_0/p_{cr} = 1.01$, the axial profile of pressure obtained with the linear

theory augmented with linearized minor losses has been validated with the Navier-Stokes data (not shown). For increasing base pressures, K increases, consistent with the increase in the cold base density ρ_0 (see figure 4.1a): a larger pressure drop is entailed by heavier pseudo-liquid in correspondence of the area jump between right end side of the stack and resonator. Notice that a single value of K is chosen for both the area changes and all values of ΔT, which is an approximation. A more precise estimate would consider different values of K at each location of pressure drop, and varying K with T_{hot} between the hot cavity and the stack. We expect the coefficient K to be lower the more T_{hot} increases, due to the more prevalent presence of ideal gas inside the duct (for which pressure drops are lower), hence our approximation underestimates the pressure amplitude at limit cycle shown in figure 4.16, for high values of ΔT. For those, a more precise estimate, outside the scope of this work, might be needed.

Transcritical thermoacoustic limit cycle pressure amplitudes strongly depend on the base pressure (figure 4.16a). For lower values of p_0, pressure amplitudes, work produced, and heat required are always the highest, due to the peculiar thermodynamic conditions of pseudo-boiling fluids. Thus, as also pointed out by [29], higher power energy densities are achieved by fluids with high thermal expansion coefficient. However, their thermal-to-acoustic efficiency is the highest only for low values of ΔT (up until $\Delta T = 30$ K circa). For increasing ΔT, $p_0 = 1.5 p_{cr}$ is the one entailing the most efficient energy conversion, while $p_0 = 1.01 p_{cr}$ is the least efficient. This is consistent with the theoretical findings of [29], which showed that higher acoustic powers are connected with lower efficiencies. The efficiency increases with ΔT until it reaches a maximum, of 0.87 % for $p_0/p_{cr} = 1.5$ and 120 K, to then decrease for higher values of ΔT. For the sake of comparison, [69] with their liquid sodium thermoacoustic engine obtained 18 W of acoustic power, employing 360 K temperature difference across the stack with 990 W of required heat, for an efficiency of 1.8%. The computational setup used in this work was not originally optimized for thermal-to-acoustic efficiency, but for growth rate instead (see §4.2.2), therefore we expect higher values

of η with future designs. Such improved geometrical setups could achieve a higher efficiency for a lower ΔT, for which p_0 close to p_{cr} is required. Moreover, in a realistic setup, composed of more than one thermoacoustic unit, thermoviscous losses would also be considered for the hot cavity and resonator, reducing the values of limit cycle quantities in figure 4.16a,c,d.

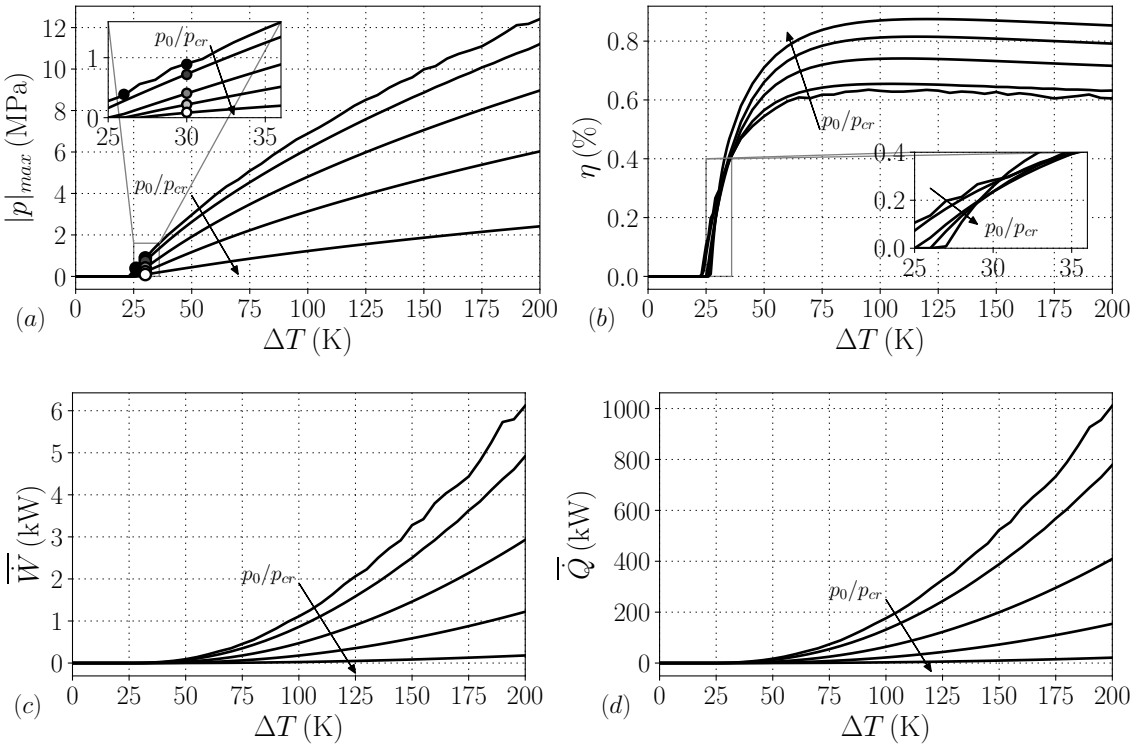

Figure 4.16. Data on limit cycle achieved due to linearized area losses (Eq. (4.30), solid lines), and data extracted from the Navier-Stokes simulations at limit cycle (symbols), for all base pressures of table 4.1. (a): maximum pressure amplitude; (b): thermal-to-acoustic efficiency (Eq. (4.29)); (c): acoustic power produced by the stack; (d) heat required to sustain thermoacoustic oscillations (Eq. (2.61)).

Very high limit pressure amplitudes can trigger also another form of nonlinearity. In fact, transcritical fluids with $p_0 \simeq p_{cr}$ entail base state thermodynamic conditions which vary axially in a strongly nonlinear manner. Therefore, if temperature perturbations at a point inside the stack, close to PB conditions, become significantly high,

strong density variations are expected, hence activating thermodynamic nonlinearities in part of the flow. These nonlinear but concentrated effects at PB conditions are further discussed in the next section, the last of the chapter.

4.5.2 Thermodynamic Nonlinearities at High Pressure Amplitudes

In this section we analyze more in detail the physics of the thermoacoustic oscillations close to the pseudo-boiling region of the stack. In order to magnify and hence clearly see flow oscillations in all variables (not only in pressure), results with strength of the initial dimensionless perturbation of $p_{amp} = 5 \cdot 10^{-3}$, instead of $p_{amp} = 10^{-7}$ (see Eq. (4.8)), are considered.

For $\Delta T = 100$ K and $p_0/p_{cr} = 1.01$, color contours of density profiles (figure 4.17) show rapid and strong fluid oscillations where transcritical conditions are reached (closer to the right end side of the stack). The fluid in PB state periodically pushes and pulls large amount of fluid away and towards it, resulting in strong mechanical force exerted on its surroundings. In addition, the density contours are not symmetric. In fact, at the beginning of the acoustic cycle, the PB density contour ($\rho = 446.671\,\mathrm{kg/m^3}$) is skewed towards the left end side of the stack, where fluid in pseudo-gaseous conditions (lighter) is present. After the standing-wave-like acoustic oscillations force this profile to move rightwards, halfway through the acoustic cycle, the pseudo-boiling fluid is pushing the heavier pseudo-liquid on its right, therefore releasing all its energy much more quickly. Moreover, the phasing between pseudo-gaseous density oscillations ($\rho = 260\,\mathrm{kg/m^3}$) and pseudo-liquid ones ($\rho = 650\,\mathrm{kg/m^3}$) is similar, whereas the pseudo-boiling fluid lags behind, especially in the center of the channel, due to the strong thermal inertia of the pseudo-liquid fluid, as we will discuss below.

On the other hand, for $p_0/p_{cr} = 1.5$, no such effects are detected. In fact, the latter base pressure, being sufficiently higher than the critical pressure, entails stability dynamics more akin to the one of ideal gases: away from strong base density gradients,

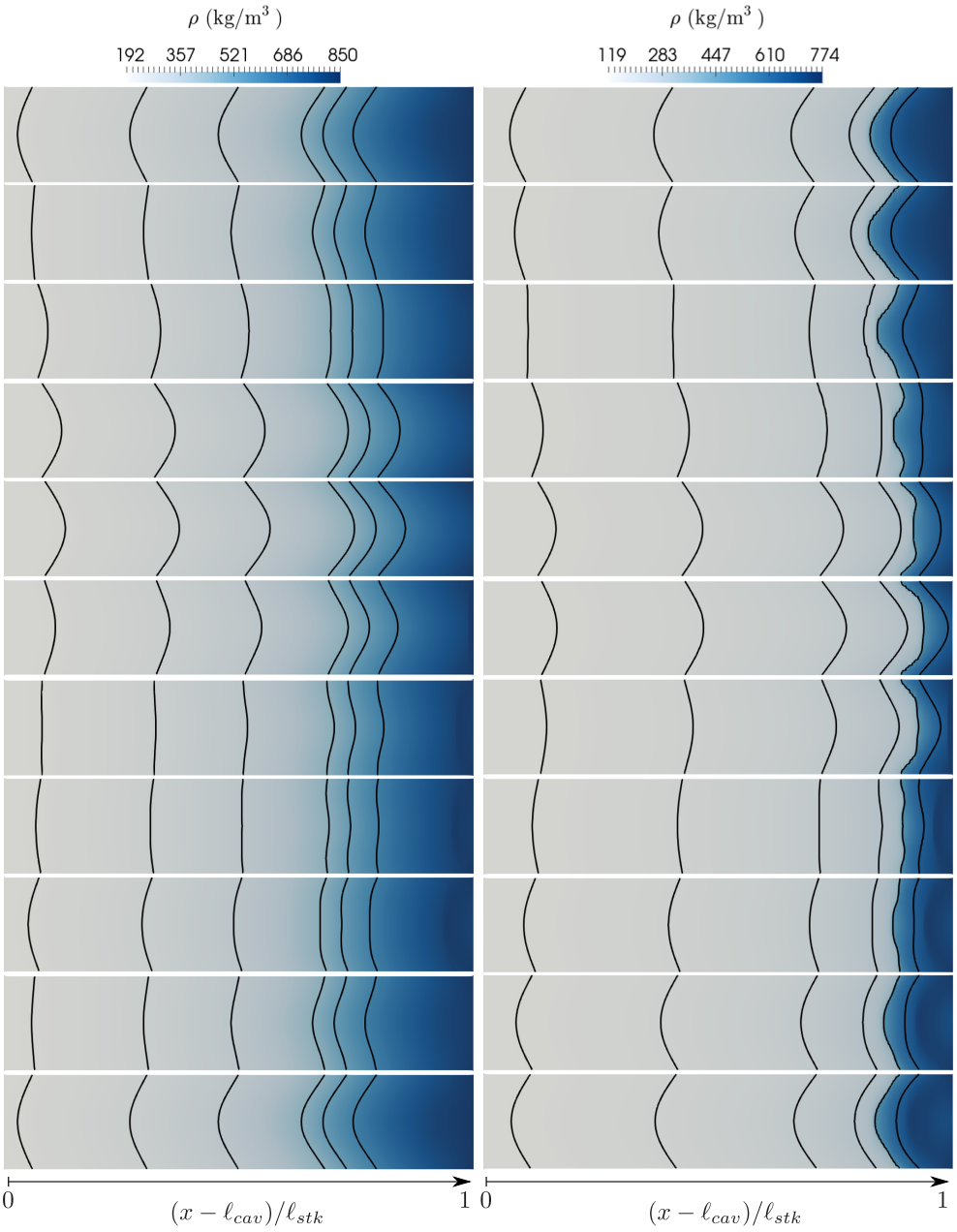

Figure 4.17. Time evolution (from top to bottom), during a complete acoustic period in the transient phase, of color contours of density inside the stack for $\Delta T = 100$ K, for $p_0/p_{cr} = 1.5$ (left) and $p_0/p_{cr} = 1.01$ (right) (see table 4.1), employing grid B with $N = 3$ (see table 4.3). The results are mirrored about the centerline and strecthed 100 times along the y axis for plotting purposes. For these cases, the strength of the initial perturbation is $p_{amp} = 5 \cdot 10^{-3}$ (see Eq. (4.8)). Solid lines indicate isocountours of density for $\rho = 200, 240, 300, 450, 521.197, 620\,\mathrm{kg/m^3}$ (left) and $\rho = 125, 150, 200, 260, 446.671, 650\,\mathrm{kg/m^3}$ (right). The density oscillations shown correspond to pressure oscillations of about 1% of the base pressure for both left and right columns.

the fluid in the stack undergoes mild and symmetric density oscillations, all with about the same relative phasing.

Apart from very high density gradients, transcritical fluids are characterized by other peculiar thermodynamic properties. These include large Prandtl numbers and low thermal diffusivity, which affect the axial profiles of the viscous and thermal boundary layers thicknesses δ_ν, δ_k, defined by

$$\delta_\nu^2 = \frac{2\nu_0}{\omega}, \quad \delta_k^2 = \frac{2k_0}{\omega \rho_0 c_{p_0}} = \frac{\delta_\nu^2}{\mathrm{Pr}_0}, \tag{4.31}$$

which are also a function of the frequency of oscillation. For gases, the Prandtl number is usually less than unity, while for liquids usually $\mathrm{Pr} > 1$. In the PB region, the Prandtl number spikes so much that the thermal boundary layer thickness δ_k can become significantly low, indicating that most of the fluid inside the stack can not be heated or cooled by the wall during an acoustic cycle.

The temperature profile (figure 4.18a), in fact, shows a flat distribution in the center of the pore, mainly due to the high thermal inertia of the oscillating pseudo-boiling fluid, and a nonlinear time phasing. Indeed, when the temperature reaches T_{cr}, the fluid's oscillation rapidly slows down, indicating an increasing thermal resistance, and lags behind the acoustic particles in the other parts of the stack, where PB conditions are not present. When the energy of the oscillation can finally overcome this inertia, the fluid rapidly oscillates away from critical conditions, around which actually the fluid spends the least amount of time. In addition, for $x = 12.31$ cm, the profiles of temperature in the half-channel are smooth and monotone when the oscillations are directed towards the left, where lighter PG fluid is present, whereas they are non-monotone when directed towards the heavier PL fluid on the right.

The profiles of density (figure 4.18c) confirm the nonlinearities observed in figure 4.17. The largest variations in density appear around the critical density ρ_{cr}, resulting in the strongly asymmetric profiles shown by the $x = 12.31$ cm (PL fluid) and $x = 12.11$ cm (PG fluid), while the $x = 12.21$ cm profile (PB fluid) shows a strong nonlinear behavior of the density in the y direction, resembling fast ejection from fluid accelerated from the transcritical region.

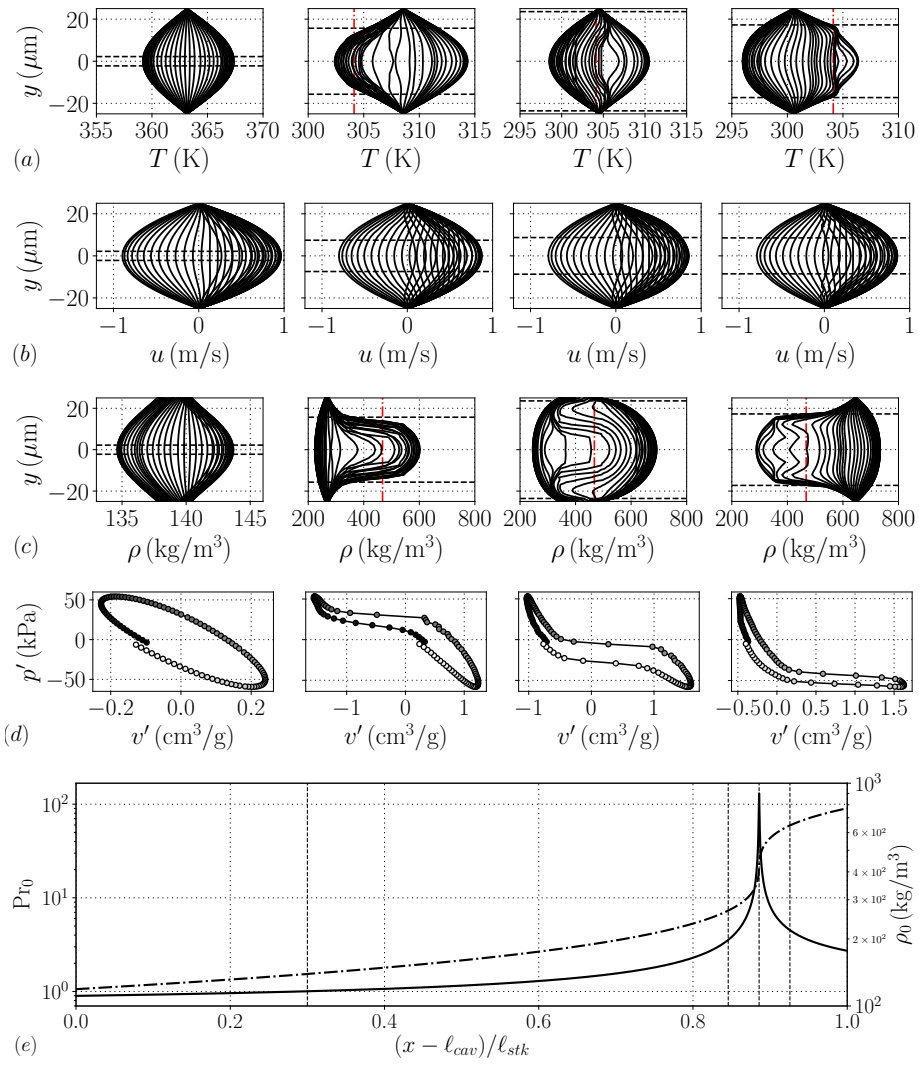

Figure 4.18. Time evolution, during the transient phase, of cross-sectional profiles of temperature (a), axial velocity (b), and density (c) inside the stack, with resulting Lagrangian pressure-volume cycle at the centerline (d), for $\Delta T = 100$ K and $p_0/p_{cr} = 1.01$ (see table 4.2), for grid B with $N = 3$ (see table 4.3). Darker to lighter colored circles indicate increasing time in (d), which considers a complete acoustic period. The results in (a), (b), and (c), for plotting purposes, are mirrored about the centerline, and are considered until 70 % of its completion. Horizontal dashed lines indicate the distance from the walls equal to δ_k in (a) and (c), and δ_ν in (b), and vertical dashed-dotted lines are plotted for $T = T_{cr}$ in (a) and $\rho = \rho_{cr}$ in (c). (e) shows the base density (dashed-dotted line) and the base Prandtl number (solid line), and vertical dashed lines at $x = 10.75\,\text{cm}, 12.11\,\text{cm}, 12.21\,\text{cm}, 12.31\,\text{cm}$, which are the axial coordinates from where the y-profiles in (a), (b), (c) are extracted from, and the initial locations for the acoustic parcel in (d). For this case, the strength of the initial perturbation is $p_{amp} = 5 \cdot 10^{-3}$ (see Eq. (4.8)).

These peculiar features are now shown by the $x = 10.75$ cm section, where the time scale of the oscillating fluid (acoustics) matches well the time of thermal diffusion in the y direction, hence allowing for harmonic temperature and density perturbations. Furthermore, the cross-sectional velocity profiles resemble their linear counterparts predicted by the theory of Rott, and do not show significant changes among the different fluid regions (figure 4.18b). This indicates that real-fluid effects mainly affect the oscillating thermodynamic variables, such as density and temperature, and not the velocity. This is because the viscous boundary layer thickness δ_ν covers most of the fluid inside the stack in all its regions, and does not vary as significantly as the thermal boundary layer thickness δ_k.

As a result of the PB thermodynamics, for such high pressure amplitudes, the linear relation between density and temperature (Eq. (2.27)), which holds for small amplitude wave amplitudes, is replaced by a fully nonlinear relationship. This causes the Lagrangian pressure volume cycle in the linear regime (figure 4.13), which is still reproduced at the $x = 10.75$ cm section (and by high base pressures, not shown), to be modified and distorted (figure 4.18d). However, the thermodynamic nonlinearities investigated in this section are concentrated in a small region of the stack close to fluid in PB condition. Therefore their effect as nonlinear losses can be negligible if the value of ΔT is low and the base pressure is away from the critical pressure. In fact, the limit cycle pressure amplitudes from the Navier-Stokes simulations at the low values of ΔT analyzed in §4.5.1 are reproducible just with the linear theory augmented with linearized minor losses. For higher values of ΔT, and hence of pressure amplitudes, the thermodynamic nonlinearities present around the PB fluid can in principle propagate further in the stack, and also in the resonator, hence changing considerably the mechanisms of acoustic energy production and dissipation, which would make the use of a linear theory obsolete for $p_0 \simeq p_{cr}$. This analysis, outside of the scope of this chapter, needs further investigation and will be analyzed in future work.

5. HEAT-RELEASE-INDUCED WAVES IN SUPERCRITICAL FLUIDS

We have performed 186 highly resolved fully compressible one-dimensional Navier-Stokes simulations of freely propagating acoustic and heat-release-induced compression waves up to Mach 2.95, spanning five orders of magnitude of heat release rate, in a canonical semi-infinite domain flow problem. Six different fluids, each taken in four different states ranging from compressible liquid to ideal gas, are considered; real-fluid thermodynamic properties are modeled via the Peng-Robinson equation of state. New dimensionless scaling laws valid for a generic homogenous single-phase compressible fluid, where a uniform and quiescent base state (or initial condition) is assumed, are able to collapse the whole dataset in the isentropic as well as the non-isentropic regime, together with one experimental result of Miura *et al.*, Phys. Rev. E, 2006. The classic isentropic acoustic scaling parameters are revisited, showing that the reference temperature and heat release rate need to be expressed in terms of the isobaric thermal expansion coefficient to ensure collapse of thermo-fluid-dynamic fluctuations across all fluids. The proposed dimensionless scaling strategy formally removes fluid-dependent parameters from the Rankine-Hugoniot equations, enabling prediction of wave Mach numbers, heat-release-induced shock wave intensity, and thermal-to-mechanical power conversion efficiency. Finally, the scaling supports the derivation of a fully predictive model for heat-release-induced shock intensity, shedding light onto the asymptotic limit of infinite Mach number.

5.1 Introduction

When compressible fluids are thermally perturbed, a mechanical response is generated in the form of waves [86, 87], from near-isentropic compressions [88] to shock waves [89]. Heat-release-induced waves appear in a wide variety of artificial and nat-

ural phenomena, such as the sound produced from asteroids' impact on Earth's atmosphere [90,91], blast waves from nuclear explosions [92], thermophones [93], shock waves induced by spark discharge [94], and space manufacturing processes [95]. Moreover, heat-release-induced fluctuations, referred to by some authors as thermoacoustic waves [96,97] or thermoacoustic sound [93], are the governing mechanism for thermal relaxation in near-critical fluids in enclosed cavities [98–104], referred to as the piston effect [100] or thermoacoustic convection [105]. Such theories have been widely verified via numerical simulations [32,97,102,106–110] and experiments [88,105,109,111].

In spite of such formidable efforts, fully predictive models for heat-release-induced wave intensity in a generic compressible fluid have been derived only for isentropic waves [88], or for non-isentropic waves but only propagating in calorically perfect ideal gases [112]. Furthermore, previously reported scaling relationships for (in general non-isentropic) heat-release-induced waves [112] fail to scale appropriately the thermodynamic jumps, even for perfect ideal gases, as discussed in §5.3.2. While the latter issue has no direct impact on the ability to formulate a fully predictive model, it does hinder its development, as shown in §5.4. To the authors' knowledge, there have been no prior attempts towards developing a dimensionless scaling strategy able to provide a unified description of isentropic and non-isentropic heat-release-induced waves across different fluids in different thermodynamic states.

Limited attention has also been given to scaling of perturbations and/or jumps in temperature and enthalpy. This has deep roots into the common practice in acoustics to use, when possible, pressure and velocity fluctuations (or pressure only) as the sole working variables. This choice is consistent with the fundamental nature of sound waves, i.e. self-propagating patterns of compressions and dilatations, inducing and induced by spatial gradients in particle displacements or velocities. No other variables but pressure and velocity are thus needed to intuitively understand sound propagation and the mechanical or acoustic power associated with it. As a result, the traditional approach to deriving a dimensionless set of linearized governing wave equations has so far been focused on collapsing pressure and velocity fluctuations only.

In reality, waves in compressible fluids are propagating disturbances affecting all thermo-fluid-dynamic variables. A secondary role is attributed to fluctuations in other quantities, such as temperature or enthalpy, used, respectively, by [67] in his qualitative explanation of viscous and conductive effects on sound waves, and by [113] as main acoustic field. The temperature and enthalpy of the base state are typically employed to scale respective fluctuations. However, as demonstrated in §5.3.1, simply using the fluid's base temperature to scale temperature fluctuations does *not* yield dimensionless collapse of temperature fluctuations, not even among different calorically perfect ideal gases under isentropic conditions. The departure from full collapse is worse when various real fluids in multiple states are considered.

This realization led us to the reformulation of the reference temperature in terms of the isobaric thermal expansion coefficient (§5.3.1), enabling the collapse of thermo-fluid-dynamic linear acoustic fluctuations across all fluids. This then paved the way to the redefinition of the dimensionless heat release rate (§5.3.2), enabling to cast d'Alembert's analytical solution of the wave equation in dimensionless form, scaling effectively the predictive isentropic law obtained by [88]. The remarkable finding is that such isentropic scaling is the necessary stepping stone towards deriving dimensionless scaling laws for the prediction of the wave Mach number (§5.3.3) and modeling of non-isentropic heat-release-induced shock wave dynamics (§5.4), up until Mach infinity (§5.4.3), for all compressible fluids.

In this chapter, the superscript (*) denotes dimensional quantities, and is omitted in their dimensionless counterpart.

5.2 Problem Formulation

5.2.1 Selection of Fluids

Fluids at supercritical pressures exhibit variations in important properties such as density, speed of sound, and thermal capacity, ranging from liquid-like to gas-like

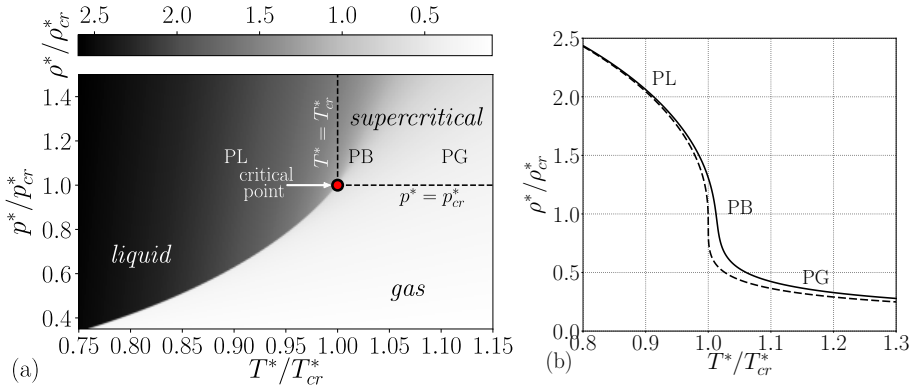

Figure 5.1. (a) Phase diagram of CO_2 showing flooded contours of reduced density ρ^*/ρ^*_{cr}; (b) reduced density of CO_2 versus reduced temperature T^*/T^*_{cr} for $p^* = p^*_{cr}$ (dashed line) and $p^* = 1.1p^*_{cr}$ (solid line). Both plots are generated with the PR EoS (Eq. (2.1)). PL, PB, PG indicate pseudo-liquid, pseudo-boiling, and pseudo-gaseous conditions.

depending on their temperature, making them a very attractive choice for the scope of the present investigation.

A supercritical state is reached when the fluid is at temperatures and pressures exceeding its critical values (indicated by the subscript "cr"), $T^* > T^*_{cr}$ and $p^* > p^*_{cr}$, respectively (figure 5.1a). For a fixed supercritical pressure (chosen as $p^*_0 = 1.1p^*_{cr}$ in this study), starting from cold and heavy pseudo-liquid (PL), the density rapidly drops for increasing temperatures (figure 5.1b) via a pseudo-boiling (PB), or pseudo-phase transitioning, process [13–15], after which the fluid reaches a pseudo-gaseous (PG) state, and then eventually a near-ideal-gas state (IG) for sufficiently high temperatures. This behavior can be captured by adopting analytically-defined equations of state for real fluids, which enable a thermodynamically consistent closure of the governing flow equations.

Table 5.2.1 reports values of the aforementioned fluid model parameters, all taken from [22] and [20], for the six fluids considered, which are carbon dioxide (CO_2), oxygen (O_2), nitrogen (N_2), methanol (CH_3OH), 1,1,1,2-Tetrafluoroethane (CH_2FCF_3 or R-134a), and octafluoropropane (R-218). All of the thermodynamic derivatives

Table 5.1.
Marker legend for the selected six fluids, each considered in four different reference states represented by greyscale levels. Black: dense compressible fluid, pseudo-liquid (PL); dark grey: pseudo-boiling fluid (PB); light grey: light supercritical fluid, pseudo-gas (PG); white: supercritical fluid in near ideal-gas conditions (IG). All cases are considered at $p_0^* = 1.1 p_{cr}^*$. Values of fluid-specific properties required by the PR EoS are also reported.

fluid	PL	PB	PG	IG	T_{cr}^*(K)	p_{cr}^*(MPa)	M_m^*(g/mol)	ω
CO_2	●	●	○	○	304.13	7.3773	44.010	0.22394
O_2	▲	▲	△	△	154.58	5.043	31.999	0.0222
N_2	▼	▼	▽	▽	126.20	3.398	28.014	0.0370
CH_3OH	■	■	□	□	512.64	8.097	32.042	0.565
R-134a	♦	♦	◊	◊	374.26	4.059	102.032	0.326
R-218	⬟	⬟	⬠	⬠	345.10	2.68	188.020	0.325
T_0^*/T_{cr}^*	0.89	1.02	1.11	2.20				
p_0^*/p_{cr}^*	1.10	1.10	1.10	1.10				

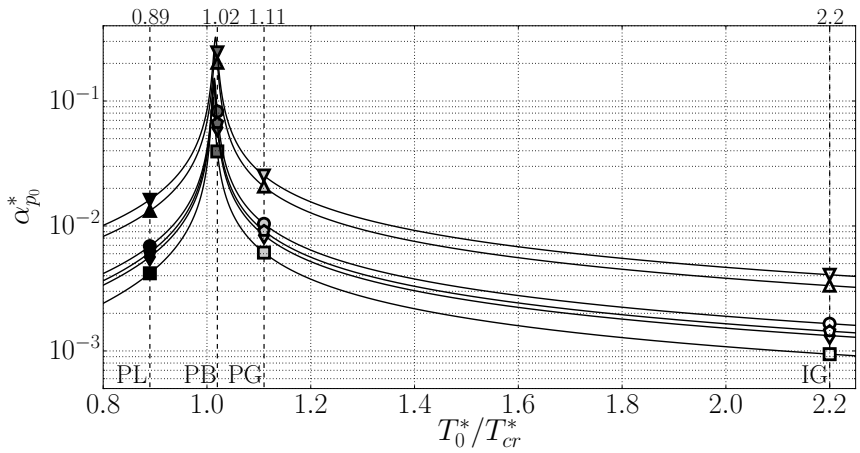

Figure 5.2. Isobaric thermal expansion coefficient versus the reduced temperature T^*_0/T^*_{cr} for all fluids and conditions in table 5.2.1. The superscript $(^*)$ denotes dimensional quantities.

required by the following analytical derivations can be computed directly from Eq. (2.1), retaining full thermodynamic consistency with data from the high-fidelity simulations. The other thermodynamic quantities are computed with the thermodynamic departure function approach as described in [20]. A Newton-Raphson-based iterative method is employed to obtain temperature from density and internal energy.

The isobaric thermal expansion coefficient (figure 5.2), is an important thermodynamic variable that will be used herein as scaling parameter (table 5.3) for heat-release-induced isentropic and non-isentropic fluctuations. The same quantity is used to select the different base conditions shown in table 5.2.1. Indeed, we here define the pseudo-boiling state as the region in the immediate vicinity of the maxima of α^*_p (PB, $T^*_0 = 1.02T^*_{cr}$), with pseudo-liquid (PL, $T^*_0 = 0.89T^*_{cr}$) and pseudo-gas (PG, $T^*_0 = 1.11T^*_{cr}$) being the states for lower and higher temperatures, respectively. For the ideal gas (IG) state, we choose $T^*_0 = 2.2T^*_{cr}$, a state at which $\alpha^*_{p_0}T^*_0 \approx 1$ and that can hence be modeled with the perfect ideal gas EoS, $p^* = \rho^* R^* T^*$, and with a (constant) ratio of specific heats γ, taken equal to the ratio of c^*_p and c^*_v given by the PR EoS at $T^* = 2.2T^*_{cr}$ and $p^* = 1.1p^*_{cr}$. Such reference conditions are indicated with

the subscript "0" and are used as both the acoustic base state in §5.3.1 and initial conditions in the heat-release cases (§5.3.2, §5.3.3, §5.4)

5.2.2 Computational Setup

The governing equations for a fully compressible one-dimensional viscous flow read

$$\frac{\partial \rho^*}{\partial t^*} + \frac{\partial \rho^* u^*}{\partial x^*} = 0, \qquad \frac{\partial \rho^* u^*}{\partial t^*} + \frac{\partial (\rho^* u^{*2} + p^*)}{\partial x^*} = \frac{\partial \tau^*}{\partial x^*}, \tag{5.1}$$

for mass and momentum, respectively, and

$$\frac{\partial \rho^* E^*}{\partial t^*} + \frac{\partial \left(\rho^* u^* E^* + p^* u^*\right)}{\partial x^*} = \frac{\partial u^* \tau^*}{\partial x^*} - \frac{\partial q^*}{\partial x^*} + \dot{Q}^*, \tag{5.2}$$

for total energy, where t^* is time, x^* is the spatial coordinate, u^* is the velocity, ρ^* is the density, p^* is the thermodynamic pressure, and $E^* = e^* + u^{*2}/2$ is the specific, i.e. per unit mass, total energy (sum of specific internal energy and specific kinetic energy). The superscript $(^*)$ denotes dimensional quantities. The Newtonian viscous stresses, expressed in accordance with Stokes's hypothesis, and the heat flux, modeled with Fourier heat conduction, are

$$\tau^* = \frac{4}{3}\mu^* \frac{\partial u^*}{\partial x^*}, \qquad q^* = -k^* \frac{\partial T^*}{\partial x^*}, \tag{5.3}$$

where μ^* is the dynamic viscosity, k^* is the thermal conductivity, and T^* the absolute or thermodynamic temperature. The spatial distribution of the imposed volumetric heat release rate $\dot{Q}^*$ is expressed as

$$\dot{Q}^*(x^*, t^*) = \Omega^* g^*(x^*), \qquad g^*(x^*) = \frac{1}{\ell^* \sqrt{2\pi}} e^{-\frac{1}{2}(x^*/\ell^*)^2}, \tag{5.4}$$

respectively, where Ω^* (W/m^2) is the planar heat release rate (table 5.2) and $g^*(x^*)$ (m^{-1}) is a Gaussian function with unitary (non-dimensional) integral on the real axis,

$$\int_{-\infty}^{\infty} g^*(x^*) dx^* = 1, \tag{5.5}$$

with characteristic width $\ell^* = 0.75\,\mu$m, inspired by the thin foil heater in the experiments of [88].

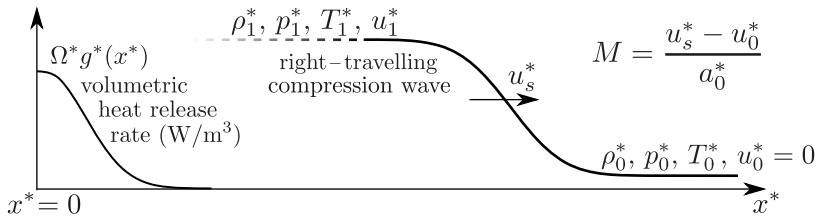

Figure 5.3. Computational setup for heat-release-induced wave generation. The superscript (*) denotes dimensional quantities. The post-compression state is denoted with the subscript "1", while pre-compression (or initial) states are denoted with the subscript "0".

Table 5.2.
Planar heat release rates used in numerical simulations of heat-release-induced waves. Values of the order of 10^{11} (†) are used only for pseudo-liquid (PL) conditions (see table 5.2.1).

Ω^* (W/m^2)	10^5	10^7	10^9	10^{10}	$3{\times}10^{10}$	$6{\times}10^{10}$	$^\dagger 10^{11}$	$^\dagger 3{\times}10^{11}$	$^\dagger 6{\times}10^{11}$

Simulations are carried out only for $x^* \geq 0$, with symmetry conditions imposed at $x^* = 0$, and halted before perturbations reach the right boundary (located at $x^* = 40\mu$m). The computational domain is sufficiently long to allow waves to form and be tracked to measure the propagation Mach number, M (see figure 5.3). The analysis below focuses solely on the peak wave speed, that is measured upon coalescence of compression waves, when and if shock formation occurs.

Numerical data is generated for six different fluids at supercritical pressure conditions $p_0^* = 1.1\, p_{cr}^*$, each taken at four different temperatures yielding pseudo-liquid (PL), pseudo-boiling (PB), pseudo-gaseous (PG), and ideal-gas (IG) conditions, (see table 5.2.1). This results in a total of 24 distinct thermodynamic base (or initial) states, spanning an overall pressure, temperature, and density range, respectively, of approximately $p_{0,max}^* - p_{0,min}^* = 6\,$MPa, $T_{0,max}^* - T_{0,min}^* = 1016\,$K, and $\rho_{0,max}^* - \rho_{0,min}^* = 1340$kg/m^3. For each base state, simulations are performed at several values of planar heat release spanning 5 orders of magnitude (see table 5.2),

bounded by the occurrence of complete rarefaction of the fluid ($\rho^* \to 0$) at the location of heat injection.

Fully compressible high-order Navier-Stokes simulations are performed with the solver *Hybrid* [114]. A fully conservative discretization is employed to predict the correct shock speed [37]. The compression wave fronts are resolved with at least 14 grid points (for the highest Mach number reproduced), corresponding to a grid spacing of $\Delta x^* = 0.04\,\mu$m, and with a time step of at most $\Delta t^* = 0.01\,$ns. While the shock profile, especially for the higher Mach number cases, is not physically accurate [115], this strategy avoids the adoption of shock capturing schemes, and still very accurately predicts the jump of the thermo-fluid-dynamic quantities across the shock. Moreover, because of the very high numerical resolution employed, the results were not hindered by spurious pressure oscillations commonly associated with transcritical flows [36, 50], which are commonly contained by adopting dissipative and/or non-conservative schemes [34, 35].

In the following section, the proposed dimensionless scaling strategy, based on isentropic flow approximations, is introduced and applied to the whole dataset of 186 simulations at once, even for strongly non-isentropic data, paving the way for the modeling effort in §5.4, extended to the limit of infinite shock strength.

5.3 Dimensionless Scaling Strategy

The present dimensionless analysis includes fundamental considerations regarding dimensionless scaling of temperature fluctuations of isentropic acoustic waves (§5.3.1), which are then extended to the case of heat-release-induced waves (§5.3.2), identifying a demarcation between isentropic and non-isentropic waves, and are finally used to scale the Rankine-Hugoniot (RH) equations, leading to a dimensionless predictive law for the propagation wave speed (§5.3.3). The entire dataset is analyzed, including non-isentropic data, demonstrating remarkable scaling properties in that regime as well. As previously stated, seeking a scaling strategy able to collapse data from different

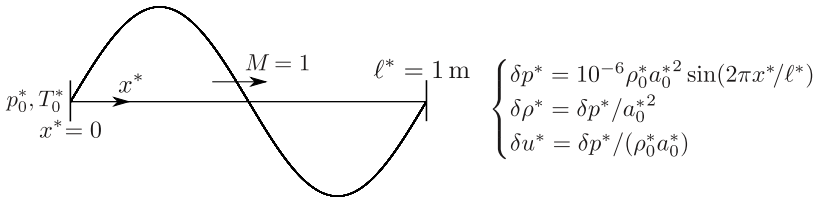

Figure 5.4. Initial conditions for the waves in a periodic domain $[0, \ell^*]$, where the initial fluctuating temperature field is obtained via the equation of state (Eq. (2.1)) for each fluid.

fluids and in different thermodynamic states is used herein as the first step conducive to a broader modeling effort valid for a generic compressible fluid.

5.3.1 Freely Propagating Acoustic Waves

We start from the simple case of planar isentropic acoustic waves evolving in a uniform quiescent base state, hereafter indicated with the subscript "0". In this case pressure δp^* and velocity δu^* fluctuations are the only quantities needed to completely characterize the flow; the proper and commonly used normalization choice is

$$\delta p = \frac{\delta p^*}{\rho_0^* a_0^{*2}}, \qquad \delta u = \frac{\delta u^*}{a_0^*}, \qquad x = \frac{x^*}{\ell^*}, \qquad t = \frac{t^*}{\ell^*/a_0^*}, \tag{5.6}$$

where ρ_0^* and $a_0^* = \sqrt{\partial p^*/\partial\rho^*|_{s^*,0}}$ are the base density and isentropic speed of sound, and x^* and t^* the independent spatial and temporal coordinates, and ℓ^* a reference length scale. Applying the normalization in Eq. (5.6) to the linearized continuity and momentum equations, assuming isentropic flow, yields

$$\frac{\partial}{\partial t}\delta u = -\frac{\partial}{\partial x}\delta p, \qquad \frac{\partial}{\partial t}\delta p = -\frac{\partial}{\partial x}\delta u, \tag{5.7}$$

whose solution in an unbounded domain can be expressed without loss of generality in the self-similar form

$$\delta u_\pm = \pm\delta p_\pm = f_\pm(\zeta_\pm). \tag{5.8}$$

The two functions $f_\pm(\cdot)$ of the travelling-wave coordinate $\zeta_\pm = x \mp t$ (assuming unitary wave Mach number) can be independently and arbitrarily assigned with the

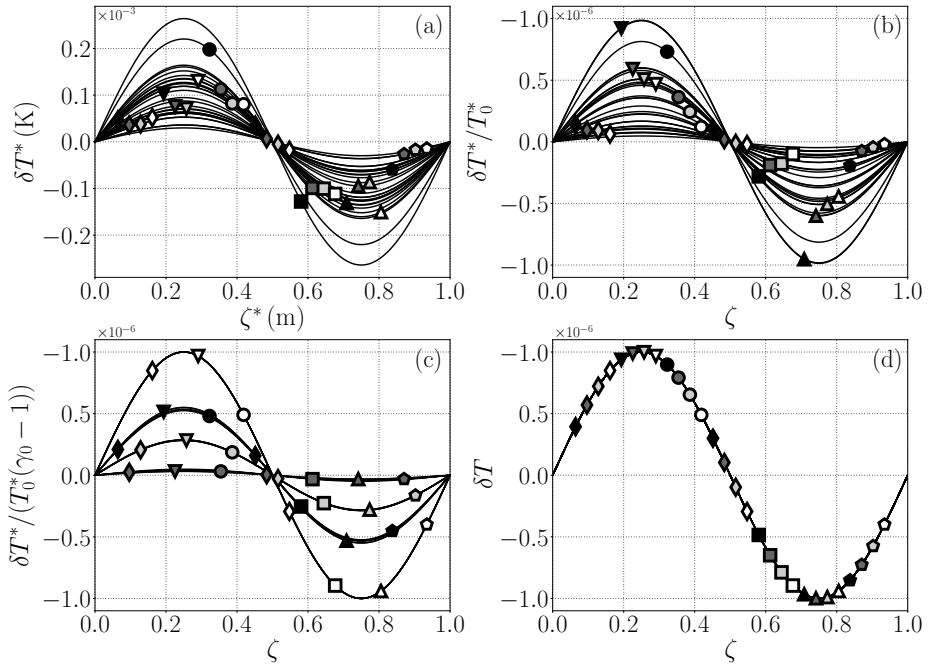

Figure 5.5. Scaling of temperature fluctuations from inviscid computations of isentropic right-travelling acoustic waves for $f(\zeta) = 10^{-6}\sin(2\pi\zeta)$ (see Eq. (5.8)) for all fluids and conditions in table 5.2.1. (a) Dimensional temperature perturbations; (b) commonly adopted normalization via base temperature; (c) normalization only collapsing IG data; (d) proposed scaling collapsing all fluids across all states (table 5.3). Same results are obtained for other variables such as δe, δh, and $\delta\rho$ (not shown). Initial conditions for this case are shown in figure 5.4.

caveat that $\max_\zeta |f(\zeta)| << 1$ to respect assumptions of linearity. The dependency on the base state, and hence also on the specific fluid properties, of the governing equations (5.7) has been completely absorbed by the normalization (5.6). *The steps leading to Eq.* (5.7) *and Eq.* (5.8) *do not require the specification of an equation of state nor of an explicit normalization for temperature fluctuations* δT^*; however, they do entail the normalization $\delta\rho = \delta\rho^*/\rho_0^*$. Without loss of generality, the following analysis will focus on right-travelling waves only, hence $f(\zeta) = f_+(\zeta)$.

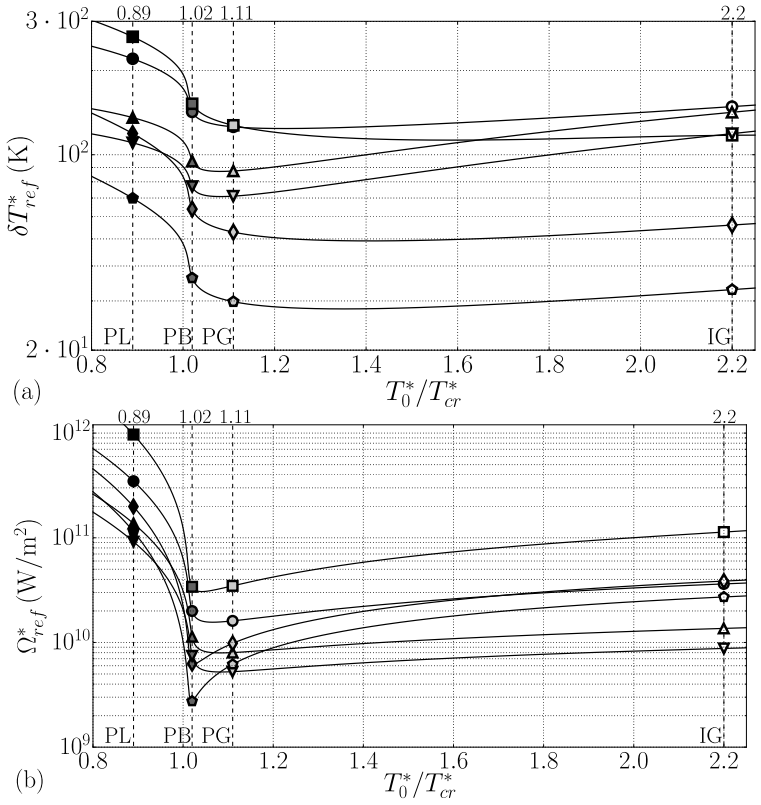

Figure 5.6. Reference scaling parameter for temperature fluctuations (a), δT^*_{ref}, and reference scaling parameter for heat release rate (b), Ω^*_{ref}, both versus reduced temperature for all fluids and conditions in table 5.2.1.

We first observe how the commonly adopted normalization of temperature fluctuations δT^*, which uses the base state temperature T_0^* as a reference [116], does *not*

collapse isentropic temperature perturbations, associated to the same dimensionless waveform $f(\zeta)$ (figure 5.5a), across different fluids; surprisingly, not even across different fluids in ideal gas conditions (figure 5.5b). This issue is trivially resolved by expressing an isentropic fluctuation of a generic quantity $\delta\varphi^*$ as a sole function of the fluctuation in a given quantity, for example pressure, via evaluation of the thermodynamic derivative $\delta\varphi^*/\delta p^* = \partial\varphi^*/\partial p^*|_{s^*,0}$, yielding, for a generic compressible fluid,

$$\delta T^* = \frac{\alpha^*_{p_0} T^*_0}{\rho^*_0 c^*_{p_0}} \delta p^*, \qquad \delta h^* = \frac{1}{\rho^*_0} \delta p^*, \qquad \delta e^* = \frac{p^*_0}{\rho^{*2}_0 a^{*2}_0} \delta p^*, \tag{5.9}$$

where δh^* and δe^* are the specific (per unit mass) enthalpy and internal energy fluctuations, $c^*_{p_0}$ is the isobaric specific thermal capacity calculated at base state conditions, indicated with a subscript "0". Applying the relation $a^{*2}_0 T^*_0 {\alpha^*_{p_0}}^2 / c^*_{p_0} = \gamma_0 - 1$, where $\gamma_0 = c^*_{p_0}/c^*_{v_0}$ is the ratio of specific isobaric and isochoric thermal capacities, and the normalization in Eq. (5.6), to Eq. (5.9), yields

$$\delta T = \frac{\alpha^*_{p_0}}{\gamma_0 - 1} \delta T^*, \qquad \delta h = \frac{1}{a^{*2}_0} \delta h^*, \qquad \delta e = \frac{\widetilde{\gamma}_0}{a^{*2}_0} \delta e^*, \tag{5.10}$$

which achieves the desired collapse for temperature (figure 5.5d), specific enthalpy (not shown), and specific internal energy fluctuations (not shown), where $\widetilde{\gamma}_0 = \rho^*_0 a^{*2}_0 / p^*_0$ is the isentropic exponent [117]. The reference scaling parameter for the specific enthalpy ($\delta h^*_{ref} = a^{*2}_0$) also holds for the specific total enthalpy $H^* = h^* + u^{*2}/2$ (used by [113] as the primary working variable to study acoustics) but not for specific total energy.

Ideal gas temperature perturbations made dimensionless only via T^*_0 (figure 5.5b) do not collapse unless $\gamma_0 - 1$ is also taken into consideration (figure 5.5c). The same result holds for enthalpy fluctuations (not shown). In fact, for a perfect ideal gas, the proposed scaling parameters revert to $\delta T^*_{ref}|_{IG} = (\gamma_0 - 1) T^*_0$, $\delta h^*_{ref}|_{IG} = \gamma_0 R^* T^*_0$.

Equations (5.6) and (5.10) define the complete set of scaling parameters, summarized in table 5.3, collapsing all isentropic thermo-fluid-dynamic fluctuations across different fluids, and, incidentally, also among themselves,

$$\delta p = \delta \rho = \delta T = \delta h = \delta e = f(\zeta), \tag{5.11}$$

which is a direct result of the single degree of thermodynamic freedom. Eq. (5.11) holds for both left- and right- travelling waves, with respective velocity fluctuations given by $\delta u = -\delta p$ and $\delta u = \delta p$.

Table 5.3.
Set of reference scaling parameters yielding collapse of isentropic acoustic and heat-release-induced waves (§5.3.2, §5.3.3) propagating in a uniform generic compressible fluid.

δp^*_{ref}	δu^*_{ref}	$\delta \rho^*_{ref}$	δT^*_{ref}	δh^*_{ref}	δe^*_{ref}	Ω^*_{ref}
$\rho^*_0 a^{*2}_0$	a^*_0	ρ^*_0	$(\gamma_0 - 1)/\alpha^*_{p_0}$	a^{*2}_0	$a^{*2}_0/\widetilde{\gamma}_0$	$2\rho^*_0 a^*_0 c^*_{p_0}/\alpha^*_{p_0}$

5.3.2 Heat-Release-Induced Perturbations

In this section we extend the approach in §5.3.1 to scaling of heat-release-induced waves, which is the main objective of this chapter as outlined in §5.2.2. Such waves are originated because of the fluid expansion that, acting like a piston [112], generates compression waves.

The first step is to recast Eq. (5.7) as the linearized dimensionless wave equation,

$$\frac{\partial^2}{\partial t^2}\delta p - \frac{\partial^2}{\partial x^2}\delta p = 0, \tag{5.12}$$

which needs initial conditions on δp,

$$(\delta p)_{t=0} = 0, \tag{5.13}$$

and on $\partial \delta p/\partial t$. In order to find the latter, Eq. (5.2) can be rewritten as the evolution equation for pressure [53],

$$\frac{\partial p^*}{\partial t^*} + u^*\frac{\partial p^*}{\partial x^*} = -\rho^* a^{*2}\frac{\partial u^*}{\partial x^*} + \frac{\alpha^*_p a^{*2}}{c^*_p}\left(\tau^*\frac{\partial u^*}{\partial x^*} - \frac{\partial q^*}{\partial x^*} + \Omega^* g^*(x^*)\right), \tag{5.14}$$

which evaluated at the initial time yields

$$\left(\frac{\partial p^*}{\partial t^*}\right)_{t^*=0} = \frac{\alpha^*_{p_0} a^{*2}_0}{c^*_{p_0}}\Omega^* g^*(x^*), \tag{5.15}$$

which is, using the normalization in Eq. (5.6),

$$\left(\frac{\partial \delta p}{\partial t}\right)_{t=0} = \frac{\Omega^* l^* g^*(x^*)}{\rho_0^* a_0^* c_{p_0}^* / \alpha_{p_0}^*}. \tag{5.16}$$

With the initial conditions imposed by Eq.s (5.13) and (5.16), d'Alembert's analytical solution of Eq. (5.12) is given by

$$\delta p = \frac{\Omega^*}{2\rho_0^* a_0^* c_{p_0}^* / \alpha_{p_0}^*} \frac{\mathrm{erf}\left(\sqrt{2}(x+t)/2\right) - \mathrm{erf}\left(\sqrt{2}(x-t)/2\right)}{2}, \tag{5.17}$$

which is made dimensionless as follows:

$$\delta p = \Omega \frac{\mathrm{erf}\left(\sqrt{2}(x+t)/2\right) - \mathrm{erf}\left(\sqrt{2}(x-t)/2\right)}{2}, \tag{5.18}$$

where Ω^* is normalized with Ω_{ref}^* (table 5.3, figure 5.6b),

$$\Omega = \frac{\Omega^*}{\Omega_{ref}^*} = \frac{\Omega^*}{2\rho_0^* a_0^* c_{p_0}^* / \alpha_{p_0}^*}. \tag{5.19}$$

The dimensionless result in Eq. (5.18) completely removes the dependency from the base state, allowing to extend results obtained from experiments carried out with ideal gases to other fluids and real-gas conditions, provided that conditions of isentropicity are respected.

In fact, analogously to figure 5.5, figure 5.7 shows how previously adopted normalizations of heat-release-induced waves, such as the one by [112] (figure 5.7b) can be extended to yield partial collapse (figure 5.7c), ultimately only achieved in full by the proposed scaling (figure 5.7d). The compressions profiles shown in figure 5.7 refer to heat-release-induced waves in their quasi-isentropic regime, with $\Omega^* = 10^5\,\mathrm{W/m^2}$ and with maximum Mach number equal to $M = 1.00003$. According to [115], the shock wave structure obtained from the Navier-Stokes equations is physically relevant for wave Mach numbers significantly below two, which is the case for the data shown in figure 5.7. For such a low heat release rate, the compression waves satisfy the hyperbolic problem described by the linearized wave equation (Eq. (5.12)) and their dimensionless profiles all collapse into the functional law of Eq. (5.18). Thermoviscous effects, which are accounted for in the simulations, are responsible for the very slight mismatch between numerical and analytical results in figure 5.7d.

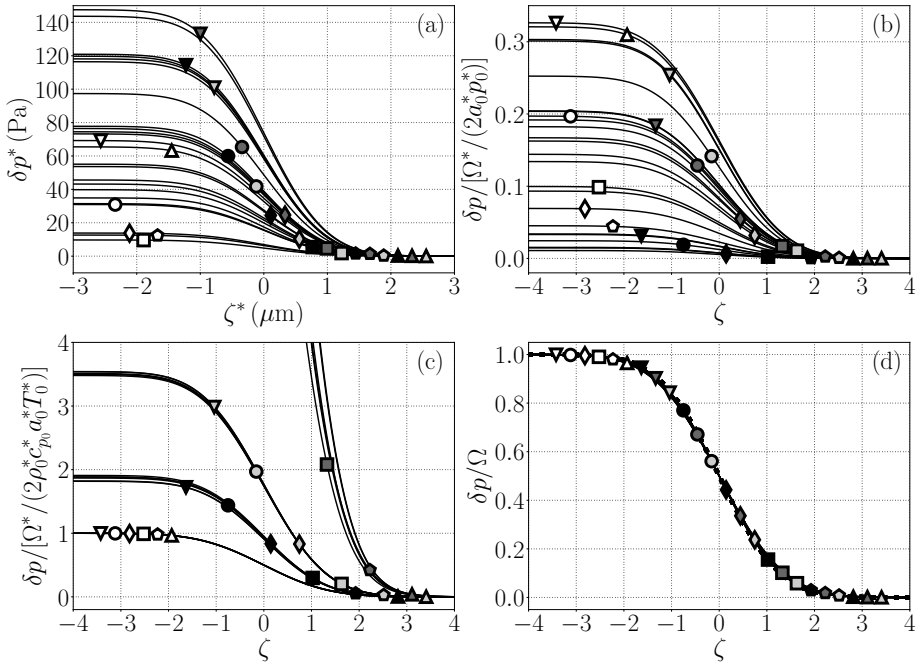

Figure 5.7. Scaling of pressure waveforms of quasi-isentropic heat-release-induced waves for dimensional heat release rate $\Omega^* = 10^5\,\mathrm{W/m^2}$. (a) Dimensional pressure profiles; (b) scaling proposed by [112]; (c) scaling only collapsing IG data; (d) proposed scaling (Eq. (5.19), table 5.3, figure 5.6b). The solution of the dimensionless wave equation (Eq. (5.18)) is plotted as a thick dotted line in (d). The maximum wave Mach number of the data shown herein is $M = 1.00003$, and the dimensionless heat release rate Ω ranges from $1.033 \cdot 10^{-7}$ to $3.634 \cdot 10^{-5}$.

The maximum value of δp in Eq. (5.18) is equal to the dimensionless pressure jump across the compression wave,

$$\Pi = \frac{p_1^* - p_0^*}{\rho_0^* a_0^*}, \tag{5.20}$$

where the subscript "1" indicates the post-compression state (figure 5.3). Eq. (5.20) is the classic definition of shock strength [118], which can be obtained, in the case of isentropic heat-release-induced waves, with the straightforward dimensionless relationship

$$\Pi = \Omega, \tag{5.21}$$

adopting the reference scaling parameter for the heat release rate in Eq. (5.19). [88], assuming low heat release rates and isentropic waves, predicted the amplitude of heat-release-induced compression waves via

$$p_1^* - p_0^* = \frac{\rho_0^* a_0^*}{T_0^*} \left(\frac{\partial T^*}{\partial p^*} \right)_{s^*,0} \frac{\Omega^*}{2}. \tag{5.22}$$

Using the thermodynamic relation

$$\left(\frac{\partial T^*}{\partial p^*} \right)_{s^*,0} = \frac{\alpha_{p_0}^* T_0^*}{\rho_0^* c_{p_0}^*} \tag{5.23}$$

in Eq. (5.22) yields

$$p_1^* - p_0^* = \frac{a_0^* \alpha_{p_0}^*}{c_{p_0}^*} \frac{\Omega^*}{2}, \tag{5.24}$$

which, made dimensionless with Eq.s (5.19) and (5.20), reverts to Eq. (5.21).

Figure 5.8 shows the result of the application of the scaling in Eq. (5.21) to the pressure jump data from all of the heat-release-induced simulations, including highly non-isentropic cases. The dimensional or unscaled pressure jumps are plotted in figure 5.8a. The latter are evaluated right after shock formation (i.e. full coalescence of compression waves) but before the onset of decay due to thermoviscous losses. As such, the reported jumps of thermo-fluid-dynamic variables are independent from viscosity and conductivity.

Scaling of the data performed following [112] (figure 5.8b), or using a scaling valid for perfect ideal gases only (figure 5.8c) does not collapse all data across all fluids. In fact, with the former scaling, the reference heat release is $a_0^* p_0^*$, which fails to incorporate the dependence on γ in the scaling parameter, resulting in the correct scaling only of perfect ideal gases with the same value of γ (figure 5.8b). With the latter scaling, in which the reference heat release is $\rho_0^* c_{p_0}^* a_0^* T_0^*$, data from all perfect ideal gases is collapsed (figure 5.8c). Only by replacing T_0^* with $1/\alpha_{p_0}^*$ in this last reference heat release rate, Eq. (5.21) is obtained, yielding full collapse of the numerical data across all fluids and conditions (figure 5.8d), confirming the effectiveness of the proposed scaling.

Experimental data from [88] has also been included (and plotted with a star in figures 5.8, 5.9, and 5.10) starting from the provided dimensionless value of the

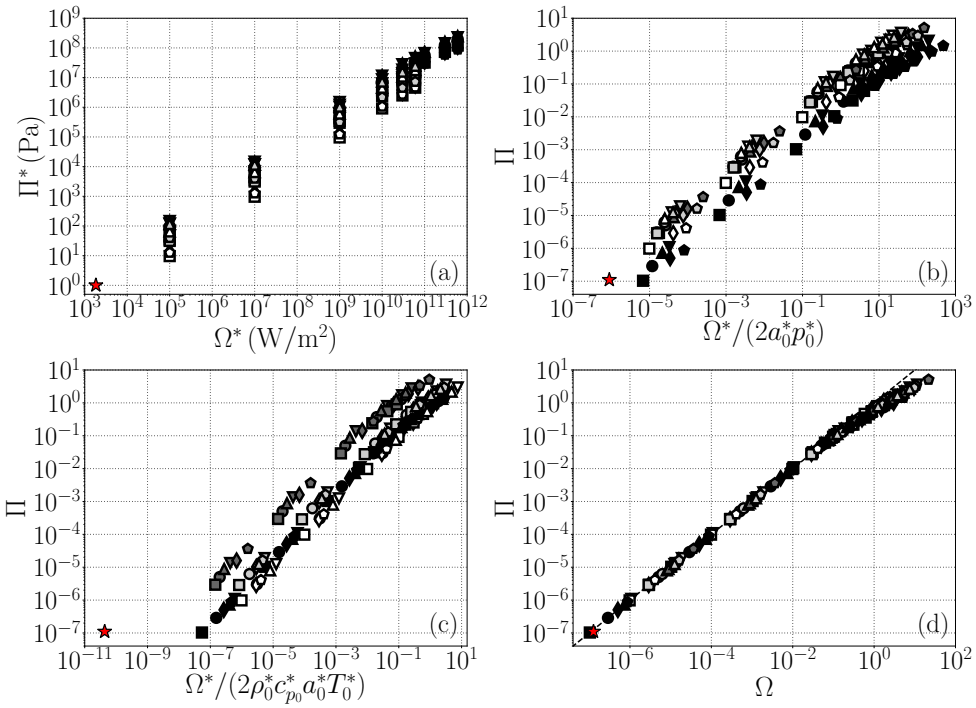

Figure 5.8. Scaling of pressure jumps across heat-release-induced waves. (a) Dimensional pressure jump Π^* versus dimensional heat release rate Ω^*; (b) scaling proposed by [112]; (c) alternative scaling collapsing only IG data; (d) proposed scaling (table 5.3). The isentropic prediction of Eq. (5.21) is shown with the dashed line in (d).

density jump, $\delta\rho^*/\rho_0^* = 1.1 \cdot 10^{-7}$ and of the dimensional planar heat-release rate $\Omega^* = 1830\,\mathrm{W/m^2}$. The dimensionless density jump is converted to a dimensionless pressure jump assuming isentropicity of the transformation ($\delta\rho^*/\rho_0^* = \delta p^*/(\rho_0^* a_0^{*2})$), and the provided heat release rate is made dimensionless via Eq. (5.19).

The parameters listed in table 5.3 allow for full collapse of the numerical and experimental data (figure 5.9). While the present derivation is valid for isentropic waves, it is remarkable that Eq. (5.21) scales approximately well shock jumps up to $\Pi = 5.09$. Such collapse allows the a priori determination, for heat-release-induced waves, of the shock strength Π from the knowledge of dimensionless heat release rate Ω only. The scaling in figure 5.9 allows to clearly observe the departure from

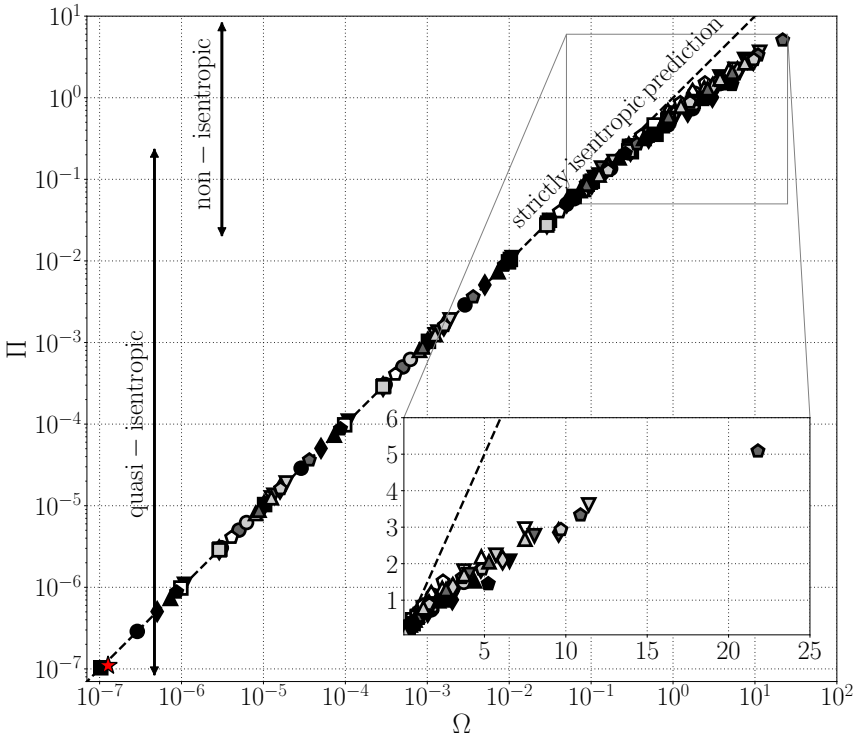

Figure 5.9. Shock strength Π versus dimensionless heat release rate Ω. Star: $T^* - T^*_{cr} = 150$ mK case by [88] with reported $\Pi = 1.1 \cdot 10^{-7}$ and estimated $\Omega = 1.27 \cdot 10^{-7}$. All other symbols: numerical simulation data for all combinations of conditions in tables 5.2.1 and 5.2. The strictly isentropic prediction from Eq. (5.21) is shown with a dashed line.

the isentropic prediction in Eq. (5.21), and to define quasi-isentropic ($\Omega \leq 10^{-1}$) and non-isentropic ($\Omega \geq 10^{-1}$) heat-release-induced regimes. It is noted that Eq. (5.11) implies that all the other dimensionless thermo-fluid-dynamic jumps will be approximately equal to Ω (plots omitted for brevity) in the quasi-isentropic region.

5.3.3 Wave Propagation Mach Number

In this section we derive a suitable normalization to the Rankine-Hugoniot (RH) equations, where pre-compression ("0") and post-compression states ("1") are defined as in figure 5.3, which is the problem formulation of primary interest of this chapter.

Relative mass, momentum, and total enthalpy are conserved across a wave moving at constant speed u_s^*, according to the RH jump conditions,

$$\rho_1^*(u_1^* - u_s^*) = \rho_0^*(u_0^* - u_s^*), \tag{5.25a}$$

$$p_1^* + \rho_1^*(u_1^* - u_s^*)^2 = p_0^* + \rho_0^*(u_0^* - u_s^*)^2, \tag{5.25b}$$

$$h_1^* + (u_1^* - u_s^*)^2/2 = h_0^* + (u_0^* - u_s^*)^2/2, \tag{5.25c}$$

where u^* is the Eulerian flow velocity and $u^* - u_s^*$ is the flow velocity relative to the reference frame moving with the compression wave. Adopting the scaling parameters in table 5.3, we define the five dimensionless jumps

$$\mathcal{R} = \frac{\rho_1^* - \rho_0^*}{\rho_0^*}, \quad \mathcal{U} = \frac{u_1^* - u_0^*}{a_0^*}, \quad M = \frac{u_s^* - u_0^*}{a_0^*}, \quad \mathcal{H} = \frac{h_1^* - h_0^*}{a_0^{*2}}, \quad \Pi = \frac{p_1^* - p_0^*}{\rho_0^* a_0^{*2}}. \tag{5.26}$$

Using the variables in Eq. (5.26), the Rankine-Hugoniot conditions in Eq. (5.25) can be recast in the very concise dimensionless form as:

$$\mathcal{R} = \mathcal{U}/(M - \mathcal{U}), \tag{5.27a}$$

$$\Pi = \mathcal{U}M, \tag{5.27b}$$

$$\mathcal{H} = \Pi - \mathcal{U}^2/2, \tag{5.27c}$$

which leads, after some algebra, to the dimensionless form of the Rayleigh line and of the Hugoniot equation,

$$\Pi = \frac{M^2}{1 + 1/\mathcal{R}}, \tag{5.28a}$$

$$\mathcal{H} = \frac{\Pi}{2}\frac{\mathcal{R} + 2}{\mathcal{R} + 1}. \tag{5.28b}$$

It is important to note that, while in Eq. (5.25) the dimensional downstream variables are explicitly dependent on the base state "0", in the dimensionless forms of Eq. (5.27) and (5.28) the dependency on the state "0", and therefore on the specific fluid under consideration, is formally removed. *A different choice for the enthalpy normalization, such as the commonly adopted $c_{p_0}^* T_0^*$ for ideal gases [112], would have not entailed such result.* This will be useful in the analysis of the behavior of the RH equations for infinite Mach number (§5.4.3).

For strictly isentropic linear waves, Eq. (5.11) gives

$$\Pi = \mathcal{R} = \mathcal{H}, \tag{5.29}$$

hence Eq. (5.28a) yields

$$M = \sqrt{1 + \Pi}. \tag{5.30}$$

Eq. (5.31) indicates that for linear isentropic waves, the wave Mach number departs from unity by an infinitesimal amount. In the limit of $\Pi \to 0$, Eq. (5.28b) is always verified, and Eq. (5.30) yields $M = 1$. Inserting Eq. (5.21) in Eq. (5.30) yields

$$M = \sqrt{1 + \Omega}. \tag{5.31}$$

For the experimental result of [88], corresponding to the star in figure 5.10b, the wave Mach number is estimated as $M = 1 + 6.343 \cdot 10^{-8}$.

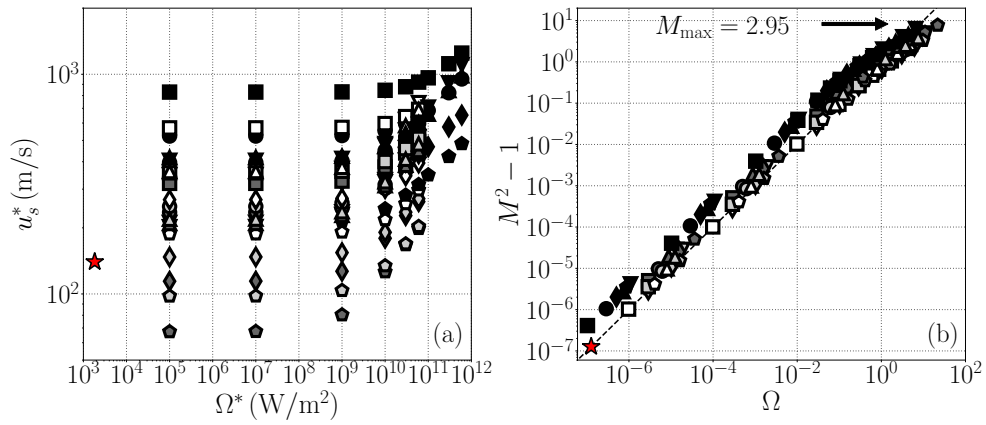

Figure 5.10. Heat-release-induced dimensional wave speed u_s^* versus dimensional heat release rate Ω^* (a); (b) wave Mach number squared minus one, $M^2 - 1$, versus dimensionless heat release rate, Ω. The dashed line in (b) is the isentropic prediction of Eq. (5.31). Star: $T^* - T_{cr}^* = 150$ mK case by [88] with estimated Mach number $M = 1 + 6.343 \cdot 10^{-8}$.

The dimensional wave speed, u_s^*, has been extracted for each of the heat-release-induced numerical simulations and plotted in figure 5.10a. Each wave speed is obtained with a tracking algorithm that follows in time the location of the maximum

pressure gradient across the wave. The wave speed is divided by the speed of sound of the initial condition yielding the Mach number, plotted in figure 5.10b. Firstly, figure 5.10b shows that, for the same dimensionless heat release rate, fluids in pseudo-liquid conditions manifest the highest wave Mach numbers, followed by pseudo-boiling fluids, pseudo gases and perfect ideal gases. The departure of M^2 from one increases linearly with the dimensionless heat release rate Ω, as also pointed out by Eq. (5.31), which has the benefit of providing a first order estimate for a generic fluid in a generic condition. In order to accurately quantify this departure as a function of the heat release rate, the fully predictive modeling procedure in §5.4 will be employed.

Figures 5.9 and 5.10b contain the entirety of the data set and demonstrate the effectiveness of a straightforward application of the isentropic dimensionless scaling to non-isentropic data. Figure 5.9 enables us to pick $\Pi = 10^{-1}$ as the boundary between quasi-isentropic and non-isentropic regimes. In the latter, data still follow a fluid- and state-specific departure from isentropic predictions (see inset in figure 5.9), creating the need for a fully predictive model valid for a generic fluid and high-amplitude waves, derived in §5.4.

5.3.4 Solution of the Rankine-Hugoniot Equations

In the general case of non-isentropic waves, both Eq. (5.25) and Eq. (5.27) provide three nonlinear relations between the upstream and downstream states of the wave. In order to obtain additional relationships (e.g. between Π and $\mathcal{R}$, Π and $\mathcal{U}$, or Π and M), an equation of state (EoS), which adds an additional condition to the three imposed by the RH relations, has to be used. In the case of the perfect ideal gas, a relation of the form $h^* = h^*(\rho^*, p^*, \gamma)$, can be written explicitly, both for state "0" and "1" (see figure 5.3), without adding any other unknowns (being $\gamma_1 = \gamma_0 = \gamma$). This allows to write

$$h_1^* - h_0^* = \frac{\gamma}{\gamma - 1}\left(\frac{p_1^*}{\rho_1^*} - \frac{p_0^*}{\rho_0^*}\right), \tag{5.32}$$

and its dimensionless counterpart, $\mathcal{H} = \mathcal{H}(\mathcal{R}, \Pi, \gamma)$ as well,

$$\mathcal{H} = \frac{1}{\gamma - 1}\left(\frac{\gamma\Pi - \mathcal{R}}{\mathcal{R} + 1}\right), \tag{5.33}$$

and with it all the other well known relationships between thermo-fluid-dynamic jumps as a function of (γ, M). Eq. (5.33) shows that, for a perfect ideal gas, the EoS adds the parameter γ to the RH equations, introducing the dependence on the fluid. This fact is expected since, for the general case of non-isentropic waves, two thermodynamic degrees of freedom are present.

If the fluid is modeled with a more complicated EoS, writing explicitly the aforementioned relationships with full predictive power (assign a Mach number M and obtain Π, for example) is rarely possible or very complicated. Indeed, in the case of the PR EoS, only explicit expressions of the type $p^* = p^*(\rho^*, T^*)$ and $h^* = h^*(\rho^*, T^*)$ are available.

Therefore, Eq. (5.25) with the EoS can be expressed as a system of four equations in the four independent unknown variables $\rho_1^*, T_1^*, u_1^*, u_s^*$, which can be solved for numerically. In particular, we consider the system of equations composed by the EoS ($\mathcal{H} = f(\mathcal{R}, \Pi)$) and the RH (Eq. (5.27)), and perform an iterative method on the vector $(\Pi, \mathcal{R}, \mathcal{U}, \mathcal{H})$, for an assigned Mach number M, with a root finding algorithm, obtaining eventually the solution of the system of equations.

All data from the numerical simulations have been checked against such solution, showing that both quasi-isentropic and non-isentropic shock strengths and wave Mach numbers are trustworthy (figure 5.11).

The solution of Eq. (5.27) allows to obtain all dimensionless jumps as a function of the Mach number M. With the objective to emulate the explicit and predictive relationships available for perfect ideal gases, we define the dimensionless thermodynamic functional ψ_{AB}, function of two thermodynamic states A and B ($\psi_{AB} = \psi_{AB}(\rho_A, \rho_B, p_A, p_B)$), as follows:

$$h_B^* - h_A^* = \frac{\widetilde{\gamma}_A}{\widetilde{\gamma}_A - \psi_{AB}}\left(\frac{p_B^*}{\rho_B^*} - \frac{p_A^*}{\rho_A^*}\right), \tag{5.34}$$

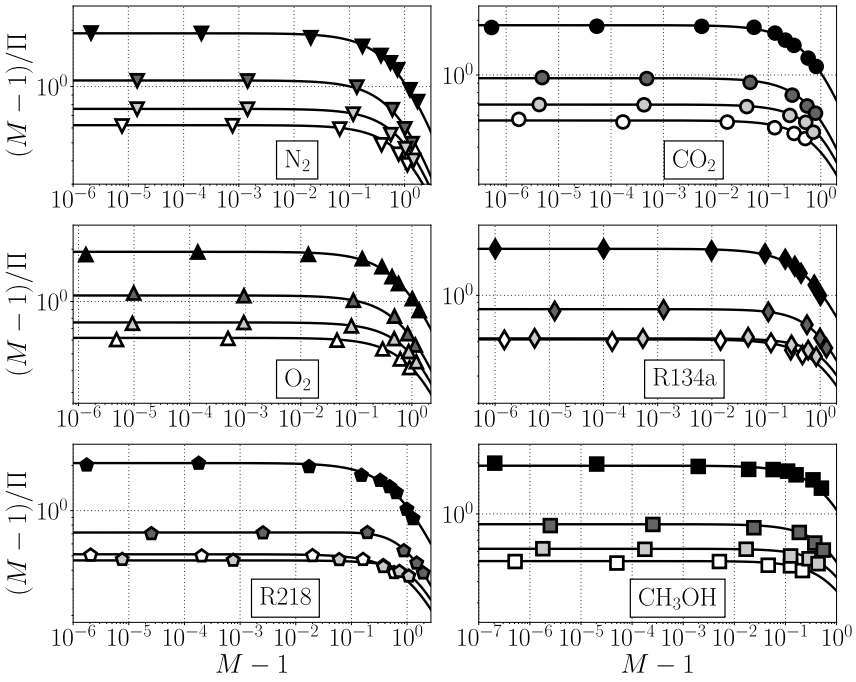

Figure 5.11. Fluid-by-fluid verification of heat-release-induced data: numerical computations (symbols) and solution of the Rankine-Hugoniot jump conditions (solid lines).

where $\psi_{AB} = 1$ for a perfect ideal gas (for any given A and B) and $\widetilde{\gamma} = \rho^* a^{*2}/p^*$ is the isentropic exponent. Applying the definition in Eq. (5.34) to the downstream and upstream states of the compression wave, ("1" and "0", respectively, see figure 5.3), yields

$$h_1^* - h_0^* = \frac{\widetilde{\gamma}_0}{\widetilde{\gamma}_0 - \psi_{01}} \left(\frac{p_1^*}{\rho_1^*} - \frac{p_0^*}{\rho_0^*} \right). \tag{5.35}$$

Eq. (5.35) allows to retain the structure of the ideal gas relationships (for a perfect ideal gas $\psi_{01} = 1$ and $\widetilde{\gamma}_0 = \gamma$, returning to Eq. (5.32)). Eq. (5.35) can be recast in dimensionless form as

$$\mathcal{H} = \frac{1}{\widetilde{\gamma}_0 - \psi_{01}} \left(\frac{\widetilde{\gamma}_0 \Pi - \mathcal{R}}{\mathcal{R} + 1} \right), \tag{5.36}$$

where we see that ψ_{01} is akin to a dimensionless jump. Eq. (5.36), if substituted in Eq. (5.28b), allows to get a relation between Π and $\mathcal{R}$,

$$\mathcal{R} = \frac{2\psi_{01}}{2/\Pi + \widetilde{\gamma}_0 - \psi_{01}}. \tag{5.37}$$

Eq. (5.37), inserted in Eq. (5.28a), yields a relation between M and Π,

$$\psi_{01} M^2 - 1 = \Pi \frac{\widetilde{\gamma}_0 + \psi_{01}}{2}. \tag{5.38}$$

Eq. (5.38), combined with Eq. (5.27b), yields a relation between Π and $\mathcal{U}$,

$$\mathcal{U} = \frac{\sqrt{2\psi_{01}}\Pi}{\sqrt{\Pi(\widetilde{\gamma}_0 + \psi_{01}) + 2}}, \tag{5.39}$$

where $\mathcal{U}$ is assumed positive. Eq. (5.39) reverts to Eq. (38) of [112], valid for a perfect ideal gas ($\psi_{01} = 1$ and $\widetilde{\gamma}_0 = \gamma$).

5.4 Modeling of Heat-Release-Induced Shock Waves

The goal of this section is to gain insight into the structure of the flow field and to derive a fully predictive model for the non-isentropic regime for a generic compressible fluid. This is achieved by reformulating and extending the model exploited by [112] to a generic EoS or fluid.

5.4.1 Global Mass and Energy Balance

We hereafter use the heat-release-induced flow field in R-134a, shown in figure 5.12, as a representative case to guide our discussions. The shocks, propagating to the right with speed u_s^* (as indicated by the solid lines passing through them), are identifiable as sharp perturbations of all thermo-fluid-dynamic quantities. By inspecting the dimensionless density variation profiles ($\delta\rho$), a smeared contact discontinuity (c.d.) is found moving at the shock-induced Eulerian velocity u_1^*. Across the c.d., pressure and velocity do not change, but density and total energy present discontinuities from a post-shock state to a zone at increasingly lower density, where heat is continuously

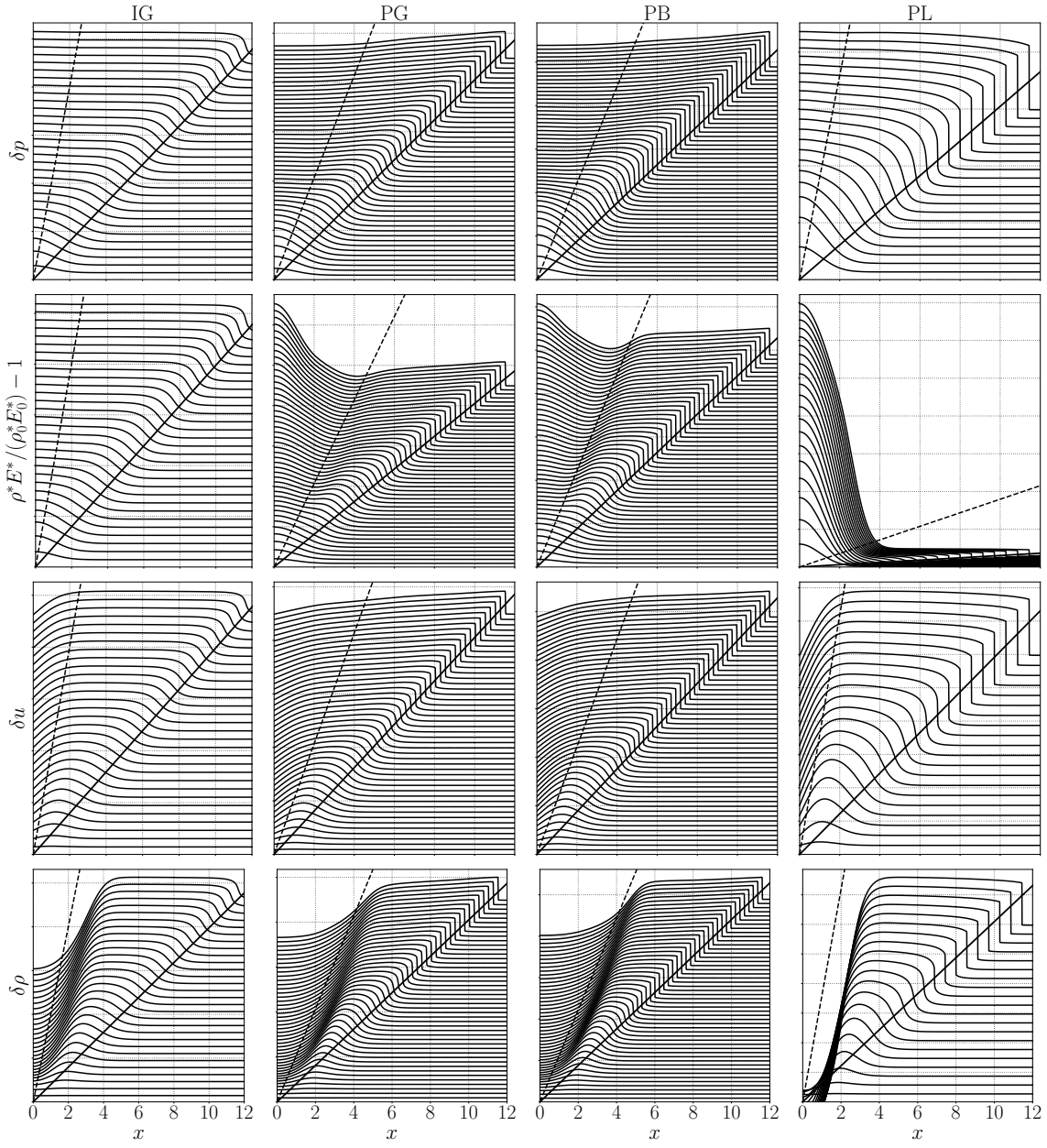

Figure 5.12. Rows: dimensionless perturbations of pressure, total energy, velocity, and density in R-134a plotted versus the dimensionless space coordinate $x = x^*/\ell^*$ and vertically shifted by arbitrary units to show temporal evolution. IG, PG, PB: $\Omega^* = 1 \cdot 10^{10}$ W/m^2; PL: $\Omega^* = 6 \cdot 10^{10}$ W/m^2. Similar behavior is found for the other fluids and conditions (not shown). Dashed lines: fireball edge velocity ($u_1^* = a_0^* \Pi / M$); solid line: shock velocity ($u_s^* = a_0^* M$).

being injected, referred to as the fireball. Figure 5.13a shows a qualitative schematic of the flow.

For a perfect ideal gas (IG, first column of figure 5.12), the pressure and total energy profiles downstream the shock wave, and also inside the fireball, are approximately flat for all times and their values are set by the shock jump. In fact, for IG, $\rho^* e^* = p^*/(\gamma - 1)$, linking pressure and internal energy by a proportionality constant. This is one of the key assumptions made by [112] in deriving his predictive model for heat-release-induced waves in ideal gases, which is discussed later in Eq. (5.47).

For a real fluid, instead, the relationship between pressure and internal energy is highly nonlinear; as such the two variables show different spatiotemporal evolutions. Moreover, their spatial profiles between the shock wave and the fireball edge are not flat in space. Finally, in the fireball, total energy varies significantly with time and space, especially in PL conditions, and pressure is not constant.

To facilitate the following analytical derivations, the (mirrored) infinite extension of the semi-infinite problem in figure 5.3 is considered. The governing equations of mass, momentum, and total energy, Eq.s (5.1) and (5.2), are integrated on the real axis, yielding

$$\begin{cases} \dfrac{\partial}{\partial t^*}\left(\displaystyle\int_{-\infty}^{\infty} \rho^* dx^*\right) + \displaystyle\int_{-\infty}^{\infty} \frac{\partial \rho^* u^*}{\partial x^*} dx^* = 0, \\ \dfrac{\partial}{\partial t^*}\left(\displaystyle\int_{-\infty}^{\infty} \rho^* u^* dx^*\right) + \displaystyle\int_{-\infty}^{\infty} \frac{\partial (\rho^* u^{*2} + p^*)}{\partial x^*} dx^* = 0, \\ \dfrac{\partial}{\partial t^*}\left(\displaystyle\int_{-\infty}^{\infty} \rho^* E^* dx^*\right) + \displaystyle\int_{-\infty}^{\infty} \frac{\partial (\rho^* u^* E^* + p^* u^* - u^* \tau^* + q^*)}{\partial x^*} dx^* = \Omega^*, \end{cases} \tag{5.40}$$

where the definition of $\dot{Q}^*$ in Eq. (5.4) has been used, and the time derivative has been taken out of the spatial integral. Exploiting the initial state properties (between $\pm u_s^* t^*$ and $\pm\infty$, $u_0^* = 0$, and T_0^*, p_0^* are constants) yields

$$\begin{cases} \displaystyle\int_{-u_s^* t^*}^{u_s^* t^*} \rho^* dx^* = 2\rho_0^* u_s^* t^*, \\ \displaystyle\int_{-u_s^* t^*}^{u_s^* t^*} \rho^* u^* dx^* = 0, \\ \displaystyle\int_{-u_s^* t^*}^{u_s^* t^*} \rho^* E^* dx^* = 2\rho_0^* e_0^* u_s^* t^* + \Omega^* t^*, \end{cases} \tag{5.41}$$

where we integrated in time the first terms on the left hand sides. Eq. (5.41) identifies three integral conservation laws, namely: the total mass between shocks is equal to the initial value $2\rho_0^* u_s^* t^*$; the flow rate induced by one shock is balanced by the other to zero (initial value, since $u_0^* = 0$), and the total energy increases linearly with time because of heat input. If the profiles of density and total energy are assumed to be symmetric with respect to the plane $x^* = 0$, Eq. (5.41) becomes

$$\begin{cases} \dfrac{1}{t^*}\displaystyle\int_0^{u_s^* t^*} \rho^* dx^* = \rho_0^* u_s^*, \\ \dfrac{1}{t^*}\displaystyle\int_0^{u_s^* t^*} \rho^* E^* dx^* = \rho_0^* e_0^* u_s^* + \Omega^*/2, \end{cases} \tag{5.42}$$

and only $x^* \geq 0$ is analyzed. With this assumption, the second of Eq. (5.41) simply states that the profile of $\rho^* u^*$ is antisymmetric with respect to the plane $x^* = 0$, hence is ignored from Eq. (5.42) on. For any given time, Eq. (5.42) can be written as

$$\begin{cases} \displaystyle\int_0^M \rho^* d\xi = \rho_0^* M, \\ \displaystyle\int_0^M \rho^* E^* d\xi = \rho_0^* e_0^* M + \Omega^*/(2a_0^*), \end{cases} \tag{5.43}$$

by using the definition of Mach number in Eq. (5.26) and the dimensionless coordinate $\xi = x^*/(a_0^* t^*)$. From visual inspection of figure 5.12, the simplified scenario of figure 5.13b is assumed, hence Eq. (5.43) can be further developed as

$$\begin{cases} \rho_3^* \mathcal{U} + \displaystyle\int_{\mathcal{U}}^M \rho_2^* d\xi = \rho_0^* M, \\ \rho_3^* E_3^* \mathcal{U} + \displaystyle\int_{\mathcal{U}}^M \rho_2^* E_2^* d\xi = \rho_0^* e_0^* M + \Omega^*/(2a_0^*), \end{cases} \tag{5.44}$$

where we used $\mathcal{U} = (u_1^* - u_0^*)/a_0^*$ (Eq. (5.26)). Only a suitable choice of $\rho_2^*(\xi)$ in Eq. (5.44) is left for the prediction of heat-release-induced wave strength. We choose a linear functional form for $\rho_2^*(\xi)$,

$$\rho_2^*(\xi) = \rho_3^* + \frac{\rho_1^* - \rho_3^*}{M - \mathcal{U}}(\xi - U), \tag{5.45}$$

which inserted in the first of Eq. (5.44) yields the value of the fireball's density (figure 5.13b),

$$\rho_3^* = \rho_1^* \frac{M - \mathcal{U}}{M + \mathcal{U}}, \tag{5.46}$$

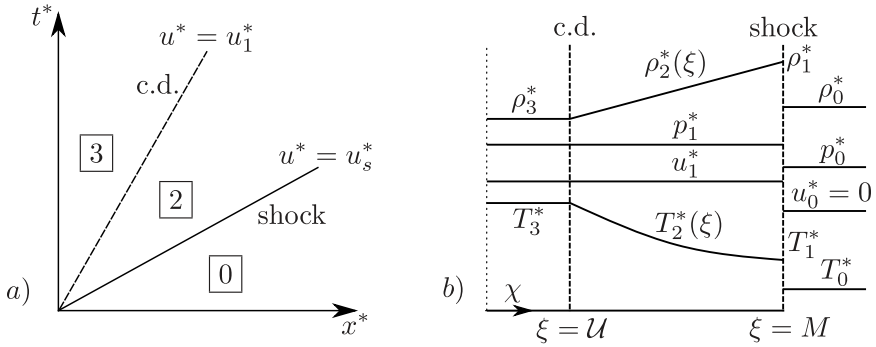

Figure 5.13. Schematics of heat-release-induced right-travelling shock wave and contact discontinuity (c.d.). (a) Modeling of the flow fields of figure 5.12; (b) profiles used in Eq.(5.44). The temperature profile T_2^*, sketched qualitatively, is obtained with the EoS (Eq. (2.1)) as $T^*(\rho_2^*, p_1^*)$, where ρ_2^* is obtained from Eq. (5.45).

which essentially provides a jump condition across the contact discontinuity. A different choice for $\rho_2^*(\xi)$ in Eq. (5.45) would change Eq. (5.46), but not the overall mass balance imposed by the first of Eq. (5.44).

The equations in (5.44) are solved with the following procedure: first, for a given Mach number M, treated as an input, the RH equations are solved (appendix 5.3.4), providing all the other shock quantities; then, ρ_3^* is computed from Eq. (5.46), and $e_3^* = e^*(\rho_3^*, p_1^*)$ is computed with the equation of state; finally, the integral in the second of Eq. (5.44) is computed (with the knowledge of $\rho_2^*(\xi)$ in Eq. (5.45) and p_1^*), providing a value for Ω^*.

[112] proposed a predictive model for heat-release-induced shock intensity for perfect ideal gases, by assuming $\rho_2^*(\xi) = \rho_1^*$. With this choice, Eq. (5.44) becomes

$$\begin{cases} \rho_3^* = 0, \\ p_1^* u_1^* = (\gamma - 1)\Omega^*/(2\gamma), \end{cases} \tag{5.47}$$

where $\rho_2^* E_2^* = p_1^*/(\gamma - 1) + \rho_1 u_1^{*2}/2$ and the RH equations (Eq. (5.25)) have been used. Given the fixed pressure of state "2", its total energy is equal to the one just downstream the shock wave, consistently with the flow field observed in the IG column

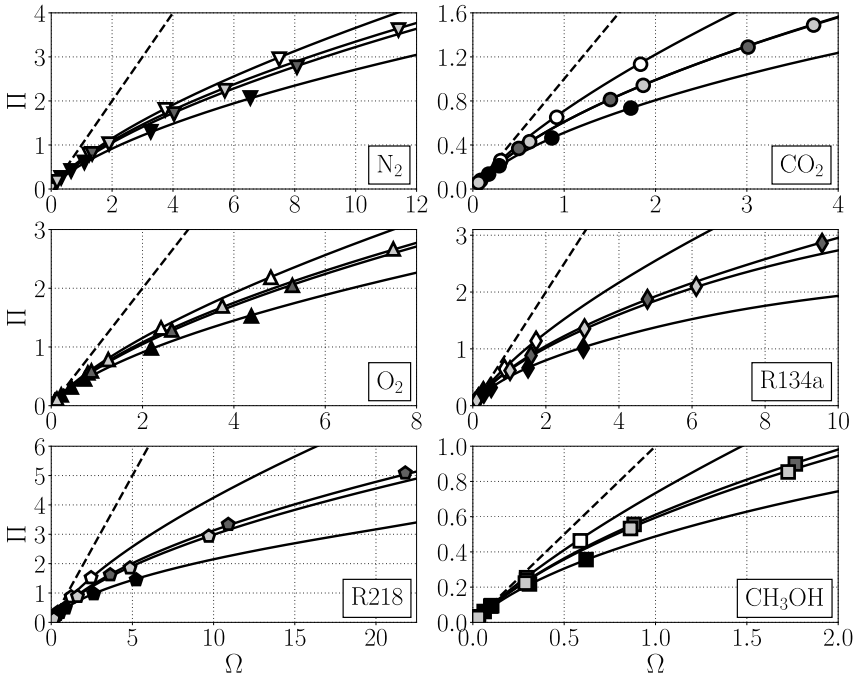

Figure 5.14. Fluid-by-fluid shock strengths for high heat release rates showing deviation from the isentropic prediction of Eq. (5.21) (dashed line): numerical computations (symbols) and results from modeling strategy (solid lines) based on integral mass and energy conservation (Eq. (5.44), figure 5.13). IG data (white-filled symbols) lay on the curve defined by Eq. (5.48).

of figure 5.12. The second of Eq. (5.47), which coincides with Eq. (34) of [112], can be made dimensionless using Eq.s (5.26) and (5.39),

$$\Omega = \frac{\sqrt{2}\Pi(\gamma\Pi + 1)}{\sqrt{\Pi(\gamma + 1) + 2}}, \tag{5.48}$$

which is the exact parametrization derived in Eq. (39) of [112], recast following the normalization and symbology used in this chapter (see Eq.s (5.19) and (5.20)). For $\Pi \ll 1$, Eq. (5.48) reverts to Eq. (5.21), removing the dependency from the ratio of specific heats γ, consistently with the single degree of thermodynamic freedom intrinsic to isentropic waves. While the model proposed by [112] satisfies the conservation laws in differential and integral forms, and allows to obtain a prediction for

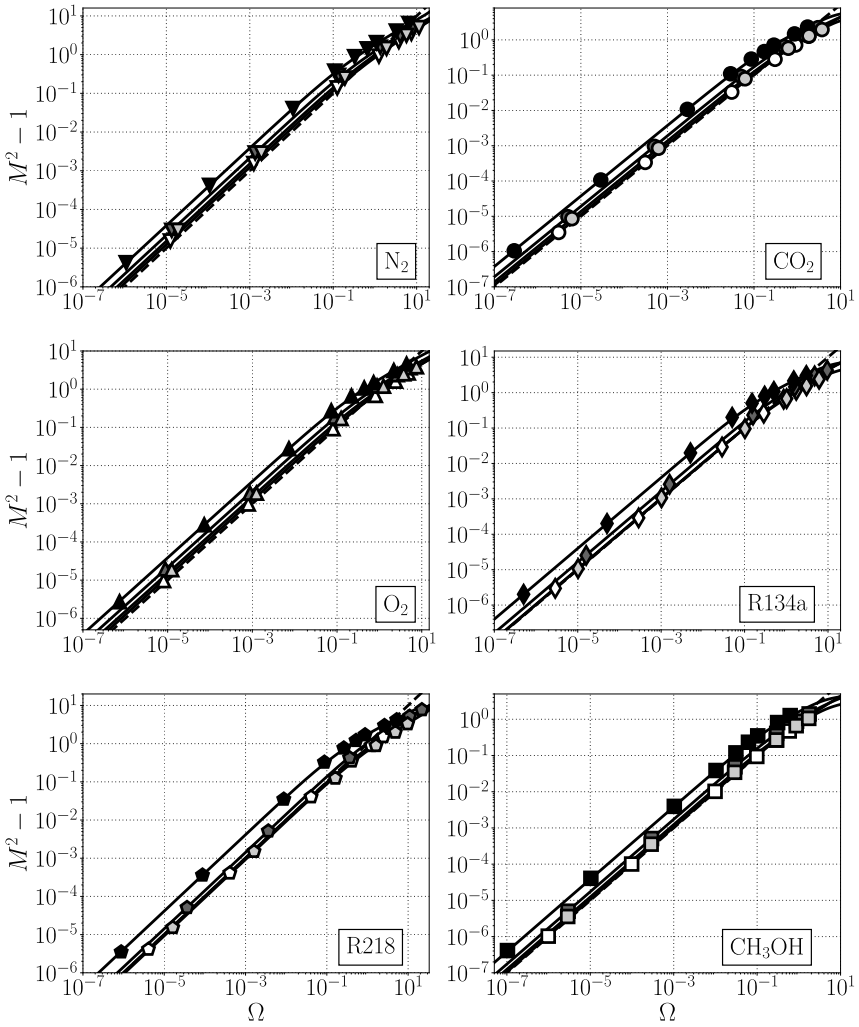

Figure 5.15. Fluid-by-fluid Mach numbers versus dimensionless heat release rate Ω. Dashed line: isentropic prediction of Eq. (5.31); symbols: numerical computations; solid lines: results from modeling strategy based on integral mass and energy conservation (Eq. (5.44), figure 5.13).

heat-release-induced shock strength, it does not apply to a generic fluid: the problem is in Chu's assumption of $\rho_3^* = 0$, which does not allow to obtain a value for $\rho_3^* e_3^*$, needed in the evaluation of the second of Eq. (5.44). In fact, for the PR EoS, $\rho^* e^*$ can diverge for $\rho^* \to 0$; instead, for a perfect ideal gas, $\rho^* e^* = p^*/(\gamma - 1)$ is independent of ρ^*. Anyways, for a perfect ideal gas, inserting Eq. (5.46) in the second of Eq.

(5.44) yields again Eq. (5.47) and Chu's results become a subset of our more general modeling procedure.

Applying the proposed predictive model for heat-release-induced waves to all the initial conditions in table 5.2.1 allows to obtain the solid lines shown in figure 5.14 and 5.15 matching the Navier-Stokes data. The model correctly captures the departure of heat-release-induced wave amplitudes from the isentropic prediction in Eq. (5.21) for $\Omega > 10^{-1}$ (figure 5.9). More specifically, the data follows a fluid- and state-specific law due to the second degree of thermodynamic freedom associated with the non-reversible entropy generation occurring across the heat-release-induced compression. Such trend is accurately predicted by the proposed model, which in turn confirms the validity of the reported heat-release-induced shock strengths. Furthermore, the modeling strategy is able to correctly capture the departure from unity of the wave Mach number for quasi-isentropic waves (figure 5.15), in addition to establishing good matching between data and model results in the non-isentropic region for it as well.

5.4.2 Efficiency of Thermal to Mechanical Power Conversion

Figure 5.14 shows that, for non-isentropic waves, the ratio of the dimensionless pressure jump to dimensionless heat release rate, Π/Ω, is maximum for perfect ideal gases and minimum for fluids in pseudo-liquid conditions; in all cases, it is always upper bounded by the isentropic prediction $\Pi = \Omega$. This decrease of Π/Ω from IG to PL conditions can be explained by inspecting figure 5.12. For IG conditions, the fireball's total energy does not increase significantly in time, implying that all of the thermal power is sustaining the shock strength. On the other hand, for real fluids, the nonlinear relationships between thermodynamic variables allow internal energy to change if pressure is held constant in the fireball. For PL conditions, in particular, a significant part of the injected power is retained by the fireball, hence reducing the amount of mechanical power carried by the shock.

However, even if the ratio Π/Ω is the highest for fluids in IG conditions, the same is not strictly true for the efficiency of thermal to mechanical power conversion, which has a different mathematical expression. In fact, a quantitative metric for the latter can be obtained by dividing the mechanical power carried by the shocks, $2(p_1^* - p_0^*)u_1^*$, by the total heat power input, Ω^*,

$$\eta = \frac{(p_1^* - p_0^*)u_1^*}{\Omega^*/2}. \tag{5.49}$$

The right-hand side of Eq. (5.49) can be recast with the parameters in table 5.3 and Eq. (5.27b), yielding

$$\eta = \frac{\Pi^2}{\varphi_0 \Omega M}, \tag{5.50}$$

where

$$\varphi = \frac{\alpha_p^* T^*}{\gamma - 1}, \tag{5.51}$$

which is defined by [27] as the ratio between the "heat parameter" $\alpha_p^* T^*$ to the "work parameter" $\gamma - 1$ in the context of thermoacoustic energy conversion. With the currently adopted normalization (see table 5.3), $\varphi = T^*/\delta T_{ref}^* = T$, and, for a perfect ideal gas, $\varphi = 1/(\gamma - 1)$.

The efficiency computed with the data extracted from the numerical simulations is compared in figure 5.16 to the theoretical efficiency (computed with modeling strategy outlined in §5.4.1). For quasi-isentropic waves, the efficiency in Eq. (5.50) is approximately given by $\eta = \Pi/\varphi_0$, and is the highest for fluids in PL conditions, contrary to what the ratio Π/Ω may suggest, followed by PB, PG, and then IG conditions. On the other hand, when the dimensionless heat release rate increases and the waves are non-isentropic, the efficiency η of perfect ideal gases grows, until it becomes the highest among all initial conditions.

The next section reveals how the ratio Π/Ω and the efficiency of thermal to mechanical power conversion behave for extremely high values of heat release rate.

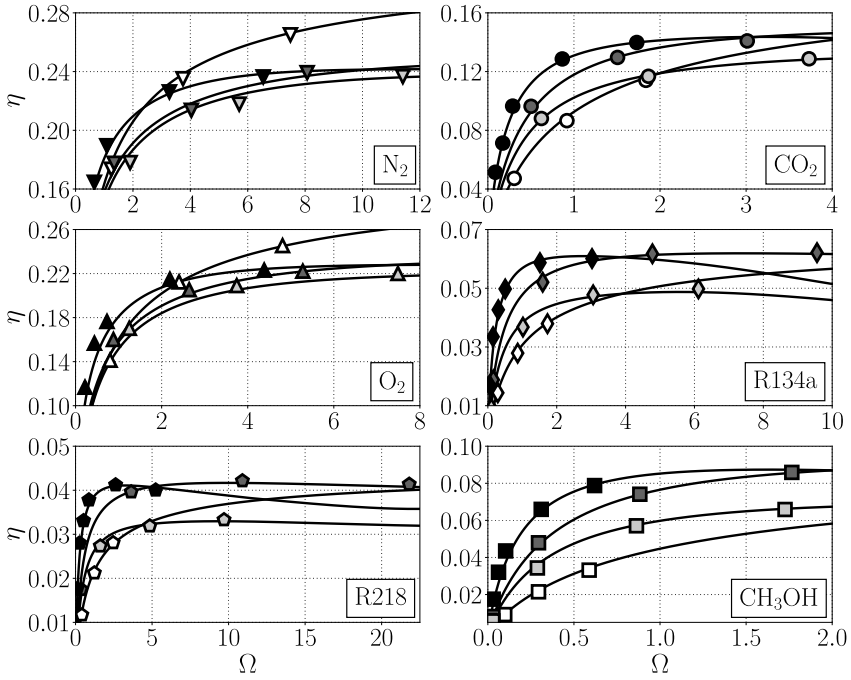

Figure 5.16. Fluid-by-fluid shock thermal-to-mechanical energy efficiency (Eq. (5.50)) for non-isentropic heat-released-induced compression waves: numerical computations (symbols) and results from the solution of the Rankine-Hugoniot equations (solid lines).

5.4.3 Asymptotic Limit of Infinite Shock Strength

In the limit of $\Omega^* \to \infty$, both the perfect ideal gas and the PR EoS cease to be physically representative of a real fluid. Nonetheless, it is of theoretical interest to investigate the asymptotic behavior of the RH equations and of heat-release-induced efficiencies.

For very high dimensionless heat release rate $\Omega \gg 1$ and, thus, shock strength $\Pi \gg 1$, Eq. (5.48), valid for a perfect ideal gas, reverts to the two-thirds law proposed in Eq. (40) of [112], which can be recast as

$$\Pi = \left(\frac{\gamma+1}{2}\right)^{1/3} \left(\frac{\Omega}{\gamma}\right)^{2/3}. \tag{5.52}$$

In order to investigate the asymptotic behavior of a generic fluid, the Rankine-Hugoniot equations (Eq. (5.27)) and the EoS are solved numerically (see appendix 5.3.4) for high-intensity shock waves, for R134a in PL conditions, and explicitly for R134a in IG conditions (figure 5.17). For low values of Mach number (quasi-isentropic

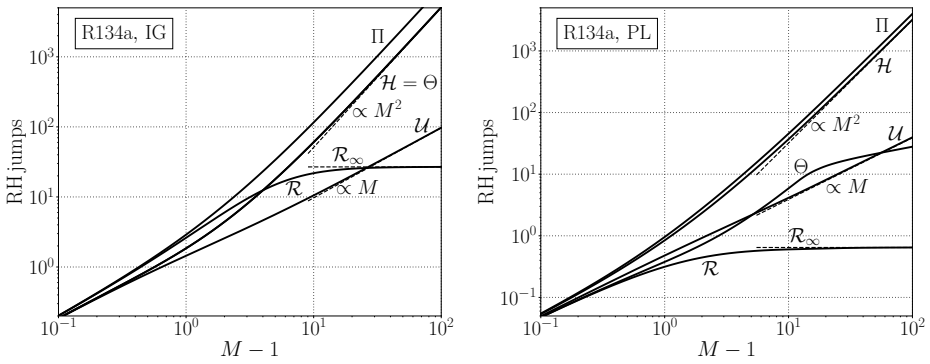

Figure 5.17. Results from the solution of the Rankine-Hugoniot equations combined with the EoS (see appendix 5.3.4), for high Mach numbers, for R-134a in IG and PL conditions. Dashed lines represent the prediction of Eq. (5.53), valid for $M \to \infty$.

region), all dimensionless jumps match, consistently with Eq. (5.29). For $M \to \infty$, instead, the dimensionless density jump $\mathcal{R}$ reaches a finite limit value, $\mathcal{R}_\infty$. All the other jumps are governed by the RH equations (Eq. (5.27)), which can be written, for $M \to \infty$, as

$$\mathcal{U}_\infty = \frac{M}{1+1/\mathcal{R}_\infty}, \qquad \Pi_\infty = \frac{M^2}{1+1/\mathcal{R}_\infty}, \qquad \mathcal{H}_\infty = M^2 \frac{2/\mathcal{R}_\infty - 1}{2(1+1/\mathcal{R}_\infty)^2}, \tag{5.53}$$

which establish the trends of $\mathcal{U}, \Pi, \mathcal{H}$ visible in figure 5.17. For a perfect ideal gas, Eq. (5.37) for $\Pi \gg 1$ yields $R_\infty = 2/(\gamma-1)$. Therefore, fluids in IG conditions tend to an asymptotic thermal to mechanical power conversion efficiency,

$$\eta = 1 - \frac{1}{\gamma}, \tag{5.54}$$

where we used the second of Eq. (5.53), Eq. (5.52), and Eq. (5.50), with $\varphi_0 = 1/(\gamma-1)$.

The dimensionless temperature jump,

$$\Theta = \frac{T_1^* - T_0^*}{(\gamma_0 - 1)/\alpha_{p_0}^*}, \tag{5.55}$$

where the reference temperature in table 5.3 has been used, is also plotted in figure 5.17. For fluids in IG conditions, $\Theta = \mathcal{H}$ always holds. For real fluids, instead, the EoS in Eq. (2.1) sets the value of temperature from the ones of density and pressure, which are imposed from the RH equations. Since the temperature profile in figure 5.13b governs the global energy balance of Eq. (5.44), this affects the predicted value of Ω for a certain shock strength Π, resulting in the trends shown in figure 5.18a.

For very high values of dimensionless heat release rates, fluids in IG conditions reach the two-thirds law predicted by Eq. (5.52), and the constant thermal to mechanical power conversion efficiency given by Eq. (5.54). For real fluids, instead, the ratio Π/Ω tends to a value lower than the upper bound imposed by fluids in IG conditions, and the efficiency η decreases, eventually reaching values inferior to the ones obtained in the quasi-isentropic region (figure 5.18b).

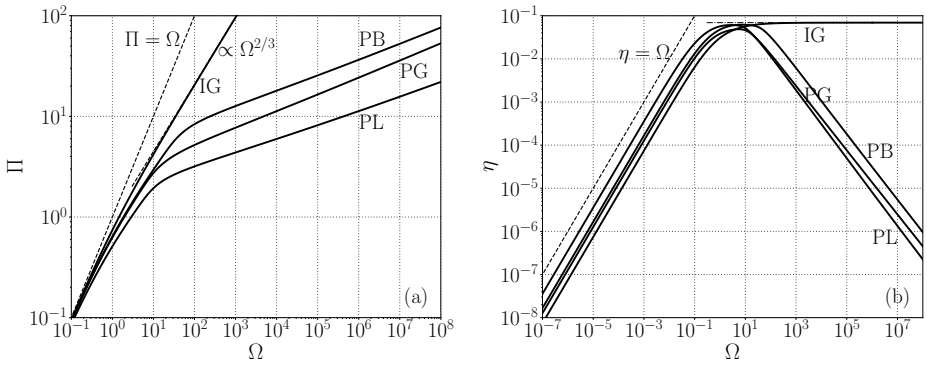

Figure 5.18. Results from the modeling strategy (§5.4.1) for high values of heat release rates, for R-134a in different thermodynamic states. (a) Shock strength Π versus dimensionless heat release rate Ω; (b) efficiency of thermal to mechanical power conversion η (Eq. (5.50)) versus Ω. The isentropic prediction $\Pi = \Omega$ is plotted with a dashed line in (a), and Eq. (5.53), valid for $M \to \infty$ and applicable only to perfect ideal gases, is plotted as a dashed dotted line in (b).

6. CONCLUSIONS

In chapter 3, we have compared the use of a fully conservative approach against a non-conservative one for the simulation of real fluids using a high-order spectral difference method. The first approach consists in solving the compressible Navier-Stokes equations in conservative form and computing the pressure as a derived quantity using an ad-hoc equation of state. This approach is found to yield significant pressure oscillations leading to computational instability when thermodynamic gradients of the flow are too high (e.g., for conditions close to the critical point). Solving instead an evolution equation for pressure is found to eliminate completely the spurious oscillations and thus significantly improves the stability of computations, at the cost of losing the total energy conservation. The benefit of solving the pressure equation instead of total energy in the context of real fluid flows has been demonstrated for a simple 1D entropy wave advection as well as the more stringent 2D buoyancy problem and 3D channel flow computation. Future work will feature a more extensive comparison and validation as well as the assessment of the present methodology for more complex flow problems.

In chapter 4 we have carried out the first Navier-Stokes simulations of a thermoacoustically unstable duct employing carbon dioxide in transcritical conditions inside the stack. We have performed an analysis over a range of 3.615 MPa in base pressures p_0 and 200 K in temperature differences ΔT, considering fluid in pseudo-gaseous, pseudo-boiling, and pseudo-liquid conditions in a computational setup optimized thanks to the linear theory. A grid convergence study has firstly been carried out, showing that the linear theory needs to consider the full eigenvalue $\alpha + i\omega$, rather than just its imaginary part ω, in order to accurately reproduce the growth rates extracted from the Navier-Stokes simulations. This is due to the high ratio α/ω exhibitied by transcritical thermoacoustic instabilities. Secondly, strong real-

fluid effects have been discussed. Indeed, after the fluid inside the stack approaches pseudo-boiling conditions, for a fixed T_{cold}, the frequency of oscillation exhibits a steep drop, while the growth rate, after a small dip for $p_0/p_{cr} = 1.01, 1.05$, increases to positive values. The growth rates exhibit a non-monotone trend with respect to p_0, showing a decrease for p_0 approaching p_{cr} and an optimum at a value of p_0 which increases with the imposed ΔT. Frequencies, instead, show a linear increase with p_0 at all values of ΔT. The eigenmodes of the system also show some peculiar real-fluid effects, for p_0 sufficiently close to p_{cr}. The pressure eigenmode presents its maximum on the right end side of the setup, while the same configuration, if a perfect ideal gas is considered, shows a higher pressure amplitude on the left hand side. Moreover, pressure fluctuations do not show a stationary node, but rather an unsteady one, due to the high ratio α/ω, and, because of this, the entire axial profile of pressure amplitude tends to flatten out. For the same reason, the pressure-velocity phasing smoothly transitions at the average location of the pressure node, assuming there a non-zero value. Furthemore, due to the rapid change in acoustic impedance present at pseudo-boiling conditions, pressure, mass flow rate, and acoustic power change drastically their derivative, as if there was an area change. The acoustic energy budgets are derived from the frequency-domain linear expressions for pressure and flow rate, and are closed, allowing to obtain a consistent value of the growth rate. Terms of the energy budgets indicating production and dissipation are analyzed inside the stack, showing a boost in thermoacoustic production at pseudo-boiling conditions, due to the spike of thermal expansion coefficient, also accompanied by a sharp increase in thermoacoustic dissipation due to the spike of Prandtl number. The acoustic power and total energy flux inside the stack show an increased slope at pseudo-boiling conditions, therefore suggesting that conditions closer to the critical point produce additional power, but also require more heat to be sustained. Data from the linear theory augmented with minor losses, which are tuned to data extracted from the Navier-Stokes simulations, allow for computations of heat-to-mechanical power conversion efficiency, which has a maximum of 0.87 %, obtained for $p_0/p_{cr} = 1.5$ at a ΔT of 120 K. Nevertheless,

the maximum limit cycle pressure oscillations grow monotonically with ΔT and are achieved for $p_0/p_{cr} = 1.01$. An in-depth analysis of the physics of the pseudo-boiling region, for high values of pressure amplitude, reveals concentrated nonlinear effects around it. Indeed, the drop in thermal boundary layer thickness at PB conditions causes the fluid inside the stack pore to lag behind other acoustic parcels, resulting in a nonlinear Lagrangian pressure-volume cycle.

In chapter 5 we have derived the correct set of reference scaling parameters able to achieve collapse of isentropic acoustic waves and heat-release-induced thermodynamic jumps and speed across all homogeneous compressible fluids. The reference temperature and heat release rate are expressed in terms of the isobaric thermal expansion coefficient. Data from 186 highly resolved one-dimensional Navier-Stokes numerical simulations of a variety of supercritical fluids has been adopted to verify the effectiveness of the proposed scaling strategy. The latter has also been successfully applied to one of the experimental results of [88], and has allowed to compute its wave Mach number. Furthermore, the data has been used to aid the extension of the scaling to the non-isentropic regime, where heat-release-induced shock waves have been investigated. Scaling of shock pressure jumps and wave Mach numbers provides their approximate a priori measure with the only knowledge of the dimensionless heat release rate Ω. In order to satisfy the need for a more accurate determination of the intensity and speed of heat-release-induced waves, a fully predictive model based on global mass and energy conservation has been proposed, generalizing the results of [112]. In the heated zone, a different energy pathway from the one imposed by perfect ideal gases has been identified as the thermodynamic bottleneck for transformation of heat to shock intensity, when non-isentropic waves are concerned. In reality, in the quasi-isentropic regime, another measure of heat-to-mechanical energy efficiency is maximum for fluids in pseudo-liquid conditions. Finally, the asymptotic behavior of heat-release-induced wave intensity for infinite Mach number has been shown to differ from the one of perfect ideal gases because of the different trend of the temperature jump, due to the highly nonlinear equation of state. For infinite

shock strength, the efficiency of thermal to mechanical power conversion of real fluids decreases, while the one of perfect ideal gases reaches a constant.

Based on the aforementioned numerical and theoretical knowledge, an experimental prototype of a transcritical thermoacoustic engine was built [79]. Current and future work is devoted to the understanding of its operations and to the design and testing of its second generation.

REFERENCES

REFERENCES

[1] M. Palumbo. *Predicting the onset of thermoacoustic oscillations in supercritical fluids.* Master's thesis, Purdue University, October 2009.

[2] Patrick C. Sweeney, Stephen D. Heister, Steven A. Hunt, Carlo Scalo, and Mario Tindaro Migliorino. System and method for stabilizing transcritical air-to-fuel heat exchange, US Patent Application 15/473,759, 2017.

[3] Steven A. Hunt. *Thermoacoustic Oscillations in Supercritical Fluid Flows.* PhD thesis, Purdue University, 2016.

[4] Heather K. Wiest and Stephen D. Heister. Experimental Study of Gas Turbine Combustion With Elevated Fuel Temperatures. *Journal of Engineering for Gas Turbines and Power*, 136(12):121507–121507, 07 2014.

[5] W. S. Hines. Pressure oscillations associated with heat transfer to hydrocarbon fluids at supercritical pressures and temperatures. *ARS Journal*, 32(3):361–366, 1962.

[6] L.E. Faith, G.H. Ackerman, and H.T. Henderson. Heat Sink Capability of Jet A Fuel: Heat Transfer and Coking Studies. Technical report, Shell Development Company, 1971.

[7] Brad Hitch and Michael Karpuk. *Enhancement of heat transfer and elimination of flow oscillations in supercritical fuels.* American Institute of Aeronautics and Astronautics, 1998.

[8] Diane Linne, Michael Meyer, Tim Edwards, and David Eitman. *Evaluation of heat transfer and thermal stability of supercritical JP-7 fuel.* American Institute of Aeronautics and Astronautics, 1997.

[9] Diane Linne, Michael Meyer, Donald Braun, and Dennis Keller. *Investigation of instabilities and heat transfer phenomena in supercritical fuels at high heat flux and temperatures.* American Institute of Aeronautics and Astronautics, 2000.

[10] Neal R. Herring and Stephen D. Heister. Review of the development of compact, high performance heat exchangers for gas turbine applications. In *ASME International Mechanical Engineering Congress and Exposition*, volume Heat Transfer, Volume 2, pages 467–476, 2006.

[11] Steven Hunt and Stephen D. Heister. *Thermoacoustic Oscillations in Supercritical Fuel Flows.* American Institute of Aeronautics and Astronautics, 2017/07/17 2014.

[12] C. Scalo, S. K. Lele, and L. Hesselink. Linear and Nonlinear Modeling of a Theoretical Traveling-Wave Thermoacoustic Heat Engine. *J. Fluid Mech.*, 766:368 – 404, 2015.

[13] M. E. Fisher and B. Widom. Decay of correlations in linear systems. *J. Chem. Phys.*, 50(20):3756–3772, 1969.

[14] D. T. Banuti. Crossing the Widom-line – Supercritical pseudo-boiling. *J. Supercritical Fluids*, 98:12–16, 2015.

[15] S. C. Tucker. Solvent density inhomogeneities in supercritical fluids. *Chem. Rev.*, 99:391–418, 1999.

[16] F. Gorelli, M. Santoro, T. Scopigno, M. Krisch, and G. Ruocco. Liquid-like behavior of supercritical fluids. *Phys. Rev. Lett.*, 97(24):245702, 2006.

[17] G. G. Simeoni, T. Bryk, F. A. Gorelli, M. Krisch, G. Ruocco, M. Santoro, and T. Scopigno. The Widom line as the crossover between liquid-like and gas-like behaviour in supercritical fluids. *Nature Physics*, 6:503–507, 2010.

[18] D.-Y. Peng and D. B. Robinson. A new two-constant equation of state. *Ind. Eng. Chem. Fundam.*, 15(1):59–64, 1976.

[19] T.-H. Chung, M. Ajlan, L. L. Lee, and K. E. Starling. Generalized multiparameter correlation for nonpolar and polar fluid transport properties. *Ind. Eng. Chem. Res.*, 27(4):671–679, 1988.

[20] B. E. Poling, J. M. Prausnitz, and J. P. O'Connell. *The properties of gases and liquids.* McGraw-Hill, 2001.

[21] Richard S. Miller, Kenneth G. Harstad, and Josette Bellan. Direct numerical simulations of supercritical fluid mixing layers applied to heptane-nitrogen. *J. Fluid Mech.*, 436:1–39, 6 2001.

[22] E. W. Lemmon, M. O. McLinden, and D. G. Friend. *Thermophysical properties of fluid systems, NIST chemistry webbook, NIST standard reference database.* Number 69. National Institute of Standards and Technology, Gaithersburg MD, 20899, 2016.

[23] Kurt Frey, Michael Modell, and Jefferson Tester. Density-and-temperature-dependent volume translation for the {SRK} eos: 1. pure fluids. *Fluid Phase Equilibria*, 279(1):56 – 63, 2009.

[24] Nikolaus Rott. Damped and Thermally Driven Acoustic Oscillations in Wide and Narrow Tubes. *Z. Angew. Math. Phys.*, 20:230 – 243, 1969.

[25] Jeffrey Lin, Carlo Scalo, and Lambertus Hesselink. High-fidelity simulation of a standing-wave thermoacoustic–piezoelectric engine. *J. Fluid Mech.*, 808:19–60, Dec 2016.

[26] Prateek Gupta, Guido Lodato, and Carlo Scalo. Spectral energy cascade in thermoacoustic shock waves. *J. Fluid Mech.*, 831:358–393, 2017.

[27] G. W. Swift, A. Migliori, T. Hofler, and John Wheatley. Theory and calculations for an intrinsically irreversible acoustic prime mover using liquid sodium as primary working fluid. *The Journal of the Acoustical Society of America*, 78(2):767–781, 1985.

[28] Mario Tindaro Migliorino, Prateek Gupta, and Carlo Scalo. *Real fluid effects on thermoacoustic standing-wave resonance in supercritical CO_2*. American Institute of Aeronautics and Astronautics, 2017/07/04 2017.

[29] G. W. Swift. Thermoacoustic Engines. *J. Acoust. Soc. Am.*, 84(4):1145–1181, 1988.

[30] Clark J. Ward, B. and G. Swift. *Design Environment for Low-amplitude Thermoacoustic Energy Conversion: Users Guide*. Los Alamos National Laboratory, 2012.

[31] M. Pizzarelli, F. Nasuti, R. Paciorri, and M. Onofri. Numerical analysis of three-dimensional flow of supercritical fluid in asymmetrically heated channels. *AIAA J.*, 47:2534–2543, 2009.

[32] B Farouk and N Hasan. Acoustic wave generation in near-critical supercritical fluids: Effects on mass transfer and extraction. *The Journal of Supercritical Fluids*, 96:200–210, 2015.

[33] Thomas Schmitt, Laurent Selle, Anthony Ruiz, and Bénédicte Cuenot. Large-eddy simulation of supercritical-pressure round jets. *AIAA Journal*, 48(9):2133–2144, 2017/06/23 2010.

[34] Peter C. Ma, Yu Lv, and Matthias Ihme. An entropy-stable hybrid scheme for simulations of transcritical real-fluid flows. *J. Comput. Phys.*, 340(Supplement C):330 – 357, 2017.

[35] S. Kawai, H. Terashima, and H. Negishi. A robust and accurate numerical method for transcritical turbulent flows at supercritical pressure with an arbitrary equation of state. *J. Comput. Phys.*, 300(Supplement C):116 – 135, 2015.

[36] Smadar Karni. Multicomponent flow calculations by a consistent primitive algorithm. *Journal of Computational Physics*, 112(1):31 – 43, 1994.

[37] Eleuterio F. Toro. Anomalies of conservative methods: analysis, numerical evidence and possible cures. *Computational Fluids Dynamics Journal*, 11(1), 2002.

[38] Mario Tindaro Migliorino, Jean-Baptiste Chapelier, Carlo Scalo, and Guido Lodato. *Assessment of spurious numerical oscillations in high-order spectral difference solvers for supercritical flows*. American Institute of Aeronautics and Astronautics, 2018/06/28 2018.

[39] F. Hempert, S. Boblest, T. Ertl, F. Sadlo, P. Offenhäuser, C.W. Glass, M. Hoffmann, A. Beck, C.-D. Munz, and U. Iben. Simulation of real gas effects in supersonic methane jets using a tabulated equation of state with a discontinuous galerkin spectral element method. *Computers & Fluids*, 145:167 – 179, 2017.

[40] José O. Valderrama. The state of the cubic equations of state. *Industrial & Engineering Chemistry Research*, 42(8):1603–1618, 2003.

[41] Jean Vidal. *Thermodynamics: Applications in Chemical Engineering and the Petroleum Industry*. Editions Technip, 2001.

[42] G. Soave. Equilibrium constants from a modified Redlich-Kwong equation of state. *Chem. Eng. Sci.*, 27:1197–1203, 1972.

[43] Müller, H., Niedermeier, C. A., Jarczyk, M., Pfitzner, M., Hickel, S., and Adams, N. A. Large-eddy simulation of trans- and supercritical injection, 2016.

[44] Wu Wei, Maozhao Xie, and Ming Jia. Large eddy simulation of fluid injection under transcritical and supercritical conditions. *Numerical Heat Transfer, Part A: Applications*, 70(8):870–886, 2016.

[45] X. Petit, G. Ribert, G. Lartigue, and P. Domingo. Large-eddy simulation of supercritical fluid injection. *The Journal of Supercritical Fluids*, 84:61 – 73, 2013.

[46] L. Pons, N. Darabiha, S. Candel, G. Ribert, and V. Yang. Mass transfer and combustion in transcritical non-premixed counterflows. *Combustion Theory and Modelling*, 13(1):57–81, 2009.

[47] L. Selle and T. Schmitt. Large-eddy simulation of single-species flows under supercritical thermodynamic conditions. *Combustion Science and Technology*, 182(4-6):392–404, 2010.

[48] Guillaume Ribert, David Taieb, and Vigor Yang. Large-eddy simulation of a supercritical channel flow using a shock capturing numerical scheme. *Computers & Fluids*, 117:103 – 113, 2015.

[49] A. Urbano, Q. Douasbin, L. Selle, G. Staffelbach, B. Cuenot, T. Schmitt, S. Ducruix, and S. Candel. Study of flame response to transverse acoustic modes from the {LES} of a 42-injector rocket engine. *Proceedings of the Combustion Institute*, 36(2):2633 – 2639, 2017.

[50] Rémi Abgrall. How to prevent pressure oscillations in multicomponent flow calculations: A quasi conservative approach. *Journal of Computational Physics*, 125(1):150 – 160, 1996.

[51] Michael Dumbser and Vincenzo Casulli. A conservative, weakly nonlinear semi-implicit finite volume scheme for the compressible navierstokes equations with general equation of state. *Applied Mathematics and Computation*, 272:479 – 497, 2016. Recent Advances in Numerical Methods for Hyperbolic Partial Differential Equations.

[52] Marco Pizzarelli, Francesco Nasuti, and Marcello Onofri. {CFD} analysis of transcritical methane in rocket engine cooling channels. *The Journal of Supercritical Fluids*, 62:79–87, 2012.

[53] Mario Tindaro Migliorino and Carlo Scalo. *Dimensionless scaling of heat-release-induced planar shock waves in near-critical CO_2*. American Institute of Aeronautics and Astronautics, 2017/07/04 2017.

[54] Joseph C. Oefelein and Vigor Yang. Modeling high-pressure mixing and combustion processes in liquid rocket engines. *Journal of Propulsion and Power*, 14(5):843–857, 2018/05/11 1998.

[55] Keiichi Kitamura and Eiji Shima. *Pressure-Equation-Based SLAU2 for Oscillation-Free Supercritical Flow Computations*. American Institute of Aeronautics and Astronautics, 2017/06/08 2017.

[56] Keiichi Kitamura, Meng-Sing Liou, and Chih-Hao Chang. Extension and comparative study of ausm-family schemes for compressible multiphase flow simulations. *Communications in Computational Physics*, 16(3):632–674, 2014.

[57] H. Terashima, S. Kawai, and N. Yamanishi. High-resolution numerical method for supercritical flows with large density variations. *AIAA J.*, 49:2658–2672, 2011.

[58] H. Terashima and M. Koshi. Approach for simulating gas/liquid-like flows under supercritical pressures using a high-order central differencing scheme. *J. Comput. Phys.*, 231(20):6907–6923, 2012.

[59] H. Terashima and M. Koshi. Strategy for simulating supercritical cryogenic jets using high-order schemes. *Comput. Fluids*, 85:39–46, 2013.

[60] C. Pantano, R. Saurel, and T. Schmitt. An oscillation free shock-capturing method for compressible van der Waals supercritical fluid flows. *Journal of Computational Physics*, 335:780 – 811, 2017.

[61] G. Lodato, P. Castonguay, and A. Jameson. Discrete filter operators for Large-Eddy simulation using high-order Spectral Difference methods. *Int. J. Numer. Meth. Fluids*, 72(2):231–258, 2013.

[62] J-B Chapelier, G Lodato, and A Jameson. A study on the numerical dissipation of the spectral difference method for freely decaying and wall-bounded turbulence. *Comput. Fluids*, 139:261–280, 2016.

[63] J-B Chapelier and Guido Lodato. A spectral-element dynamic model for the large-eddy simulation of turbulent flows. *J. Comput. Phys.*, 321:279–302, 2016.

[64] Antony Jameson. A proof of the stability of the Spectral Difference method for all orders of accuracy. *J. Sci. Comput.*, 45(1-3):348–358, 2010.

[65] D. A. Kopriva and J. H. Kolias. A conservative staggered-grid Chebyshev multidomain method for compressible flows. *J. Comput. Phys.*, 125(1):244–261, 1996.

[66] Y. Sun, Z. J. Wang, and Y. Liu. High-order multidomain Spectral Difference method for the Navier-Stokes equations on unstructured hexahedral grids. *Comm. Comput. Phys.*, 2(2):310–333, 2007.

[67] Rayleigh. The explanation of certain acoustical phenomena. *Nature*, 18:319–321, 1878.

[68] P.H. Ceperley. A pistonless Stirling engine-the traveling wave heat engine. *J. Acoust. Soc. Am.*, 66:1239–1244, 1979.

[69] A. Migliori and G. W. Swift. Liquid sodium thermoacoustic engine. *Applied Physics Letters*, 53(5):355–357, 1988.

[70] T. Yazaki, A. Iwata, T. Maekawa, and A. Tominaga. Traveling wave thermoacoustic engine in a looped tube. *Phys. Rev. Lett.*, 81(15):3128 – 3131, 1998.

[71] S. Backhaus and G. W. Swift. A thermoacoustic Stirling heat engine. *Nature*, 399(6734):335–338, 1999.

[72] S Backhaus and G. W. Swift. A thermoacoustic-Stirling heat engine: detailed study. *J. Acoust. Soc. Am.*, 107:3148–3166, 2000.

[73] M.E.H. Tijani and S. Spoelstra. A high performance thermoacoustic engine. *J. Appl. Phys.*, 110:093519, 2011.

[74] M. Petach, E. Tward, and S. Backhaus. Design Of A High Efficiency Power Source (HEPS) Based On Thermoacoustic Technology. Technical Report n/a, NASA, 2004.

[75] B.P. Elison, P.V. Mann, and A.K. Sinha. Implementing microscale thermoacoustic heat and power control for processors and 3d chipstacks, March 27 2014. US Patent App. 13/624,051.

[76] M. J. Casiano, J. R. Hulka, and V. Yang. Liquid-propellant rocket engine throttling: A comprehensive review. *J. Propul. Power*, 26(5):897–923, 2010.

[77] T. Poinsot and D. Veynante. *Theoretical and Numerical Combustion*. R.T. Edwards, Inc., third edition, 2011.

[78] H. Wang, J. Zhou, Y. Pan, and N. Wang. Experimental investigation on the onset of thermo-acoustic instability of supercritical hydrocarbon fuel flowing in a small-scale channel. *Acta Astronautica*, 117:296–304, December 2015.

[79] Dayle Alexander, Mario Tindaro Migliorino, Stephen Heister, and Carlo Scalo. *Numerical and Experimental Analysis of a Transcritical Thermoacoustic Prototype*. American Institute of Aeronautics and Astronautics, 2018/06/28 2018.

[80] G. Kirchhoff. Über den Einfluss der Wärmeleitung in einem Gase auf die Schallbewegung. *Pogg. Ann.*, 134:177 – 193, 1868.

[81] H. A. Kramers. Vibrations of a Gas Column. *Physica*, 15(971):971 – 984, 1949.

[82] J. F. J. Malone. A new prime mover. *Journal of the Royal Society of Arts*, 79(4099):679–709, 1931.

[83] G. W. Swift. Analysis and performance of a large thermoacoustic engine. *J. Acoust. Soc. Am.*, 92(3):1551 – 1563, 1992.

[84] T. Yazaki, A. Iwata, T. Maekawa, and A. Tominaga. Traveling Wave Thermoacoustic Engine in a Looped Tube. *Phys. Rev. Lett.*, 81(15):3128–3131, October 1998.

[85] I. E. Idelchik. *Handbook of Hydraulic Resistance*. CRC Press, 3rd edition, 2003.

[86] D. R. Kassoy. The response of a confined gas to a thermal disturbance. i: Slow transients. *SIAM Journal on Applied Mathematics*, 36(3):624–634, 1979.

[87] Sutrisno and D. R. Kassoy. Weak shocks initiated by power deposition on a spherical source boundary. *SIAM Journal on Applied Mathematics*, 51(3):658–672, 1991.

[88] Y. Miura, S. Yoshihara, M. Ohnishi, K. Honda, M. Matsumoto, J. Kawai, M. Ishikawa, H. Kobayashi, and A. Onuki. High-speed observation of the piston effect near the gas-liquid critical point. *Phys. Rev. E*, 74:010101, Jul 2006.

[89] J. F. Clarke, D. R. Kassoy, and N. Riley. Shocks generated in a confined gas due to rapid heat addition at the boundary. ii. strong shock waves. *Proceedings of the Royal Society of London A*, 393(1805):331–351, 1984.

[90] M.B.E. Boslough and D.A. Crawford. Low-altitude airbursts and the impact threat. *International Journal of Impact Engineering*, 35(12):1441 – 1448, 2008. Hypervelocity Impact Proceedings of the 2007 SymposiumHVIS 2007.

[91] National Research Council. *Defending Planet Earth: Near-Earth-Object Surveys and Hazard Mitigation Strategies*. The National Academies Press, Washington, D.C., 2010.

[92] Geoffrey Taylor. The formation of a blast wave by a very intense explosion. i. theoretical discussion. *Proceedings of the Royal Society of London A: Mathematical, Physical and Engineering Sciences*, 201(1065):159–174, 1950.

[93] Ji Won Suk, Karen Kirk, Yufeng Hao, Neal A. Hall, and Rodney S. Ruoff. Thermoacoustic sound generation from monolayer graphene for transparent and flexible sound sources. *Advanced Materials*, 24(47):6342–6347, 2012.

[94] Qingming Liu and Yunming Zhang. Shock wave generated by high-energy electric spark discharge. *Journal of Applied Physics*, 116(15):153302, 2014.

[95] R. J. Krane and M. Parang. Scaling analysis of thermoacoustic convection in a zero-gravity environment. *Journal of Spacecraft and Rockets*, 20(3):316–317, 2017/06/22 1983.

[96] Pierre Carlès. Thermoacoustic waves near the liquid-vapor critical point. *Physics of Fluids*, 18(12):126102, 2006.

[97] B. Shen and P. Zhang. Thermoacoustic waves along the critical isochore. *Phys. Rev. E*, 83:011115, Jan 2011.

[98] Akira Onuki, Hong Hao, and Richard A. Ferrell. Fast adiabatic equilibration in a single-component fluid near the liquid-vapor critical point. *Phys. Rev. A*, 41, 1990.

[99] Hacène Boukari, Matthew E. Briggs, J. N. Shaumeyer, and Robert W. Gammon. Critical speeding up observed. *Phys. Rev. Lett.*, 65:2654–2657, Nov 1990.

[100] B. Zappoli, D. Bailly, Y. Garrabos, B. Le Neindre, P. Guenoun, and D. Beysens. Anomalous heat transport by the piston effect in supercritical fluids under zero gravity. *Phys. Rev. A*, 41:2264–2267, Feb 1990.

[101] Sakir Amiroudine and Bernard Zappoli. Piston-effect-induced thermal oscillations at the rayleigh-bénard threshold in supercritical ^{3}He. *Phys. Rev. Lett.*, 90:105303, Mar 2003.

[102] B. Zappoli. Near-critical fluid hydrodynamics. *Comptes Rendus Mécanique*, 331(10):713–726, 2003.

[103] Akira Onuki. Thermoacoustic effects in supercritical fluids near the critical point: Resonance, piston effect, and acoustic emission and reflection. *Phys. Rev. E*, 76:061126, Dec 2007.

[104] Pierre Carlès. A brief review of the thermophysical properties of supercritical fluids. *The Journal of Supercritical Fluids*, 53(1-32):2–11, 2010.

[105] Matthew A. Brown and Stuart W. Churchill. Experimental measurements of pressure waves generated by impulsive heating of a surface. *AIChE Journal*, 41(2):205–213, 1995.

[106] B. Zappoli and A. Durand-Daubin. Direct numerical modelling of heat and mass transport in a near supercritical fluid. *Acta Astronautica*, 29(10/11):847–859, 1993.

[107] A. Nakano. Studies on piston and soret effects in a binary mixture supercritical fluid. *International Journal of Heat and Mass Transfer*, 50(23–24):4678–4687, 2007.

[108] Nusair Hasan and Bakhtier Farouk. Thermoacoustic transport in supercritical fluids at near-critical and near-pseudo-critical states. *The Journal of Supercritical Fluids*, 68:13–24, 2012.

[109] N Hasan and B Farouk. Fast heating induced thermoacoustic waves in supercritical fluids: Experimental and Numerical Studies. *Journal of Heat Transfer*, 135(8):081701, 2013.

[110] B. Shen and P. Zhang. On the transition from thermoacoustic convection to diffusion in a near-critical fluid. *International Journal of Heat and Mass Transfer*, 53(21–22):4832–4843, 2010.

[111] In-Ju Hwang and Youn-Jea Kim. Measurement of thermo-acoustic waves induced by rapid heating of nickel sheet in open and confined spaces. *International Journal of Heat and Mass Transfer*, 49(3–4):575 – 581, 2006.

[112] B. T. Chu. Pressure waves generated by addition of heat in a gaseous medium. *NACA-TN 3411*, (NACA-TN 3411), 1955. https://ntrs.nasa.gov/archive/nasa/casi.ntrs.nasa.gov/19930084155.pdf.

[113] P.E. Doak. Fluctuating total enthalpy as the basic generalized acoustic field. *Theoretical and Computational Fluid Dynamics*, 10(1):115–133, 1998.

[114] J. Larsson and S. K. Lele. Direct numerical simulation of canonical shock/turbulence interaction. *Phys. Fluids*, 21:126101, 2009.

[115] G. A. Bird. *Molecular Gas Dynamics and the Direct Simulation of Gas Flows*. Oxf. Univ. Press, 1994.

[116] S. W. Rienstra and A. Hirschberg. *An Introduction to Acoustics*. Eindhoven University of Technology, 2017.

[117] Arthur S. Iberall. The effective "gamma" for isentropic expansions of real gases. *Journal of Applied Physics*, 19(11):997–999, 1948.

[118] P. A. Thompson. A fundamental derivative in gasdynamics. *Physics of Fluids*, 14(9):1843–1849, 1971.

VITA

VITA

Mario Tindaro Migliorino was born in Rome, Italy to Placido Migliorino and Antonella Pepe on March 8, 1991. After completing his studies at the Nomentano High School in 2010, he started his undergraduate studies in aerospace engineering at Sapienza University of Rome. He graduated with a Bachelor of Science in 2013, and also got a Master of Science from the same university in 2015. From August 2015, he attended the Ph.D. program in the School of Mechanical Engineering at Purdue University. His research at Purdue, guided by Dr. Carlo Scalo, focused on the fundamental understanding of thermoacoustic instabilities in transcritical fluids. Mario will receive his PhD in December 2018.